A Computational Approach to the Stability of Complex Sphere Forming Phases in Block Polymer Melts

A DISSERTATION

SUBMITTED TO THE FACULTY OF THE GRADUATE SCHOOL

OF THE UNIVERSITY OF MINNESOTA

BY

Guo Kang Cheong

IN PARTIAL FULFILLMENT OF THE REQUIREMENTS

FOR THE DEGREE OF

DOCTOR OF PHILOSOPHY

Advisor: Kevin D. Dorfman

May, 2021

Acknowledgements

Firstly, I want to express my utmost gratitude to my advisor Prof. Kevin D. Dorfman. Your invaluable advising and optimistic outlook were instrumental to the success of this work. I appreciate your investment into my career, even going as far as giving me an opportunity to change the direction of my research from nanoconfined polymers to block polymers halfway into my PhD career. I very much enjoyed working with you as my advisor. I tend to spend long stretches of time working on a problem and few are flexible enough to fully trust in my work like you did.

I sincerely thank Prof. David Morse, Prof. Frank Bates, and Prof. Jorge Viñals for serving as my committee member and for providing their feedback for my thesis. I especially thank Prof. David Morse and Prof. Frank Bates who were collaborators in my projects and for providing their insights into our work. I also want to thank my fellow experimental colleagues, Aaron Lindsay and Andreas Mueller, whose exceptional works inspire the projects in this thesis.

I have the opportunity to work alongside with a group of wonderful colleagues during my six years in the Dorfman group. I appreciate the work that Akash and Xiaolan have done in SCFT and PERM, respectively, which a lot of my work builds upon. I want to thank Hui-Min, Aditya, Mathew, and Paridhi for making the basement where we work a little bit brighter even if we do not get much sunlight at all! I also enjoyed my conversations with my junior colleagues, Zixue, Logan, Anshul, Demetra, Sarah, Ryan,

and Pengyu. I appreciate all the connections I made in the department over the years and will treasure all the interactions that we had.

To my parents, your sacrifices in life are what allowed me to pursue this path. Your selfless devotion to the well-being of our family has got us through even the most difficult of times. To my siblings, you two are central in helping me navigate through life. I could always count on your guidance and advise to figure out what is best for me.

I would like to thank the National Science Foundation (NSF DMR-1725272, NSF DMR-1719692), Doctoral Dissertation Fellowship, and Rutherford Aris Memorial Fellowship for financially supporting this work. I would also like to extend my thanks to the Minnesota Supercomputing institute for providing the computational resources to this work.

To the Cheong Family

Abstract

Block polymers spontaneously self-assemble into a variety of morphologies upon cooling below their order-disorder temperature. Owing to this behavior, block polymers have various potential applications ranging from semiconductors fabrication to filtration devices. Recent discovery of the stable Frank-Kasper phases in diblock copolymer melts resulted in a shift of focus from high-symmetry morphologies to low-symmetry tetrahedrally close-packed phases. While experimentalists have been able synthesize block polymers that exhibit stable Frank-Kasper phases, they could not predictably determine the observed phases *a priori*. Computational tools can aid in prediction but are rooted in well-developed theories and experimental results. In this dissertation, we aim to develop theoretical understanding of the stability of Frank-Kasper phases that could aid in prediction through a computational study of block polymers guided by experimental data. To this end, we take a three-pronged approach in the dissertation. First, we examined an experimental diblock copolymer/homopolymer system which produces a variety of Frank-Kasper phases. Our computational study reproduced the salient behavior of the system and unveiled a new mechanism for the stabilization of Frank-Kasper phases. Next, we studied the disordered micelle regime, which has consequence in stabilizing metastable Frank-Kapser phases in thermal processing experiments, for conformationally asymmetric diblock copolymer melts. We uncovered a reduction in the window of stability for the disordered micelle regime with increasing conformationally asymmetric. Finally, we compared computational prediction of binary blends of high molecular weight diblock copolymer to experimental results and demonstrated their utility in accessing Frank-Kasper phases. Along with our analysis, we unveiled a potentially new mechanism that may be important in the stabilization of Frank-Kasper phases. We believe that our work in this dissertation provides additional understanding to the behavior of diblock copolymer, specifically in stabilizing Frank-Kasper phases.

This work also opens up potential avenues of interest that may further our ability to tailor block polymers for specific applications.

Contents

List of Tables

List of Figures

Chapter 1

Introduction

Block polymers, consisting of two or more chemically distinct polymers covalently joined together at their ends, spontaneously form ordered structures below some order-disorder temperature, T_{ODT}. At low temperatures, chemically distinct polymers tend to macrophase separate in a homopolymer blend, but are unable to do so in a block polymer melt owing to the strong covalent bond at their intersection. Upon cooling of the block polymer melt, which is a one component system of pure block polymer, the system instead microphase separates into a multitude of ordered structures with complex geometries. The classical phases commonly observed in the self-assembly of block polymers are shown in Fig. 1.1 which include Lamellar (LAM), Hexagonal Cylinders (HEX), sphere-forming structures such as BCC and FCC, and the bicontinuous Gyroid (Gyr).

With modern advances in synthesis, we now see increasingly complex and precise types of block polymers being synthesized with a myriad of architectures and chemistries resulting in varying physical and rheological properties [1]. Indeed, owing to the flexibility and vast design space of these materials, countless works have sought to exploit block

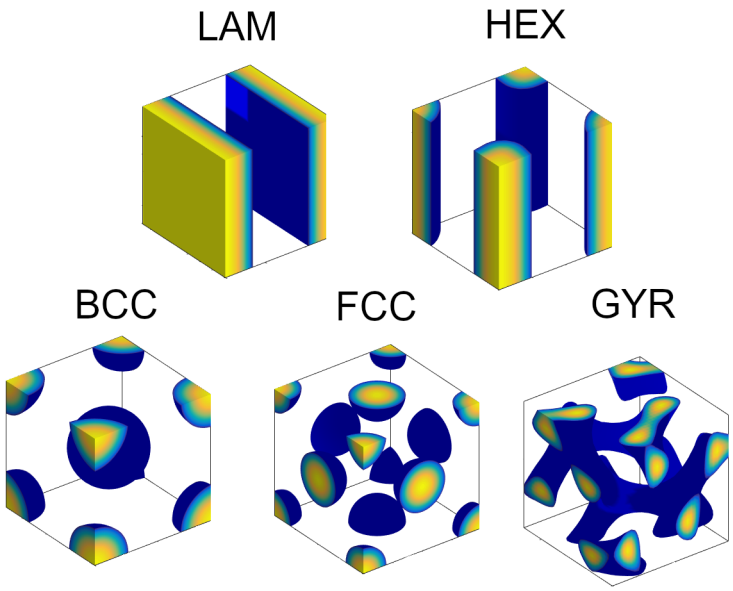

Figure 1.1: Classical phases commonly observed below T_{ODT} for block polymer systems. The morphologies shown here include the one-dimensional Lamellar (LAM), the two-dimensional Hexagonal Cylinders (HEX), and three-dimensional structures of Body Centered Cubic (BCC), Face Centered Cubic (FCC), and Gyroid phase (GYR).

polymers as designer materials with limitless potential [2]. Block polymers have applications ranging from thin films that form the basis of next generation semiconductors [3–5], membranes for filtration devices [6–8], and even tunable photonic crystals [9, 10].

With an exceedingly large design space, it is imperative to isolate the tunable parameters responsible for the selection of ordered structures in block polymers. Computation provides an avenue to rapidly study these systems by parsing through large ranges of parameters, whose result can then be experimentally confirmed. Computational studies can not only be performed rapidly in certain cases, but also can probe length scales not easily accessible in experimental studies. For example, small angle x-ray scattering

(SAXS) is the standard experimental technique used to probe the structure of block polymer melts [11]. While the utility of SAXS is indisputable, it only provides aggregated information of the system in inverse space and lacks the ability to differentiate, say, chemically identical macromolecules but with different chain lengths. Naturally, computational tools can track all the different types of macromolecules in a particular system, providing information which might enable new understanding of the underlying physical phenomena.

One outstanding question that could benefit from the synergistic workflow highlighted above is the factors surrounding the stability of Frank-Kasper phases in block polymers. Unlike the classical ordered structures, Frank-Kasper phases are low-symmetry sphere-forming structures, which are typically observed in metals, patterned by clusters of 12-, 14-, 15-, and 16-fold coordination numbers [12, 13]. Recent experimental works have observed stable Frank-Kasper phases including σ [14–18], A15 [15, 16, 19], C14 [17, 20, 21], and C15 [20, 21] in block polymer systems. The discovery of these low symmetry phases resulted in a paradigm shift which focuses on the stability of these Frank-Kasper phases over high-symmetry classical phases. Since their first observation, experimentalists have been able to predictably stabilize these phases by exploiting a combination of experimental processing [20, 22] and the synthesis of polymers with particular characteristics [18, 23]. However, the mechanisms behind these phenomena and how they stabilize Frank-Kasper phases remain a working hypothesis [21]. While experimentalists can synthesize block polymers that self-assemble into low-symmetry phases, they cannot predictably choose the specific phases or their associated window of stability. As such, we take a computational approach to provide a deeper understanding of the experimental results in this dissertation.

1.1 The Gaussian chain model

To facilitate the discussion of the stability of these ordered phases, we first introduce a mathematical model of block polymer known as the continuous Gaussian chain model [24, 25]. As it is the main type of block polymer studied in this work, we will describe this model specifically for the diblock copolymer, which is the simplest type of block polymer, consisting of only two blocks of type, say, A and B. The continuous Gaussian chain model treats the block polymer strand as the continuum limit of linear bead-spring chain model. A single chain is composed of segments with a volume of ρ_0^{-1} and with each of the two blocks having $N_{i=A,B}$ segments, respectively. The full chain is thus characterized by the total degree of polymerization, $N = N_A + N_B$, and the volume fraction of the A-block, $f_A = N_A/(N_A + N_B)$. In the Gaussian chain model, the incompatibility between the two blocks is characterized by the parameter χN, where χ is the Flory-Huggins parameter. With only two parameters, f_A and χN, this mathematical model is sufficient to qualitatively describe much of the phase diagram of the diblock copolymer system. Indeed, the phase diagram in Fig. 1.2 was generated using Self-Consistent Field theory (SCFT), a mean-field limit of the many-chain Gaussian chain model, with only the two parameters, χN and f_A. As a mean field method, SCFT perfectly reproduces all behaviors of the block polymer system in the extreme limit of $N \to \infty$ but still agrees reasonably well with the experimental phase diagram of sufficiently long block polymer chains. [27, 28].

While facile, the two parameters f_A and χN do not constitute the complete set of parameters describing the system. With a focus on Frank-Kasper phases, parameters secondary to f_A and χN become increasingly important in fully describing and understanding the stability of these phases. The first of these is the statistical segment length of a chain, b_i, which can be treated as the flexibility of the chain. For a diblock copolymer, the focus is on the ratio of statistical segment length of both blocks, also

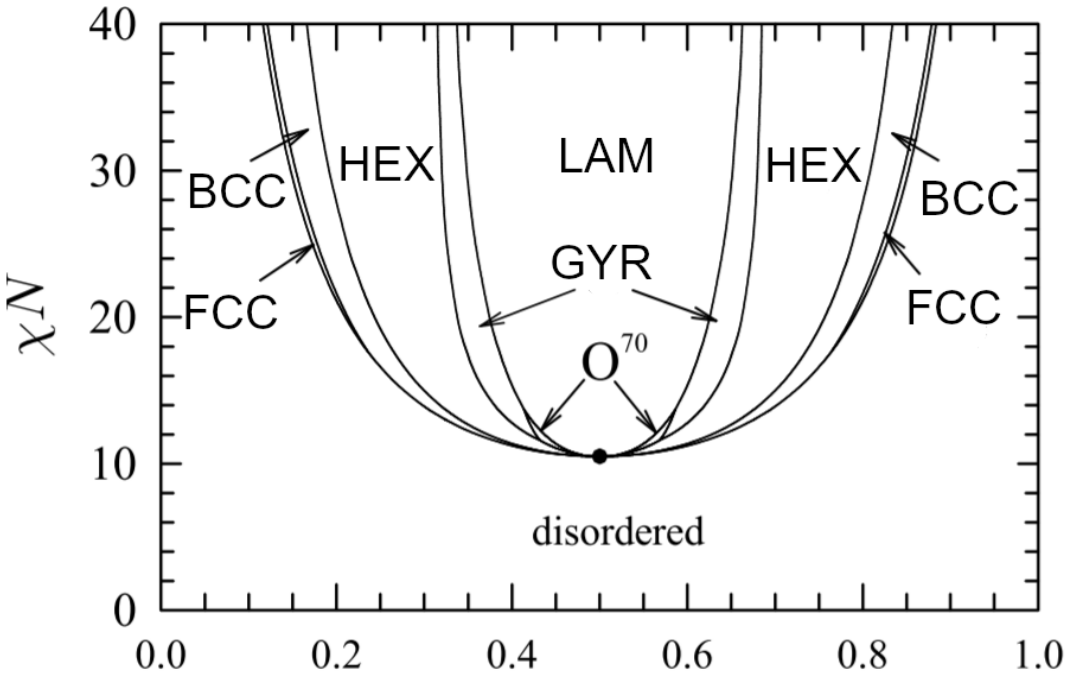

Figure 1.2: SCFT phase diagram for conformationally symmetric, $\epsilon = 1$, diblock copolymer. The phase diagram shows regions of stability for Lamellar (LAM), Hexagonal Cylinders (HEX), Body Centered Cubic (BCC), Face Centered Cubic (FCC), Gyroid (GYR), and Fddd (O^{70}). Figure reproduced from [26].

known as conformational asymmetry, $\epsilon = b_A/b_B$ [29, 30]. Recent works have observed Frank-Kasper phases overtaking classical phases in stability for block polymeric systems with high conformational asymmetry [16, 18, 31]. As such, conformational asymmetry is one of the key molecular design tricks in ensuring the stability Frank-Kasper phase in the diblock copolymer phase diagram.

Another key parameter that is relevant in the stability of Frank-Kasper phases is the invariant polymerization index, $\bar{N} = a^6\rho_0^2 N$, where $a = (f_A b_A^2 + (1 - f_A)b_B^2)^{1/2}$ is the effective statistical segment length of the diblock copolymer [32]. As mentioned previously, SCFT is only perfectly accurate in the limit of infinite chain length or, equivalently, $\bar{N} \to \infty$. In this limit, all composition fluctuations in the system are suppressed resulting in the mean-field solution being exact. As $\bar{N}$ decreases from infinity, mean-field predictions start deviating from the experimental results and, in the limit of very short chains, fail to observe stable Frank-Kasper phases [28, 32]. Where the mean-field method breaks down, direct order-disorder transition to low-symmetry phases in experiments are also not observed in computational methods [16]. Thus, it warrants additional probing of the Gaussian chain model while accounting for the effects of $\bar{N}$.

In this work, we will focus only on the parameters above, which have already unveiled a myriad of phenomena that pose interesting scientific questions. Certainly, there are other additional factors relevant in the selection of ordered phases past the ODT. For example, the Gaussian chain model can also describe block polymeric system with a more complex architecture such as linear chains with more than two blocks [33, 34], miktorm-arm/star polymers [35–37], and bottlebrush polymers [37, 38], which all have very different phase diagrams. The model can also be modified to handle polydispersity, which is a measure of the distribution of molecular weights of the system [37, 39–41]. Nevertheless, we believe there are still many unknowns in regards to the deceptively

simple diblock copolymer worthy of our intellectual curiosity. To put this into perspective, the first computational phase diagram for the diblock copolymer was obtained in 1994 [30]. Eleven years later, there was an addendum to the phase diagram with the discovery of a region where the O^{70} network phase is stable [33]. Another five years later, experimental studies discovered a stable Frank-Kasper σ phase in tetrablock terpolymer melts and diblock copolymers [14]. Certainly, there are still many open problems in regards to the simple diblock copolymers where new discoveries are still made to this date for a system whose phase diagram was effectively solved 27 years ago.

1.2 Research Outline

With the Gaussian chain model highlighted above, we can proceed to computationally study systems of diblock copolymer with respect to the stability of complex Frank-Kasper phases, especially in collaboration with experimental evidence. With the design space for block polymer growing larger with every improvement of synthetic methods, a collaborative effort can be immensely helpful in the direction of using block polymers for future applications. Having better mechanistic understanding of the stability of Frank-Kasper phase allows us to specifically tailor synthetic efforts toward particular physical property for a chosen application. As such, the goal of this dissertation is to *understand the mechanism behind the stability of complex sphere-forming phases* particularly through computational study of diblock polymers guided by experimental data.

In line with the objective above, Chapter 2 showcases two cutting-edge computational tools developed to study block polymeric systems. Firstly, we have updated a previously open-source SCFT tool to utilize graphics processing unit (GPU) acceleration. In that chapter, we describe the implementation of SCFT especially through the lens of GPU-accelerated algorithms. Our highly efficient implementation achieves

speedups of up to 50x compared to the open-source version. The development of high-speed processing tool allows not only rapid examination of the phase space, which is vital in searching for complex sphere forming phases, but also allows opportunities for material discovery by the community at large owing to its open-source nature. With good documentation and easy-to-use tutorials, our implementation allows experimentalists to use such tools to supplement their own work, in line with our stated goals of collaboration between experimentalists and computationalists. Next, we describe the implementation of a Monte Carlo-Field Theoretic Simulation (MC-FTS) wrapper around the GPU-accelerated system. MC-FTS is a method similar to the mean-field SCFT but allows fluctuations in the system with $\bar{N}$ as an input parameter. The fluctuations have implications in the formation of micelles in the disordered micelle phase which we will fully explore in Chapter 4.

In Chapter 3, we examine the sphere forming structure in diblock polymer/homopolymer blends. Inspired by experiments discovering a variety of Frank-Kasper phases in such blends, we performed SCFT calculations for three different blends of varying homopolymer length and discovered a pattern of order-order transition of BCC to σ to C14 to C15. By performing a particle-by-particle analysis, we confirmed a hypothesis posited by our experimental colleagues on the partitioning of homopolymer in the system. Detailed analysis of the partitioning of the homopolymer unveiled a new mechanism for the stabilization of Frank-Kasper phases only available to blends. This mechanism, which is unlike any described earlier, leverages the delayed onset of macrophase separation which favors the formation of structures with increasingly larger volume asymmetry. This work not only suggests a new pathway for the formation of Frank-Kasper phases but also allows experimentalist to anticipate the selection of specific phases in the system.

Next, we examine the formation of disordered micelle regime in diblock copolymer

melts for different values of conformational asymmetry in Chapter 4. Near the T_{ODT}, compositionally asymmetric (low-f_A) diblock copolymer melts spontaneously form disordered micelles with short-range ordering while lacking the long-range order associated with crystalline structures. Our calculations show a wide window of stability for the disordered micelle regime in conformationally symmetric diblock copolymer but a much narrower window of stability for the conformationally asymmetric case at relatively high $\bar{N}$ of 10^4. We posit that the formation of disordered micelles occurs near the order-disordered segregation strength determined by SCFT, $\chi N_{\mathrm{ODT}}^{\mathrm{SCFT}}$. Meanwhile, the window of stability of disordered micelles is determined by the distance between $\chi N_{\mathrm{ODT}}^{\mathrm{SCFT}}$ and the true order-disordered segregation strength of the fluctuation-based method. Our analysis has implications for the use of thermal processing in experiments to form metastable Frank-Kasper phases which survive multiple heating-cooling cycles owing to the memory of their thermal processing history in the disordered micelle regime.

In Chapter 5, we examined a system of binary blends of diblock copolymer where the B-block have the same length but with different block length for the A-block, A_1B/A_2B. We examined three different blends of the same A_1 block length but increasingly longer A_2 block length. We reproduced the experimental phase diagrams through SCFT, demonstrating the utility of binary blends for the formation of a collection of Frank-Kasper phases whose stability can be easily predicted by this computational method. Further, a particle-by-particle analysis of the binary blend unveiled selective partitioning of the two different types of chains in the unit cell mimicking bonding/antibonding behavior of molecular orbital theory. By tracking the two types of chemically indistinguishable chains in the calculations, we further establish the utility of a synergistic collaborative effort of experimental and computational work for discovering new mechanisms explaining the behaviors observed in experimental work.

Finally, in Chapter 6, we summarize the findings of our previous works and postulate future avenues that build upon them. We propose ideas that are attractive in the spirit of collaboration between experimentalist and computationalist.

Chapter 2

Self-Consistent Field Theory and Monte Carlo-Field Theoretic Method [1]

The key step in computational design of block polymer materials is identifying the stable morphology at a given state point, ideally via parameters that can be readily mapped to experimental studies. In the Gaussian chain model, a system of volume, V, contains n $= V\rho_0/N$ chains. In this many chain system, the pairwise interchain interaction can be relegated to one or more external field under the Hubbard-Stratonovich transformation [24, 42]. This changes the problem posed from a many-chain problem to a single-chain in an external field problem that is mathematically easier to solve. The derivation for this transformation can be found elsewhere [24, 42] but the resulting partition function

[1] Portions of this chapter were reproduced from Guo Kang Cheong, Anshul Chawla, David C. Morse and Kevin D. Dorfman, European Journal of Physics E 43, 15 (2020)

for the canonical ensemble is

$$Z \sim \int \int \exp\left(-\frac{H[W_-, W_+]}{k_B T}\right) DW_- DW_+ \tag{2.1}$$

where $k_B T$ is the Boltzmann factor and the interaction between chains are relegated to the external fields known as the composition field, W_- and the pressure field, W_+. The Hamiltonian is given as

$$\frac{H[W_-, W_+]}{n k_B T} = -\ln Q + \frac{1}{V} \int \left(\frac{W_-^2(\mathbf{r})}{\chi N} - W_+(\mathbf{r})\right) d\mathbf{r}. \tag{2.2}$$

where Q is the single chain partition function whose computation will be discussed later. In SCFT, the fluctuating fields are taken to be their extremum value which, as mentioned in Chapter 1, is exact when $\bar{N} \to \infty$. In this limit, the Hamiltonian is also the free energy of the system,

$$F = -k_B T \ln Z = H \tag{2.3}$$

SCFT is thus well-suited to the purpose of identifying the stable morphology at a given state point. SCFT can also serve as the compute engine for inverse design strategies [43–49]. However, SCFT has been underutilized as a tool due to the lack of readily available open-source software [50]. The release of the Polymer Self Consistent Field (PSCF) code [51] improved this situation by providing an open-source SCFT solver along with guides for initializing calculations and examples of usage [50].

The original PSCF code [50] was designed to utilize only a single CPU core. This provides adequate speed for many tasks, and has allowed the code to be successfully used to analyze block copolymer phase behavior [20,21,52–68]. To determine the relative

stability of different candidate morphologies in a region of the block polymer parameter space, an SCFT calculation must be performed for each competing morphology at many points in parameter space. If one has access to a CPU cluster, this task can be partially parallelized by assigning different morphologies and different regions of parameter space to different CPU cores. The single CPU implementation inevitably becomes a bottleneck, however, when each calculation requires a sufficiently long time to complete. The time required to solve the modified diffusion equation by a pseudo-spectral SCFT algorithm scales as $O(N_s N_n \log N_n)$ [53], where N_n is the number of nodes in the spatial mesh and N_s is the number of contour length integration steps. Some particularly important examples of computationally challenging problems involve candidate morphologies that have very large unit cells, such as Frank-Kasper phases and Laves phases [12–15, 17, 18, 20–22, 28, 31, 34, 36, 57, 69–73]. Evaluating the relative stability of several competing Frank-Kasper phases is particularly challenging because of the need to use a large number nodes in the spatial mesh, and the need to test the dependence of free energy on both N_n and N_s to ensure sufficient accuracy when comparing phases with very similar free energies [20]. Obtaining an SCFT solution for Frank-Kasper phases in PSCF also generally requires many iterations to converge [50, 74]. Likewise, problems involving strongly segregated components and narrow interfaces are particularly challenging. Computation time also becomes a bottleneck for inverse design problems [43–49], since many SCFT calculations are required during the search of the design space. Clearly, PSCF stands to benefit from having a massively parallelized version which could be used to accelerate expensive calculations.

For this reason, we have implemented a GPU-accelerated version of PSCF. Delaney and Fredrickson previously described a GPU implementation of SCFT within their closed software package and found remarkable speed-ups of up to 60× for single precision calculations [75]. Following these authors, we also chose a GPU implementation over

a multiple-CPU mesage passing implementation because the computational time of SCFT is dominated by Fast Fourier Transforms (FFT) [75]. FFTs are very effectively accelerated on GPUs, but suffer from significant communication costs in multi-CPU message passing implementations.

The GPU-accelerated code that we focus on here differs from that of Delaney and Fredrickson [75] in two ways. First, the two codes use different iteration algorithms. The algorithms described by Delaney and Fredrickson obtain a solution of the self-consistent field equations through a relaxation scheme. Our implementation instead uses an Anderson mixing iteration scheme [76, 77] that can be used to optimize the unit-cell dimensions simultaneously with the solution of the self-consistent field equations [74,78]. Secondly, and more importantly, our implementation is available for use by others as an open-source code. We found that our implementation obtains a speed-up of up to $\sim$60$\times$ relative to the existing Fortran PSCF code for sufficiently large single precision problems, comparable to the speed-up obtained by Delaney and Fredrickson.

This code is distributed [79] as part of a rewritten version of the PSCF package that also contains several CPU-based programs. While the original PSCF program was written in Fortran 90, the new package has been rewritten using C++ for code that is implemented on the CPU and CUDA for code that is implemented on a GPU.

2.1 SCFT algorithm and implementation details

The most computationally expensive part of SCFT is the solution of the modified diffusion equation (MDE). The forward propagator, $q(\mathbf{r}, s)$, of a linear multiblock polymer is computed from the solution of the MDE,

$$\frac{\partial q(\mathbf{r}, s)}{\partial s} = \left[\frac{b_\alpha^2}{6} \nabla^2 - \omega_\alpha(\mathbf{r}) \right] q(\mathbf{r}, s) \quad . \tag{2.4}$$

The parameter b_α is the statistical segment length within a block containing monomers of type α, $s \in [0, N]$ is a contour variable, $\mathbf{r}$ is the position variable, and ω_α is the spatially-dependent potential field acting on monomers of type α. For the diblock copolymer, the relationship between W_-, W_+ and ω_α is,

$$W_- = \frac{\omega_A - \omega_B}{2} \tag{2.5}$$

$$W_+ = \frac{\omega_A + \omega_B}{2} \tag{2.6}$$

with the choice of the symbol ω being the extremum fields and W being the fluctuating fields. The corresponding backward propagator, $q^\dagger(\mathbf{r}, s)$, follows the same MDE but with the sign of the time derivative in Eq. 2.4 reversed. In both cases, the initial condition is $q(\mathbf{r}, 0) = q^\dagger(\mathbf{r}, N_s) = 1$.

Solutions of the MDE are obtained in PSCF using the pseudospectral algorithm of Ranjan, Qin and Morse (RQM) [53]. This algorithm yields a discretization error of order $(\Delta s)^4$, where $\Delta s = N/N_s$ is the contour length step size, N is chain contour length, and N_s is the number of contour length steps. Typically, each chain is discretized into $N_s \sim 10^2$ steps. The RQM algorithm has been shown to be very effective for high accuracy SCFT calculations [80]. This algorithm involves six Fast Fourier Transform (FFT) operations at each step of integration along the contour length of the polymer, which dominate the cost of the algorithm [75]. In our code, NVIDIA's CUFFT library is used to perform all FFTs on the GPU. All other operations with a cost per contour step that is proportional to the number of grid points, such as point-wise multiplications, are also implemented on the GPU.

Following the solution of Eq. 2.4 for q and the counterpart equation for $q^\dagger$, the

volume fraction of each monomer at position $\mathbf{r}$ is computed as

$$\phi(\mathbf{r}) = \frac{1}{NQ} \int q(\mathbf{r}, s) q^{\dagger}(\mathbf{r}, s) ds \quad , \tag{2.7}$$

where the partition function for an unconstrained chain is

$$Q = \frac{1}{V} \int q(\mathbf{r}, N_s) d\mathbf{r} \quad . \tag{2.8}$$

The integral with respect to s in Eq. 2.7 is computed using Simpson's rule, while the spatial average in Eq. 2.8 is computed as an average over mesh nodes [77]. Both types of integration are implemented on the GPU, where the division of work is at the level of an individual grid point.

The chemical potential fields in the modified diffusion equation must be chosen so as to satisfy the SCFT self-consistency condition,

$$\omega_{\alpha}(\mathbf{r}) = \sum_{\beta \neq \alpha} \chi_{\alpha\beta} \phi_{\beta}(\mathbf{r}) + \xi(\mathbf{r}) \quad , \tag{2.9}$$

for the chemical potential potential field, ω_{α} for each monomer type α. Here, $\xi(\mathbf{r})$ is a Lagrangian that enforces incompressibility constraint, which requires that

$$\sum_{\alpha} \phi_{\alpha}(\mathbf{r}) = 1 \tag{2.10}$$

at every position $\mathbf{r}$ in the unit cell.

In an SCFT calculation with a flexible unit cell, the MDE and SCFT equations are supplemented by a requirement that parameters of the unit cell be chosen so as to minimize the free energy per unit volume or (in a one-component melt) per chain. Let N_c denote the number of parameters (lengths and angles) required to describe the unit cell

of a particular type (e.g., cubic, hexagonal, tetragonal, etc.), and let $\theta_1, \ldots, \theta_{N_c}$ denote a list of these parameters. In a block copolymer melt, the requirement of minimization of the free energy can be expressed as a requirement that

$$0 = -\frac{1}{Q}\frac{\partial Q}{\partial \theta_i} \tag{2.11}$$

for all $i = 1, \ldots, N_c$. The calculation of the stress in the unit cell in Eq. 2.11 is obtained using a perturbation theory that provides an analytical form of derivative $\partial Q/\partial \theta_i$ [78]. Efficient calculation of this derivative in a pseudo-spectral algorithm requires knowledge of the spatial Fourier transforms of the forward and reverse MDE solutions $q(\mathbf{r}, s)$ and $q^\dagger(\mathbf{r}, s)$ at each step of the contour length variable. Calculation of $\partial Q/\partial \theta_i$ thus requires the calculation of two additional FFTs per contour integration step, per trial choice of the chemical potential fields and unit cell parameters, in addition to the six FFTs required by the RQM algorithm for solving the MDE. These two additional FFTs are performed on the MDE solutions q and $q^\dagger$ after each completion of the RQM algorithm for computing these quantities. To reduce the cost of these additional FFTs, solutions of q and $q^\dagger$ are stored in a contiguous memory array that can then be pipelined into the CUFFT batching system. This batch processing of FFTs results in a speed-up of up to $2\times$ for this operation compared to performing separate FFTs.

Equations 2.4-2.11 constitute a set of nonlinear, non-local equations that need to be solved simultaneously to obtain an SCFT solution in an optimal unit cell. A calculation with a flexible unit cell typically begins with a guess for the potential fields $\omega_\alpha(\mathbf{r})$ and for the unit cell parameters. Reference [50] provides step-by-step recipes for generating initial chemical potential fields for both particle-forming phases and network phases. These initial guesses must then be iteratively adjusted until Equations 2.9-2.11 are satisfied. To obtain an SCFT solution in a fixed unit cell, one instead begins with an

initial guess for the chemical potential fields and iteratively solves Equations 2.4-2.10, while treating the unit cell parameters as constants.

The self-consistent solution is found using an iterative procedure known as Anderson mixing [74, 76, 77, 81]. The form of Anderson mixing used in both the CPU code and the GPU code is the same as that presented by Arora *et al.* [74], which is only briefly summarized here. This algorithm is based on a reformulation of equations 2.9 and 2.10 for a system with N_m distinct types of monomers as a set of N_m independent equations per point in space (in a continuum) or per node on the FFT mesh (in a discretized solution), given by equations 10-12 in Ref. [74]. In an SCFT problem with a rigid unit cell, this formulation gives a system of $N_m N_f$ independent equations that must be satisfied by the chemical potential fields, where N_f is the number of independent degrees of freedom used to represent the chemical potential and volume fraction fields associated with each monomer type. The version of Anderson mixing implemented in the CPU code for periodic microstructures uses a representation of these fields as an expansion in symmetry-adapted basis functions. In this case, N_f denotes the number of basis function used in the expansion, which is generally less than the number N_n of nodes in the FFT mesh by a factor approximately equal to the number of symmetry elements in the space group. The version of Anderson mixing in the GPU-accelerated code, however, uses a representation that does not impose any space group symmetry, for which $N_f = N_n$. The solution of an SCFT problem with a flexible unit cell must also satisfy equation 2.11 for each of N_c unit cell parameters, giving a system of $N_m N_f + N_c$ equations.

The resulting system of nonlinear equations can be expressed formally in all cases of interest as a requirement that

$$\mathbf{0} = \mathbf{R}(\mathbf{x}) \quad , \tag{2.12}$$

where $\mathbf{R}(\mathbf{x})$ denotes a column vector of residuals and $\mathbf{x}$ denotes vector of unknowns.

In the case of a rigid unit cell, $\mathbf{x}$ is a vector with $N_m N_f$ elements corresponding to the coefficients required to specify the N_m chemical potential fields, and $\mathbf{R}$ is a vector of $N_m N_f$ corresponding SCFT residuals. In the case of a flexible unit cell, $\mathbf{x}$ also contains an additional N_c elements given by the values of the unit cell parameters, while $\mathbf{R}$ contains an additional N_c elements containing derivatives of free energy with respect to particular unit cell parameters.

Anderson mixing is an iterative algorithm that retains a history of previous trial values of $\mathbf{x}$ and $\mathbf{R}$, and uses information from this history to construct new trial values of $\mathbf{x}$. The variant of the algorithm presented by Arora *et al.* [74] allows problems with fixed unit cell and flexible unit cells to be treated with analogous algorithms, simply by extending the number of elements in $\mathbf{x}$ and $\mathbf{R}$. After k steps of iteration, it retains a history of the K most recent previous values of $\mathbf{x}$ and $\mathbf{R}$. The number of previous trials retained is $K = \min(k+1, N_h)$, where N_h, the maximum history length, is a user-selected parameter. Storage of this history incurs a memory penalty of $\mathcal{O}(N_h N_f N_m)$. This is comparable to the memory required to store q and $q^\dagger$ in calculations with $N_h \sim N_s \sim 10^2$.

After the first N_h iterations, each iteration of the Anderson-mixing update algorithm as described by Stasiak and Matsen [77] requires computation of N_h inner products of pairs of residual vectors, at a cost of $\mathcal{O}(N_h N_f N_m)$. We achieved this time complexity by following their suggestion of storing the inner products of pairs of residual vectors.

In our implementation, these operations are performed on the GPU. While the Anderson mixing update algorithm constitutes only a small portion of the computation time in SCFT, we were able to obtain a modest additional speed-up in the GPU code by offloading these update operations to the GPU.

In contrast to the CPU code, which uses double precision, the GPU-accelerated code can be compiled in either single precision or double precision. For professional grade

GPUs that are designed for scientific computing, such as as NVIDIA's Tesla, double precision calculations take roughly twice as much time as corresponding single precision calculations. For more widely available GPUs that were not designed for computation, such as the GTX series, use of double precision can cause a slow down of 32-fold in the ideal case where everything else such as bandwidth is equal. The flexibility of our code reduces the burden of needing sophisticated hardware and thus allows efficient use of the code on more common, less expensive GPUs.

To further take advantage of our choice of hardware, we have also chose to limit the simulation grid to sizes of $N_n = 2^n$. This allows us to write GPU kernels that both require less communication time with the CPU and have a higher computational speed.

2.2 SCFT Code Performance

To ensure the efficacy of this code, it is important to address both the speed-up and the accuracy of the calculation. The performance of GPU-accelerated SCFT calculations are well documented by Delaney and Fredrickson [75] for their particular implementation. We have performed basic performance testing here as well, as our implementation of the field relaxation is somewhat different than Delaney and Fredrickson [75], and we also test their conjecture that single-precision codes can be polished to higher accuracy by a subsequent double-precision calculation. We further provide results for GPU-accelerated solutions for Frank-Kasper phases, which have very large unit cells.

For the purpose of comparing the older PSCF Fortran code to the new GPU code, we used the diblock case studies that are distributed with [50] as a benchmarking tool. The SCFT solution provides the free energy of a particular morphology with an optimized domain size, which allows for easy comparison between different implementations. The diblock case studies involve BCC, FCC, gyroid, A15, and the Frank-Kasper σ phase. Except where noted otherwise, each calculation proceeded until the root-mean-squared

		Computational Time [s] (# Iterations)			
Phase	Grid Size, N_n	Symmetry	No-Symmetry	GPU-D	GPU-S
BCC	32×32×32	27.9 (51)	80.7 (56)	5.4 (49)	4.3 (68)
FCC	64×64×64	256.9 (53)	580.9 (54)	20.3 (51)	11.0 (67)
A15	64×64×64	418.0 (84)	951.0 (93)	31.4 (79)	15.7 (92)
σ	64×64×32	372.0 (177)	846.3 (183)	41.9 (175)	21.2 (198)
Gyroid	32×32×32	21.7 (44)	47.4 (45)	4.9 (44)	3.7 (58)

Table 2.1: Grid size and computational time needed to reach convergence for each morphology using the three different SCFT implementations. The corresponding number of Anderson mixing iterations for each implementation is in parenthesis next to the computational time. The 'Symmetry' and 'No-Symmetry' implementations are CPU-based with the conditions as described in Section 2.2. 'GPU-D' and 'GPU-S' is the double precision and single precision, respectively, GPU-based implementation described in Section 2.1.

magnitude of elements in the residual vector $\mathbf{R}$, as defined by Arora *et al.* [50], is less than 10^{-5}. All calculations were performed with a Intel® Xeon® Processor E5-2630 v2 CPU, coupled with a Tesla K40 GPU for the GPU code. The computational time is taken from an average of three trials. All results reported here for a CPU program were obtained with the original Fortran PSCF code.

We performed four sets of calculations to benchmark the code. The first calculation (with the label 'Symmetry') uses the Fortran CPU code with the workflow that was recommended in [50] and simultaneous relaxation of the fields and unit-cell stress [74]. This calculation uses symmetry-adapted basis functions to represent all fields within the Anderson Mixing iteration algorithm, thus constraining the solution to have a specified space group symmetry [50]. We also examined the performance of the CPU code but with no imposed symmetry ('No-Symmetry'), by setting the space group to the identity group. Finally, we tested the performance of both double and single precision calculation on the GPU ('GPU-D' and 'GPU-S' respectively). The 'No-Symmetry' calculations yield the closest equivalence between the CPU and the GPU codes, since we have not yet

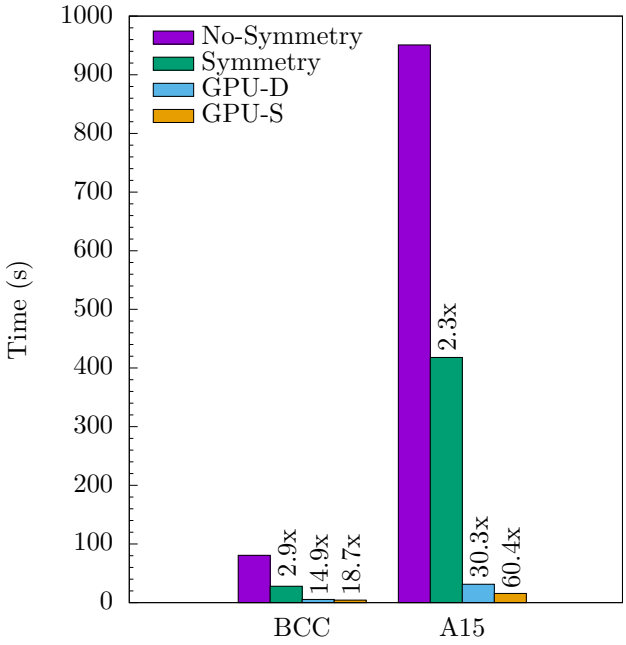

Figure 2.1: Execution time for the SCFT solution for the BCC and A15 phase. The labels above the bars corresponds to the speed-up, which is defined as time to compute the solution with no-symmetry constraints divided by execution time for the other approaches. The grid sizes and number of iterations for each solution are in Table 2.1, along with similar speed-up results for other morphologies.

implemented an iteration algorithm that enforces space group symmetry during iteration in the GPU-based code. The relative speed of the GPU code and CPU code with no imposed symmetry is thus the best measure of the speed-up obtained for identical algorithms as a result of the change in hardware alone. The speed of the GPU code relative to the CPU code with symmetry is instead the speed-up obtained for these crystal structures by switching to the current GPU code from the fastest available CPU implementation.

Figure 2.1 provides the computational time for two of the case studies, and Table 2.1 provides the computational time and the number of iterations needed to reach convergence for each of the case studies. Overall, the GPU-accelerated calculations are

much faster than the CPU calculations. The speed-up accrued by shifting to the double precision GPU-based SCFT code is around two orders of magnitude, about 30× for A15. The change from double precision to single precision provides an additional 2× speed up per iteration, consistent with our choice of GPU. Taking into account both the change in hardware and the use of single precision calculations, the magnitude of our largest speed-up is 60×, similar to that by Delaney and Fredrickson [75]. Speed aside, Anderson mixing is crucial to the SCFT solutions of Frank-Kasper phases because it is a Jacobian-free method, and thus uses much less memory than, for example, using a Newton-Raphson scheme to update the fields [50].

A common observation is that the relative speed-up obtained by using GPUs tends to increase up until the problem becomes large enough to hide latency. This is observed in our calculations of the case study examples where the largest speed-up are with examples of 64×64×64 grid size, while only moderate speed-up is seen for 32×32×32 grids. Note that, since the algorithm dictates that the computational grid is limited to sizes of 2^n, we slightly modified the unit cell of the PSCF-distributed case study example of BCC to 32^3 from the previous value of 36^3. The improvement with increasing grid size is especially important for SCFT solutions for Frank-Kasper phases, which have large unit cells with a large number of particles [82] and thus require many grid points to resolve the core-matrix interfaces of the particles.

The difference in speed between the 'Symmetry' and 'No-Symmetry' calculations is a result of the use of symmetry-adapted basis functions on the cost of the operations required for Anderson-Mixing update operations. In the CPU code, symmetry adapted basis functions are used to represent fields in the outer Anderson-Mixing iterator algorithm, but not within the pseudo-spectral algorithm used to solve the MDE. Use of symmetry-adapted basis functions thus has no effect on the time required to solve the MDE, but does affect the time required by the Anderson Mixing update operation itself,

because it drastically reduces the number of degrees of freedom required to represent the chemical potential field and the corresponding residual vector.

We have not yet implemented any symmetry constraints in the GPU-accelerated code. It is illuminating to estimate the speed-up that might be obtained if this feature were implemented. Comparing the 'Symmetry' and 'No-Symmetry' calculations reveals the effect of including symmetry-constrained basis functions in Anderson mixing. For example, the symmetry-adapted basis for the A15 'Symmetry' case reduces the 262 144 nodes to a mere 6 017 basis function coefficients, a 44× reduction. The use of basis functions allows inner products of residual vectors to be computed as summations over basis functions rather than summations over grid points, and dramatically reduces the number of unknowns in the required solution of a system of linear equations. The fact that the solution with 'Symmetry' is roughly twice as fast as the 'No Symmetry' case reflects the fact that, in the 'No Symmetry' case, the cost of these update operations has become comparable to the cost of the solution of the MDE, though the cost of the update operations becomes negligible for high symmetry (e.g., cubic) phases when symmetry is imposed. While these observations suggest that a further speed-up is possible by implementing these symmetry constraints within the GPU code, we do point out that the effectiveness of the GPU acceleration will be decreased concomitantly with the reduction in the number of equations to solve. Thus the speed-up is not multiplicative.

To ensure the accuracy of our calculations, we examined the resulting volume fraction profile for each block in the converged solution as well as the final free energies. Density profiles were examined using the visualizer developed for [50], which is also available online [51]. In all cases, the converged solutions were found to yield the expected morphology. The free energies obtained from the CPU and GPU codes were very similar, with the largest fractional error in free energy for both double precision and single precision GPU calculations with respect to the 'Symmetry' calculation being an order

of magnitude less than the convergence criteria described earlier.

For cases where speed is the key criterion, our results indicate that single precision GPU calculations are preferred. However, there are situations where higher accuracy may be required, for example when comparing different Frank-Kasper phases with nearly degenerate free energies [20]. Delaney and Fredrickson [75] proposed that the solution generated by a single precision GPU calculation could be used as the initial condition for a subsequent double precision calculation to provide the desired accuracy while retaining the speed of the original GPU calculation during the early stages. We tested this proposition by first computing a single precision GPU calculation to the standard tolerance of 10^{-5} for our work, and then using that solution with a double precision GPU calculation to reach a tolerance of 10^{-6}. The timing results of this calculation are the 'Refine' method in Fig. 2.2. We then repeated the calculation by performing it entirely in double precision, which is denoted as the 'Direct' method in Fig. 2.2. Both methods lead to similar run-times. Note that the comparison in Fig. 2.2 uses identical Anderson mixing parameters when switching from single precision to double precision, and none of the history information from the single precision calculation is transferred to the double precision calculation. Some additional speed-up of the 'Refine' calculation might be possible by additional optimization of the algorithm.

2.3 MC-FTS algorithm and implementation details

If one were interested in the effects of fluctuation in the system, they would have to solve Eq. 2.1 without taking the fluctuating fields to their extremum value. In principle, one could sample both sets of field through some Monte-Carlo method but, in practice, the fluctuations in W_+ suffer from a numerical problem known as the "sign problem" [83]. In MC-FTS, this issue is resolved by allowing the composition field to fluctuate but taking the pressure field to its extremum value. This works surprisingly well due to the

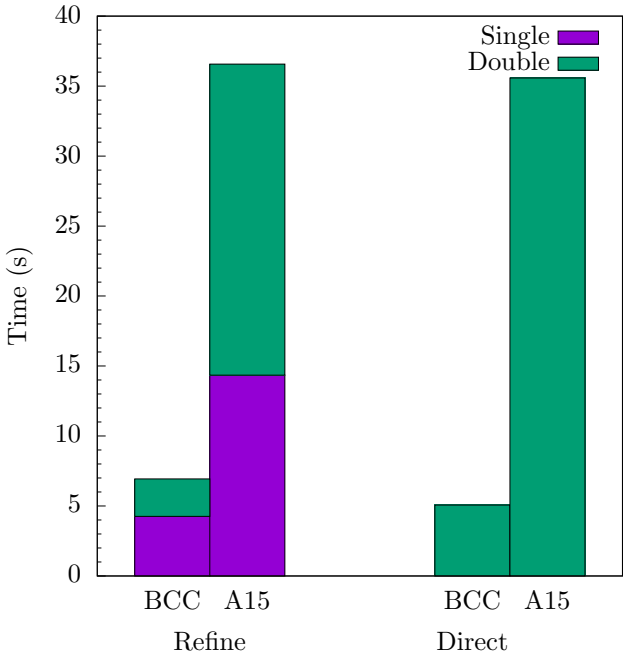

Figure 2.2: Execution time for the SCFT solution for the BCC and A15 phase with a convergence criteria of 10^{-6}. The set of histograms labeled 'Refine' is the time taken to run a single precision solver to an accuracy of 10^{-5} and then refine that solution to an accuracy of 10^{-6} using the double precision solver. The set labeled 'Direct' is the time taken using a double precision solver from the outset.

low correlation time in the sampling of W_+ [83] and has seen increasing use of recent times due to improvement in computational power [83–87].

Our implementation of MC-FTS follows closely that of Stasiak and Matsen [84]. The partition function in MC-FTS with only one fluctuating field is,

$$Z \sim \int \exp\left(\frac{H[W_-, w_+]}{k_B T}\right) DW_- \tag{2.13}$$

whose Hamiltonian, H, given in Eq. 2.2 is governed by a fluctuating composition field W_- and the mean-field pressure field w_+. The algorithm proceeds to calculate the single chain partition function and density field as per Eq. 2.7-2.8. The solution of the modified

diffusion equation is then obtained pseudo-spectrally, and Anderson Mixing [77] was used to modify w_+ in obtaining the corresponding extremum pressure field for the given composition field. By taking only the extremum of W_+, the definition of the deviation in Anderson Mixing constrains the system to satisfy only the condition of incompressibility [86], i.e. $\rho_A(\mathbf{r}) + \rho_B(\mathbf{r}) = \rho_0$ with $\phi_\alpha(\mathbf{r})$ defined as $\rho_\alpha(\mathbf{r})/\rho_0$, where $\rho_\alpha(\mathbf{r})$ is the local α-monomer density.

The fluctuations in composition field are sampled using a standard Metropolis Monte Carlo algorithm. Moves in the composition field are accepted by computing the change in the Hamiltonian,

$$\Delta H = H[W_- + \Delta W_-, w_+ + \Delta w_+] - H[W_-, w_+] \tag{2.14}$$

and then setting the probability of acceptance for a given move of ΔW_- as $\min(1, \exp[-\Delta H/k_BT])$. Note that the extensive Hamiltonian is used for the Monte Carlo acceptance criterion in Eq. 2.14, rather than the intensive form given by Eq. 2.2. At each Monte Carlo step, two different types of moves are performed alternately [84]. The first type is a real space move chosen from a uniform distribution $\Delta W_-(\mathbf{r}) \in [-A_1, A_1]$ at each grid point. The second move is a collective move in Fourier space, $\Delta W_-(q) \in [-A_2[S_{\mathrm{FH}}(q)]^{1/2}, A_2[S_{\mathrm{FH}}(q)]^{1/2}]$ with $S_{\mathrm{FH}}(q)$ being the Fredrickson-Helfand structure factor, [32] as suggested in previous work for accelerating sampling rate [84]. Both A_1 and A_2 are constants chosen to maintain about 40% acceptance rate and need to be tuned for a given system.

As a fluctuating field theory, the value of χN in MC-FTS has to account for the ultraviolet divergence effect present in low $\bar{N}$ systems [84, 85, 88–90]. We define χN_{bare} as the input parameter to MC-FTS and an effective interaction parameter, χN_{eff}, as the interaction parameter that is used in comparison to theory and experiment. We use the

definition from Vorselaars et al. [85],

$$\chi N_{\text{eff}} = \left[1 - \ell \frac{R_0^2 \int S_{\text{RPA},0}(q,\epsilon) d\mathbf{q}}{(2\pi)^3 \rho_0 N f_A (1 - f_A)} \right] \chi N_{\text{bare}} \tag{2.15}$$

where $S_{\text{RPA},0}(q,\epsilon)$ is the athermal RPA structure factor at a given value of ϵ [91, 92] and $\ell = R_0 \bar{N}^{-1/2}$ where $R_0 = N^{1/2} b$ is the end-to-end length of the polymer chain. We chose this definition of χN_{eff} since those authors [85] have shown that this choice of χN_{eff} is effective at culling the ultraviolet divergence for low $\bar{N}$ diblock copolymers. Unless otherwise noted, any use of the symbol χN henceforth for MC-FTS calculations is equivalent to χN_{eff}.

Our implementation of MC-FTS is run for at least 5×10^5 iterations to first equilibrate the system and is followed by 3.5×10^6 iterations to obtain the relevant statistics. Statistics are sampled every 10^3 iterations. To ensure the correctness of our implementation, we repeated a set of calculations by a previous work demonstrating the implementation of MC-FTS [85] and found negligible difference as shown in Fig. 2.3.

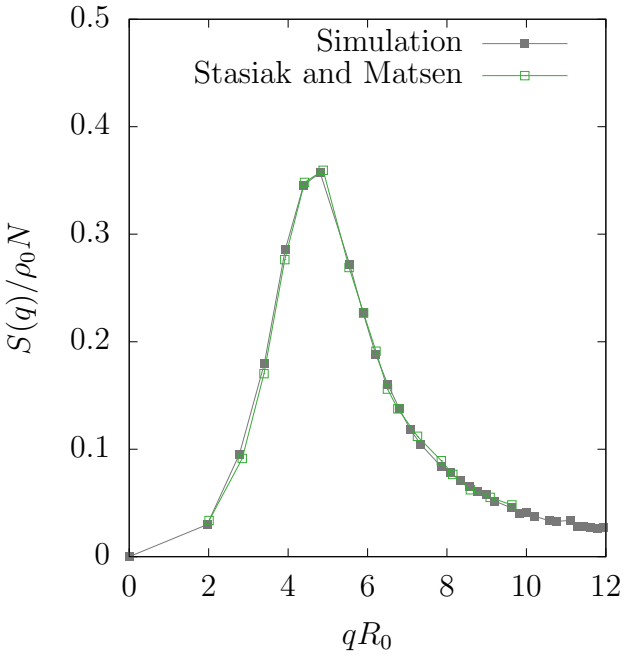

Figure 2.3: Structure factor versus normalized wavenumber, qR_0, for $\chi N = 10$, $\bar{N} = 10^4$, $f_A = 0.5$ and $V = 3.2^3$. The solid box are results from our implementaion of MC-FTS and the empty boxes are the result presented in Fig. 2 of Vorselaars and Matsen [85].

Chapter 3

Symmetry breaking in particle-forming diblock polymer/homopolymer blends[1]

Compositionally asymmetric AB diblock polymers form micelles with the minority A-block in the core to minimize enthalpically unfavorable A/B contacts. When a melt of these polymers is cooled below the order-disorder transition temperature, the micelles undergo a first-order phase transition and order on a lattice. Theory and experiments in the past four decades indicated that these particles form a body-centered cubic (bcc) phase (Fig. 3.1) throughout much of the sphere-forming region of the phase diagram [27, 92] with a small region of face-centered cubic (fcc) packing near the order-disorder transition [93, 94]. The discovery of a Frank-Kasper σ phase (Fig. 3.1) in a diblock copolymer melt in 2010 [14] upended the conventional wisdom that these materials only form close-packed structures. Typically found in metals and metallic alloys [12, 13],

[1]This chapter is adapted from Guo Kang Cheong, Frank S. Bates and Kevin D. Dorfman, Proceedings of the National Academy of Sciences USA 117, 16764-16769 (2020)

Frank-Kasper phases are tetragonally close-packed structures consisting of combinations of 12-sided, 14-sided, 15-sided and 16-sided polyhedra. These building blocks can be arranged in a vast number of ways, with 27 known Frank-Kasper phases, and other packings proposed but not yet observed in nature [82]. Since the original discovery of the σ phase in block copolymer melts [14], three other Frank-Kasper phases have been identified: A15 [15, 16, 19], C14 [17, 20, 21] and C15 [20, 21]. C14 and C15 are also known as Laves phases, a subset of Frank-Kasper phases consisting of only Z12 and Z16 polyhedra (Fig. 3.1). Frank-Kasper phases are periodic approximants to quasicrystals, and a dodecagonal quasicrystal, associated with the σ phase, has been observed as well in diblock copolymer melts [22]. In addition to block polymers, Frank-Kasper phases and quasicrystals have been reported in a wide range of other soft materials, including dendrimers [95, 96], liquid crystals [97–101] and shape amphiphiles [102, 103], including a notable discovery of the Z-phase in the latter [104]. With the existence of Frank-Kasper phases in soft matter now firmly established, the challenge has moved towards understanding the factors giving rise to these low-symmetry phases over high-symmetry, close-packed structures like bcc.

In the context of neat linear diblock copolymer melts, there now exists evidence supporting three independent factors giving rise to Frank-Kasper phases. First, these phases only emerge for conformationally asymmetric block polymers, where the block comprising the matrix is stiffer (i.e., characterized by a smaller volume normalized statistical segment length) than the core block [15, 18, 31, 72, 105]. For such systems, the borders of the Voronoi cells are imprinted on the core-matrix interface. The interfacial and corona distortion alters the delicate balance of interfacial tension and chain stretching that otherwise favors close-packed spheres when the matrix is soft, and selects packings with higher sphericity [69]. Second, owing to the nearly degenerate free energies of different Frank-Kasper phases in diblock polymers [20, 72], thermal processing can access

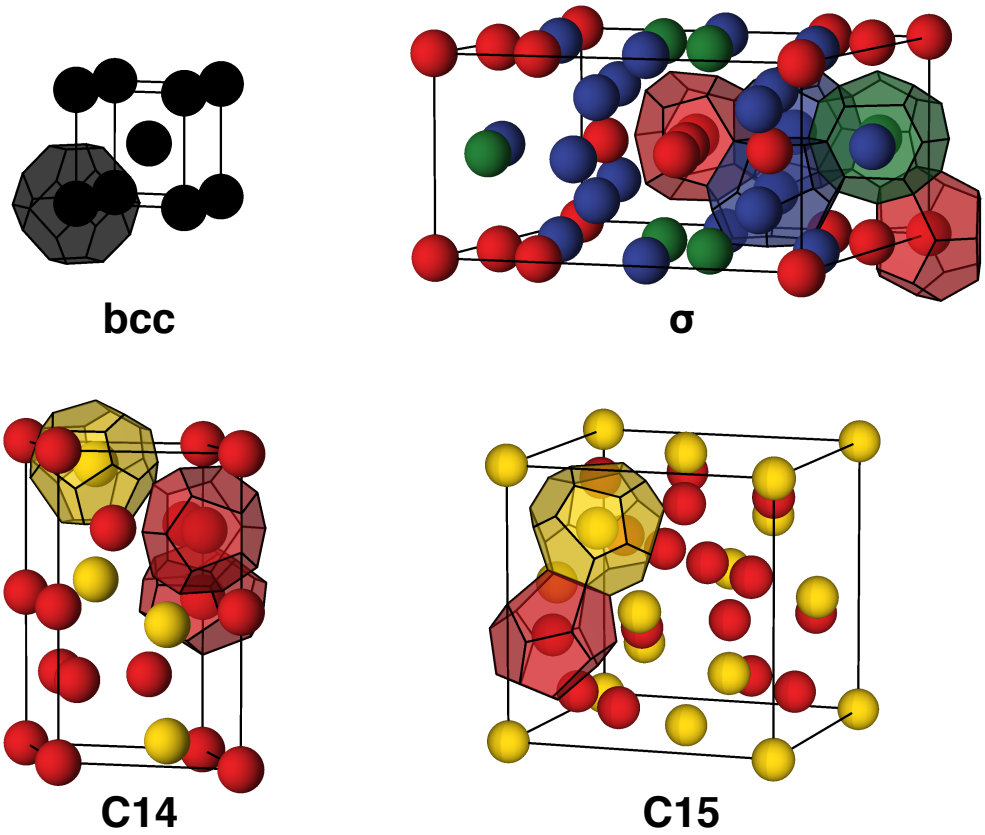

Figure 3.1: Illustration of the unit cells for a body-centered cubic (bcc) phase, the Frank-Kasper σ phase, and the C14 and C15 Laves phases. Particle colors correspond to Z8 (black), Z12 (red), Z14 (blue), Z15 (green) and Z16 (yellow). Illustrative polyhedra are included for each particle type.

different ordered states [20, 21], with the C14 and C15 Laves phases being accessible to date in the neat melt state only by thermal processing. Third, there is evidence that lower molecular weight systems, which increase the self-concentration of the chains, also stabilize Frank-Kasper phases [28]. However, the appearance of Frank-Kasper phases within the context of self-consistent field theory (SCFT) calculations [20, 31, 72], which are only strictly valid as the degree of polymerization $N \rightarrow \infty$, indicates that high self-concentration is not a necessary condition for Frank-Kasper phase formation.

While further increasing conformational asymmetry or exploiting different processing paths are feasible approaches to widen the range of diblock copolymer compositions and temperatures that produce Frank-Kasper phases, blending provides considerably more versatility within a relatively straightforward experimental platform. For example, experiments performed with blends of lamellar-forming diblock polymer and a disorder-forming diblock polymer furnished two Frank-Kasper phases, σ and A15, and a dodecagonal quasicrystal [106]. Related SCFT calculations [21, 70, 107] reveal that blending two diblock copolymers with different molecular weights and volume fractions of the minority block can substantially increase the region of the phase space where Frank-Kasper phases are stable. In the blended system, the two different block copolymers tend to reside at different locations within the particles [70] to minimize the chain stretching penalty for reaching the edges of the Voronoi cells.

Blending a diblock copolymer with a homopolymer also leads to the emergence of Frank-Kasper phases. Experiments have probed the addition of homopolymer that is similar to the molecular weight of either the matrix block [73] or the core block [108]. In the former case, the addition of the matrix homopolymer lead to the formation of a σ phase. In the latter case, the system underwent a sequence of transitions from bcc to σ to C14 to C15 with the addition of core homopolymer in the dry brush regime [109], i.e., when the core homopolymer is of similar length to the core block [108]. Reducing

the molecular weight of the homopolymer loaded into the cores of the micelles shifted the system into a wet brush regime, wherein the only ordered states observed were bcc and hexagonally-packed cylinders (hex) [108]. These experiments [108] used a diblock copolymer that produced only a bcc phase in the neat melt state [28], indicating that high conformational asymmetry is not a prerequisite for Frank-Kasper phase formation during blending with a homopolymer.

SCFT provides an ideal platform for understanding the symmetry breaking in blends of AB diblock polymers with A homopolymers by facile discrimination of the placement of A-block and A-homopolymer chains within the domains. Zhao and Li [36] used SCFT to examine the phase behavior of AB_4 miktoarm polymers under the addition of A-homopolymer, where the homopolymer is at least as long as the A-block and thus deep into the dry brush regime [109]. In a neat melt, the high conformational asymmetry of an AB_4 miktoarm polymer exhibits a sequence of fcc to bcc to σ to A15 [36], corresponding to an increasing average isoperimetric quotient and consistent with the arguments of sphericity [69]. Addition of A-homopolymer leads to the emergence of both C14 and C15 Laves phases, accompanied by changes in the volume asymmetry of the particles, the various contributions to the free energy, and the distributions of the different components within the domains [36]. In the present contribution, we build on these initial observations [36] to provide a deeper understanding of the emergence of different Frank-Kasper phases in experiments on diblock polymer/homopolymer blends [108].

3.1 Methods

The SCFT calculations first use a set of canonical ensemble calculations to identify the stable phase on the assumption of a single-phase system (Appendix Tables A.1-A.10). Subsequent grand canonical ensemble calculations were performed to locate the

phase boundaries and two-phase regions [110]. The calculations consider eight candidate phases: disorder, bcc, fcc, σ, A15, C14, C15, and hexagonally-packed cylinders (hex). Canonical ensemble calculations were performed for homopolymer degrees of polymerization $N_{\mathrm{H}} = 0.12N$, $0.14N$ and $0.18N$, where N is the block polymer degree of polymerization, with block polymer volume fractions from $\phi_1 = 0.70$ to $\phi_1 = 1.00$ at an A-block volume fraction of $f_{\mathrm{A}} = 0.18$ and $\chi N = 20$, 25 and 30, where χ is the Flory-Huggins parameter, for $\epsilon = 1.7$. Additional calculations were performed for $\chi N = 25$ at $\epsilon = 1$ (Appendix, Fig. A.3B). The SCFT calculations used an integration step of $\Delta s = 0.01$ and a convergence criterion of 10^{-5} as defined in Ref. 74. Grid sizes of $64 \times 64 \times 64$ were used for all 3D phases with the exception of σ phase at $96 \times 96 \times 48$. A grid size of 64×64 was used for the 2D calculation for the hex phase. Further refinement of the grid sizes up until $96 \times 96 \times 96$ to resolve the free energy differences between the nearly degenerate C14 and C15 phases at $\alpha = 1$ shows no difference in their relative stability. The differences in free energies are all larger than the convergence criterion of 10^{-5} based on the algorithm of Ref. 74.

3.2 Results

We have performed SCFT calculations for a system that mimics the experiments of Mueller *et al.* [108] on poly(styrene-*b*-1,4-butadiene) block polymers blended with poly(1,4-butadiene) homopolymer. The minority A-block in their experiments is poly(1,4-butadiene), with a volume fraction $f_{\mathrm{A}} = 0.18$. The ratio of statistical segment lengths $b_{\mathrm{A}}/b_{\mathrm{B}} = 1.31$, where b_i is the statistical segment length of block i [28]. The corresponding conformational asymmetry of $\epsilon \equiv (b_{\mathrm{A}}/b_{\mathrm{B}})^2 = 1.7$ is insufficient to form a Frank-Kasper phase in SCFT [31] or in experiments on the neat diblock polymer melt [28]. The experimental system is thus significantly different than the AB_4 miktoarm/A homopolymer system examined previously by SCFT [36], as both theory [31, 36, 105] and experiments [15]

indicate Frank-Kasper phases form in neat melts of miktoarm copolymers because the branches in the matrix impart a very high degree of conformational asymmetry.

We examine here the phase behavior of this system at the fixed value of $\chi N = 25$, where χ is the Flory-Huggins parameter and N is the degree of polymerization of the diblock polymer, for different values of the volume fraction of the block polymer, ϕ_1, down to $\phi_1 = 0.70$. At $\chi N = 25$, SCFT predicts that the neat diblock copolymer melt is fcc. The fcc-bcc two phase window only occupies less 1% of the phase diagram and is immediately overtaken by bcc at higher values of ϕ_1. As expected [93], increasing to $\chi N = 30$ (Appendix, Fig. A.1A) produces a bcc state in the neat melt and lowering to $\chi N = 20$ (Appendix, Fig. A.2B) produces a disordered melt.

Figure 3.2 furnishes phase diagrams for three different degrees of polymerization N_{H} of the homopolymer, where $\alpha = N_{\mathrm{H}}/f_{\mathrm{A}}N$ represents the ratio of the degree of polymerization of the A-homopolymer to the A-block [108]. For $\alpha = 1$, the system is in the dry brush limit, where penetration of the homopolymer into the space occupied by the associated block is limited. Past the narrow window of fcc stability, the phase sequence of bcc to σ to C14 to C15 qualitatively agrees with experiments obtained at $\alpha = 1.08$ [108], with the caveat that the experimental sequence of phases was obtained by simultaneously decreasing ϕ_1 and increasing temperature, which may be related to the fluctuation-induced stabilization of Frank-Kasper phases [15] that is neglected in SCFT. Eventually, SCFT predicts that the system macroscopically phase separates into C15 and a disordered homopolymer-rich phase, consistent with experiments [108] on this system and SCFT results obtained for AB_4 miktoarm polymers [36]. While canonical ensemble calculations produce a C14 phase within the two phase window, the concomitant grand canonical ensemble calculations reveal that the C14/homopolymer and C15/homopolymer tie lines are indistinguishable. We thus posit that the equilibrium two-phase system is C15/homopolymer, but caution that the free energy differences

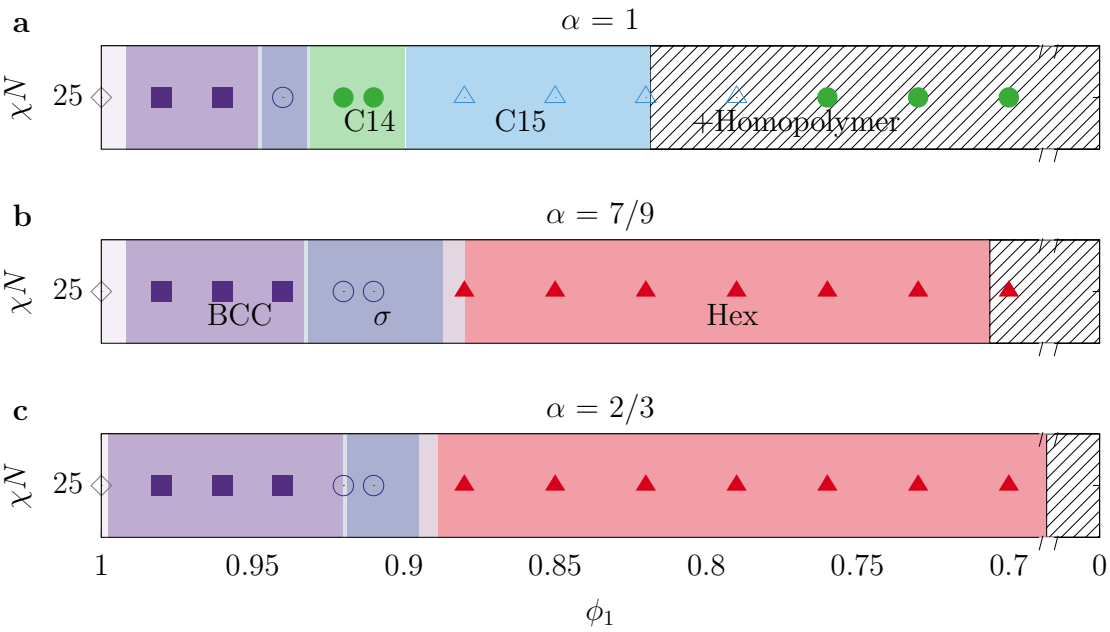

Figure 3.2: SCFT phase diagram for blending of an AB diblock polymer with A homopolymer for different ratios $\alpha = N_H/f_A N$ of the degree of polymerization of the A-homopolymer to the A-block and volume fractions ϕ_1 of the diblock copolymer: (a) $\alpha = 1$, (b) $\alpha = 7/9$, and (c) $\alpha = 2/3$. The symbols indicate state points for SCFT calculations in the canonical ensemble. Phase boundaries between these state points were obtained by grand canonical ensemble calculations. Symbols correspond to fcc ($\diamond$, gray), bcc ($\blacksquare$, dark purple), σ ($\bigcirc$, light purple), C14 ($\bullet$, green), C15 ($\triangle$, blue), and hexagonally-packed (hex) cylinders ($\blacktriangle$, red) obtained from canonical ensemble calculations. A15 was also a candidate phase but no regions of A15 stability were observed. Phase boundaries between states were obtained from grand canonical ensemble calculations. Two-phase regions between ordered states are indicated by light shading; in many cases, these regions are too narrow to be depicted. The hashed areas indicate two-phase regions that correspond to equilibrium between an ordered phase and a disordered phase.

between these two possibilities are small (Appendix, Tables A.1-A.3). Additional calculations at $\chi N = 20$ (Appendix, Fig. A.2B) show a similar sequence of phases, but with a disordered neat melt and fcc as the classic sphere-forming phase rather than bcc, and $\chi N = 30$ (Appendix, Fig. A.1) produces only bcc followed by the Frank-Kasper phase sequence. Likewise, calculations at $\chi N = 25$ for the conformationally symmetric case $\epsilon = 1$ (Appendix, Fig. A.3B) produce bcc followed by the same progression of Frank-Kasper phases upon addition of homopolymer, indicating that conformational asymmetry is not a necessary condition. Moreover, the neat diblock melt for $\epsilon = 1$ produces bcc, indicating that conformational asymmetry is required to produce the fcc phase in Fig. 3.2 and Appendix Figs. A.1A and A.2B.

As the homopolymer molecular weight decreases to $\alpha = 7/9$, Fig. 3.2b indicates a loss of the C14 and C15 phase and the emergence of a hexagonally packed cylinder phase (hex) over a large range of ϕ_1 that we examined. Continued reduction of the degree of polymerization of the homopolymer to $\alpha = 2/3$ in Fig. 3.2c leads to further extinction of the Frank-Kasper phase. This phenomena is consistent with experiments at $\alpha = 0.6$ and has been attributed to a transition from dry to wet brush behavior [108]. Qualitatively similar behavior occurs at a lower $\chi N = 20$ (Appendix, Fig. A.2b). When $\epsilon = 1$ and $\chi N = 25$ (Appendix, Fig. A.3b), the extinction of Frank-Kasper phases with decreasing α is even more pronounced, consistent with the ability of conformational asymmetry to stabilize Frank-Kasper phases [31].

Overall, the SCFT calculations capture the salient aspects of the experimental phase behavior, namely the sequence of the Frank-Kasper phases as the volume fraction of homopolymer increases and the transition from Frank-Kasper particle phases to a cylindrical phase as the homopolymer degree of polymerization decreases. SCFT does not provide a quantitative prediction of the stability windows for Frank-Kasper phases due to their nearly degenerate free energies (Appendix, Tables A.1-A.10), consistent with

prior work [15, 20, 21, 31, 57, 111].

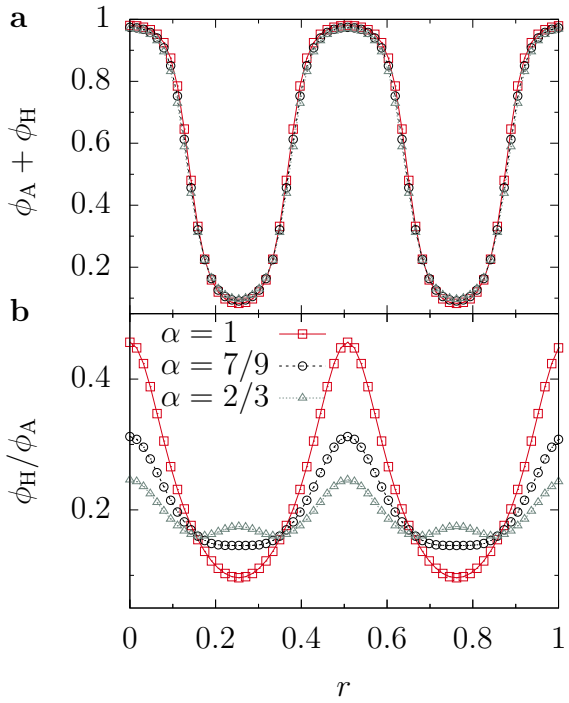

Figure 3.3: Illustration of the transition from the dry brush to wet brush regimes as the homopolymer molecular weight decreases at $\chi N = 25$. (a) Volume fraction of the A monomers in the bcc phase at $\phi_1 = 0.97$ along the [111] direction for $\alpha = 1$ (red squares), $\alpha = 7/9$ (black circles), and $\alpha = 2/3$ (green triangles), where the position is made dimensionless with $\sqrt{3}a$ for the unit-cell parameter a. (b) Ratio of the A-homopolymer to A-block volume fractions for the conditions in (a).

To investigate further the transition between wet and dry brush regimes, Fig. 3.3 examines the volume fractions ϕ_A and ϕ_H of the A-block and homopolymer repeat units, respectively, along the [111] direction of the bcc phase, which is the simplest case to analyze, at a block polymer volume fraction of $\phi_1 = 0.97$. As the homopolymer degree of polymerization N_H increases, Fig. 3.3a indicates that the cores of the micelles swell slightly, using $\phi_A + \phi_H = 0.5$ as a reasonable cutoff for the A-rich region of the micelle. While the swelling effect is small, the increase in the apparent degree of segregation is more significant. The origin of the increased segregation is a dewetting of the A/B

Table 3.1: Total volume fraction of the A monomers, $\phi_A + \phi_H$, at the center of the micelles (i.e., the Wykoff positions) for the dry brush case $\alpha = 1$ and $\chi N = 25$. Results correspond to canonical ensemble SCFT calculations appearing in Fig. 3.2.

Phase	ϕ_1	Wykoff Position	Polyhedron	$\phi_A + \phi_H$
bcc	0.97	—	Z8	0.980
σ	0.94	2b	Z12	0.988
		4f	Z15	0.992
		8i	Z12	0.988
		8i'	Z14	0.991
		8j	Z14	0.991
C14	0.92	2a	Z12	0.993
		4f	Z16	0.997
		6h	Z12	0.993
C15	0.85	8a	Z16	0.999
		16d	Z12	0.999

interface of the micelles as N_H increases, with Fig. 3.3b demonstrating a significant increase in the homopolymer segregation towards the core of the micelle [109]. The observation of increased wetting of the brush with decreasing homopolymer molecular weight, and the eventual formation of a cylindrical phase in Fig. 3.2 for the shorter homopolymers, is consistent with the wet brush model proposed by Mueller *et al.* [108], and thus consistent with their rationale for the emergence of a hex cylinder phase. Similar results are obtained at $\chi N = 20$ (Appendix, Fig. A.2A) and for $\epsilon = 1$ at $\chi N = 25$ (Appendix, Fig. A.3A).

The apparent increase in segregation strength in the dry brush regime observed in Fig. 3.3 for bcc is maintained for the Frank-Kasper phases. Indeed, Table 3.1 shows that the ejection of the B-block from the particle core is even stronger for the Frank-Kasper phases, with an increase from a total A volume fraction 0.980 for bcc to up to 0.999 for the Z16 particles in C15. The particle centers are defined by their Wykoff positions, which are unaffected by the addition of homopolymer (Appendix, Figs. A.4 and A.5). Similar to what was observed in Fig. 3.3 for bcc, the purity of the A-polymers at the

center of the particles is driven by partitioning of the homopolymers to the particle core and the A-block towards the perimeter of the particle core. Owing to the distorted shapes of the polyhedra in Frank-Kasper phases [69], it is not straightforward to analyze the homopolymer and block polymer volume fractions in a manner akin to what we did for bcc in Fig. 3.3. Figure 3.4 provides an alternate approach by examining the volume distribution for the σ phase in the (001) plane, which slices through four of the five different particle types in the σ phase. The trend is analogous to what was observed for bcc, with significant partitioning of the homopolymer to the interior of the particles.

Figure 3.4 suggests that the effect of the partitioning of homopolymer to the particle center is stronger for a Frank-Kasper phase than for bcc. To investigate this point further, Fig. 3.5 compares the relative volume fraction of the homopolymer at the center of each particle in the dry brush limit to the total volume fraction of A-polymers. Similar results are obtained at other conditions (Appendix Figs. A.1B, A.2C and A.3C). Overall, Frank-Kasper phases exhibit an increase in the homopolymer volume fraction at the particle center of circa 50% when compared to bcc. Interestingly, the homopolymer volume fraction for a given phase is a monotonically increasing function of the coordination number of the number of faces in the polyhedra, which are themselves increasing in volume with increasing coordination number [36, 69]. Similarly, the 12-sided polyhedra contain a higher volume fraction of homopolymer in the centers of the particles in the Laves C14 and C15 phases than the Frank-Kasper σ phase, which arises in part due to the increased homopolymer volume fraction when the Laves phases are stable and is consistent with the larger volume asymmetry amongst different particles in the Laves phases [20].

To understand the relative partitioning of the homopolymer between different types of particles within a single phase, Fig. 3.6 tracks the evolution of the homopolymer volume fraction at the centers of the C15 particles in its relatively wide stability region for α

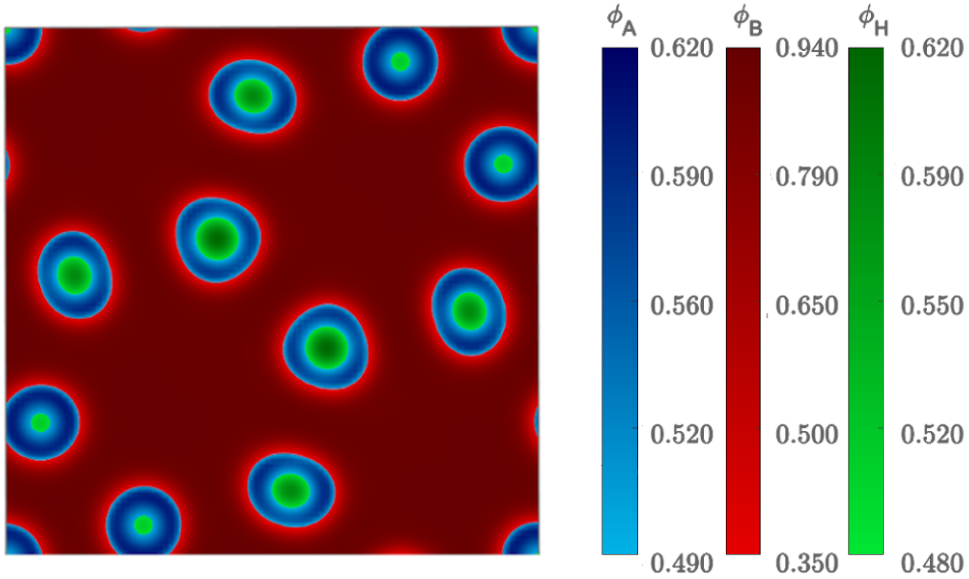

Figure 3.4: Volume fraction distribution in the (001) plane for the σ phase for the dry brush case $\alpha = 1$ and block polymer volume fraction $\phi_1 = 0.94$ at $\chi N = 25$. The 2b particle is on the corners, four of the 8i particles are proximate to the edges of the unit cell, two 4f particles are near the center, and four 8i' particles comprise the remainder of the particles in the image. Note that the (001) plane slices these particles at different distances from their centers, and that the A/B interfaces of the particles themselves are asymmetric. The A-rich regions of the 8j particles do not intersect this plane. The transition between colors is selected to highlight different components in different locations.

= 1, which clearly illustrates the basic phenomena. At the onset of the stability window, the larger Z16 particle has approximately 17% higher volume fraction of homopolymer than the smaller Z12 particle, indicating a preferential loading of the larger particle first. As the homopolymer volume fraction increases, the relative differences in homopolymer volume fraction at the particle centers decrease to approximately 5%. Similar results are obtained at other conditions (Appendix Figs. A.1C, A.2D and A.3D).

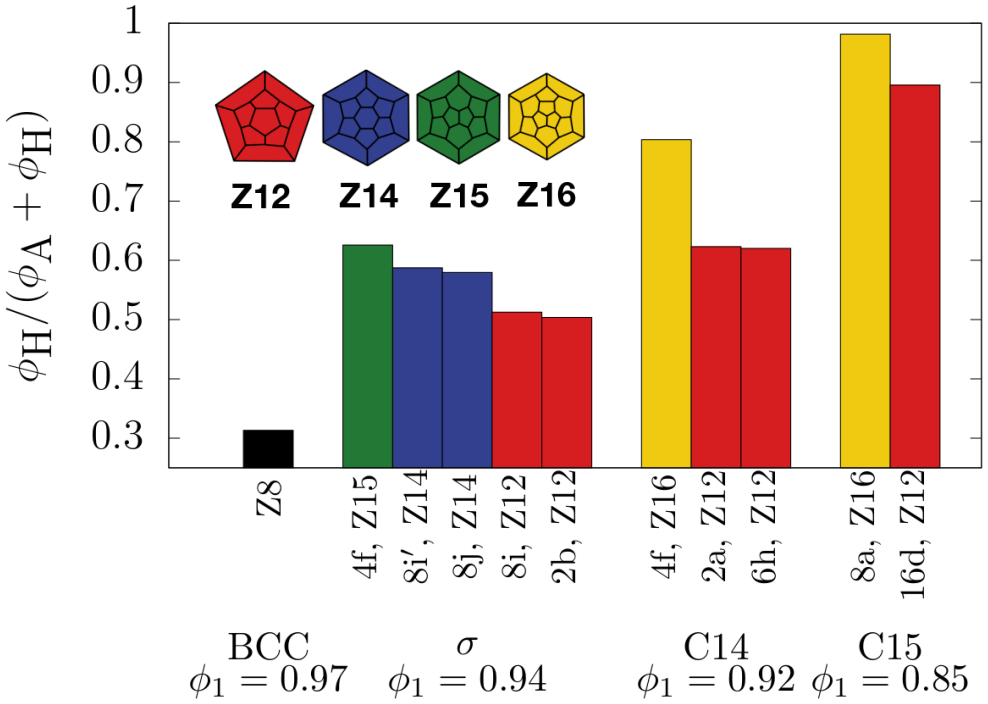

Figure 3.5: Volume fraction of the homopolymer, ϕ_H, relative to the total volume fraction of A monomers at the center of a micellar particle, $\phi_A + \phi_H$, for the dry brush case $\alpha = 1$ at $\chi N = 25$. Results correspond to canonical ensemble SCFT calculations appearing in Fig. 3.2. The notation refers to the Wykoff positions of the particles and the number of faces in the polyhedra. The inset shows the planar graph forms of each of the polyhedra.

3.3 Discussion

The key issue posed by our SCFT calculations and the related experiments by Mueller *et al.* [108] is understanding the origin of the transition from bcc to σ to C14 to C15 upon the addition of homopolymer to the cores of the micelles in the dry brush limit. Explanations proposed for the formation of Frank-Kasper phase in other diblock copolymer systems are unlikely to be applicable to the present case. The conformational asymmetry mechanism [31], which has been particularly powerful in explaining the formation of Frank-Kasper phases in neat diblock copolymer melts [14, 15, 20], cannot provide a

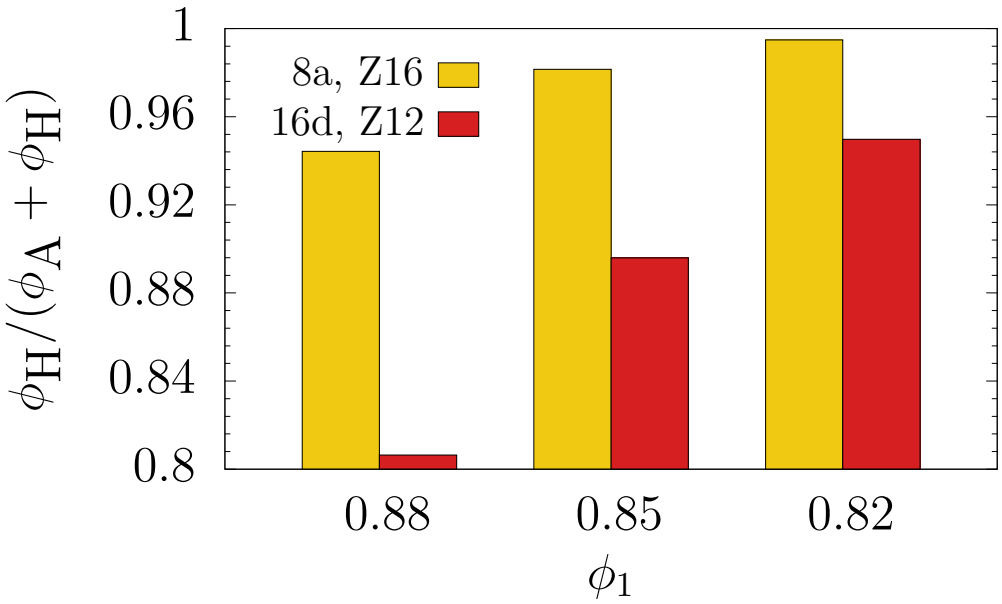

Figure 3.6: Volume fraction of the homopolymer, ϕ_{H}, relative to the total volume fraction of A monomers at the center of the micellar particle, $\phi_{\mathrm{A}} + \phi_{\mathrm{H}}$, for C15 for $\alpha = 1$ and $\chi N = 25$ due to the addition of homopolymer. The color coding corresponds to Fig. 3.5.

mechanism for their formation in this blended system; the stiffness of the matrix chains is imposed by the corona block chemistry and is unaffected by additives to the micelle cores. The addition of homopolymer does swell the micelle core [36], and it is tempting to propose that the swelling leads to compression of the matrix chains, which then imprints the shape of the polyhedra more strongly on the A/B interface. However, the system can relieve any such compression by expanding the unit cell size, which is indeed the case in our calculations (Appendix Figs. S6 and S7). Likewise, the basis for the enhanced stability of Frank-Kasper phases in blends of two diblock copolymers [21,70,107], which relies on the different block polymers partitioning within the particles to relieve chain stretching, cannot be the stabilizing mechanism in the presence of homopolymer, which simply partitions into the core and pushes the A-block towards the perimeter.

We thus seek an alternate mechanism for stabilization of Frank-Kasper phases upon the addition of homopolymer to micelles where the core and matrix blocks are of similar stiffness, i.e. for low conformational asymmetry. We posit that the increasing volume asymmetry of the particles in the different particle-forming phases explains the order of their progression. The preferred ordered particle-forming state at the conformational asymmetry $\epsilon = 1.7$ and $\chi N = 25$ is fcc. Now consider what happens upon the addition of a small amount of homopolymer. If one cannot resolve the homopolymer from the core block, the data in Fig. 3.3 would lead one to interpret the system as a higher degree of segregation, or equivalently a higher χN. This effect produces the bcc phase, which is the preferred packing for a neat melt with low conformational asymmetry [31] but at a higher χN (Appendix, Fig. A.1A). As additional homopolymer is added and partitions towards the core of the bcc particle, it eventually reaches a solubility limit. At this point, the system is confronted with two options: macroscopic phase separation or an order-order transition to a Frank-Kasper phase. The system selects a transition to the σ phase. The selection of σ is, at first glance, analogous to its selection

by conformationally asymmetric diblock polymers as χN increases [31]. However, the symmetry breaking mechanism differs for the blended system. While the morphology of the σ phase is dramatically different than bcc, it has the least particle volume asymmetry amongst the Frank-Kasper phases observed here [36], with the relative volumes all lying between 91.0% and 106.5% of the mean [69]. Figure 3.5 further indicates a relative partitioning of the homopolymer into the higher coordination number 4f particle, which is also the largest particle [69]. We did not observe a stable region of A15, which is consistent with our argument; the two particles in A15 are of lower coordination number (Z12 and Z14) and very similar in relative volume (100.8% and 97.7%) [36]. We posit that this soft matrix prefers bcc and will only transition to a Frank-Kasper phase that offers sufficient volume asymmetry to accommodate the additional homopolymer. Once the particles in σ are saturated with homopolymer, the system selects the next highest volume asymmetry (C14; relative volumes between 113.9% and 92.8% [36]) and the process repeats again to yield C15 (relative volumes of 114.2% and 92.2% [36]). At this point, there is no known Frank-Kasper phase in block polymers with a higher volume asymmetry. Under the addition of even more homopolymer in the dry brush limit, the system is then forced to undergo macroscopic phase separation. This partitioning mechanism is robust with respect to χN (Appendix, Figs. A.1B and A.2C) and conformational symmetry (Appendix, Fig. A.3C).

The SCFT results obtained here for a system with relatively low conformational asymmetry, as well as for no conformational asymmetry (Appendix, Fig. A.3), differ from previous SCFT results obtained for AB_4 miktoarm polymers [36], which have exceptionally high conformational asymmetry. For example, the phase sequence for $\alpha = 1$ and $f_A = 0.2$ exhibits a transition from fcc to σ to C14, without a C15 regime. Similar results for $f_A = 0.28$ yield σ as the equilibrium phase for the neat melt, with a transition to C15, while $f_A = 0.32$ produces A15 in the neat melt and transitions to hex cylinders

with added homopolymer. If the homopolymer length increases further to a ratio of $\alpha = 1.25$, the AB_4 miktoarm system now exhibits a transition from A15 to σ to C15, followed by phase separation. The particular Frank-Kasper phases for the neat polymer melts that emerge in the AB_4 miktoarm system arise from the conformational asymmetry argument [31]. Nevertheless, even for this different system, Frank-Kasper phases of increasingly higher volume asymmetry are selected as the homopolymer volume fraction increases, consistent with our result.

Our analysis benefits from the ability of SCFT to readily distinguish between the homopolymer and minority-block within the particle cores, since these are distinct entities in the calculation [50]. An outstanding question related to the volume asymmetry mechanism is whether the selective partitioning of the homopolymers to the larger particles can be observed experimentally. There is a body of prior work on combining small-angle X-ray scattering (SAXS) and small-angle neutron scattering (SANS) to identify the locations of homopolymers in block polymer microstrutctures [112, 113], and microscopy has also been employed for this purpose [114]. The small domain sizes of the particles in these phases and the subtle (but important) differences in A-polymer volume fractions within different particles pose non-trivial experimental obstacles, but it may be possible to observe the partitioning effect through changes in the relative intensity of the scattering from the Z16 particles in C15 relative to the Z12 particles as the hompolymer volume fraction increases. Such an experimental confirmation would firmly establish volume asymmetry as one of the growing number of mechanisms [20, 31, 69] giving rise to Frank-Kasper phases in block polymers.

It remains to be seen whether this volume asymmetry mechanism holds for other soft matter, where forming a dry brush regime is no longer possible. For example, C14 and C15 Laves phases have been observed to emerge from a bcc phase in lyotropic liquid

crystals [101] by fixing the loading of oil within the micelle core and decreasing the head-group hydration number. The oils used in surfactant experiments are low molecular weight molecules, and might be assumed to form a wet brush with the hydrocarbon portion of the surfactant molecules. However, the qualitative rules associated with the transition from wet ($\alpha \approx 1/2$) to dry ($\alpha \approx 1$) brush behavior when homopolymer is mixed with block polymer do not translate directly to the case of surfactant and oil, which are characterized by the extreme limit of self-concentration [28]. Analogous experiments with a fixed hydration number but varying the oil loading would provide an ideal test for the generality of the volume asymmetry mechanism.

Chapter 4

The disordered micelle regime in conformationally asymmetric diblock copolymer melts

Diblock copolymers with a high degree of compositional asymmetry produce (approximately) spherical particles with the minority A-block partitioning to the core of the spheres, which pack onto a lattice at low temperatures with the majority B-block forming the matrix [93]. In addition to traditional sphere-forming phases such as body-centered cubic (BCC) or face-centered cubic (FCC), recent experimental work has revealed the existence of the tetrahedrally close-packed Frank-Kasper [12, 13] phases σ [14–18], A15 [15, 16, 19], C14 [17, 20, 21], and C15 [20, 21] for systems possessing high conformational asymmetry, the latter defined by the ratio $\epsilon = b_A/b_B$ of the statistical segment length of the two blocks. [31]. As the system is heated past its order-disorder transition temperature T_{ODT}, the lattice is destroyed by a first-order phase transition to produce a disordered micelle state. For a diblock copolymer of degree of polymerization

N, the value of the Flory-Huggins χ parameter corresponding to this transition is denoted χN_{ODT}. Upon further heating, the system eventually reaches its critical micelle temperature, where the micelles themselves disaggregate and produce a homogeneous solution. This second transition can be expressed in terms of the value of χN_{CMT} where, above the critical micelle temperature, the segregation strength is insufficient to drive the self-assembly of micelles [115, 116].

We are interested here in the structure of the disordered micelle state for cases where the system is above χN_{CMT}. Recent molecular dynamics simulations by Ghasimakbari and Morse [117] have successfully quantified the structure factor of this disordered state over a large range of compositions for compositionally asymmetric but conformationally symmetric diblock copolymers. Importantly, this work directly examined the parametric dependence of various quantities on the invariant polymerization index, $\bar{N}$. The quantity $\bar{N}$ plays an important role in quantifying the composition fluctuation effects observed in experiments associated with finite-length polymers [32]. In the limit of $\bar{N} \to \infty$, the structure of the disordered state corresponds to the result of random phase approximation (RPA). [92]

In this chapter, we probe the structure of the disordered micelle state for compositionally asymmetric diblock copolymer melts possessing both conformational asymmetry and a finite value of $\bar{N}$. Our study is motivated by a trio of possible connections between the the structure of the disordered state and the emergence of Frank-Kasper phases. First, both experimental and computational studies revealed that the Frank-Kasper σ phase emerges as the thermodynamically stable state by increasing ϵ [15, 17, 18, 31, 34]. Remarkably, at high ϵ, experiments revealed a direct transition between the disordered state and the A15 phase at high ϵ, which Bates et al. [15] attributed to the combined influences of conformational asymmetry and composition fluctuations. Second, recent experimental work has isolated $\bar{N}$ as a key factor in the formation Frank-Kasper phases

in compositionally asymmetric diblock copolymers [28]. Explicitly, Frank-Kasper phases were observed in experimental system with $\bar{N} \lesssim 400$ for conditions that do not correspond to a stable Frank-Kasper phase in mean-field methods such as Self-Consistent Field Theory (SCFT). Third, thermal processing has found remarkable success in coaxing the formation of Frank-Kasper phases in regions of phase diagram where they are unlikely to be the stable state [20, 22]. In one example, Kim et al. [20] rapidly cooled their diblock copolymer samples in liquid nitrogen and discovered the formation of C14 phase by annealing at temperatures where BCC is usually found. In a subsequent work, Kim et al. [21] postulated that long-lived non-equilibrium structures in the disordered liquid states of the micelles above the order-disorder temperature, T_{ODT}, are kinetically trapped by the rapid cooling procedure. These structures subsequently guide the formation of the observed metastable states, which remarkably persist over multiple cooling and heating cycles past T_{ODT}. This idea is attractive considering the observation of liquid-like packing (LLP) structures after rapid cooling, which potentially retains the favorable micelle size distribution for the reformation of the metastable state [20]. The formation of a dodecagonal quasicrystalline state (DDQC) following rapid cooling, which eventually reorders into the σ phase, might be a manifestation of the same phenomena [22]. Indeed, DDQC can be tiled with the same building blocks that tile the σ phase, analogous to the idea that capturing the structure of the disordered liquid states guides the formation of C14 and C15 [22].

In all of these cases, the emergence of Frank-Kasper phases could have intrinsic ties to structure present in the disordered micelle state, especially as the stability window of the disordered micelles widens significantly at low values of $\bar{N}$ [116]. One may argue that a wide window of stability could support longer lasting disordered structures, that are then able to transition into Frank-Kasper phases below T_{ODT}. [20, 21] To understand such phenomena, it is elucidating to examine the structure of the disordered micelles under

the influence of both composition fluctuations and conformational asymmetry. However, no study of the disordered phase exists that addresses the effects of conformational asymmetry in the compositional asymmetry limit for a low $\bar{N}$ diblock copolymer.

The Monte-Carlo Field Theoretic Simulation (MC-FTS) method discussed in Chapter 2 provides a useful framework to study these systems with both $\bar{N}$ and χN as parameters native to the simulation [83–87]. Unlike particle-based methods such as molecular dynamics simulations, the computational time of field-based methods such as MC-FTS decreases with increasing chain length [24], and recent advances have enabled simulations of chain lengths near experimentally relevant molecular weights [85]. We chose to use MC-FTS over complex Langevin simulations [90, 118], an alternative field-based method that incorporates fluctuations, because MC-FTS only requires a straightforward Metropolis Monte Carlo algorithm that we were able to implement as a wrapper around a modified version of our open-source GPU-accelerated implementation of SCFT [119].

4.1 Methods

The calculations done in this Chapter are based on the MC-FTS implementation discussed in Chapter 2. Specific to this work, our simulations are performed with a grid size of 16 x 16 x 16 and a simulation box size of $4^3 N^{3/2} b_B^3$, which provides sufficient resolution to the system while maintaining a reasonable computational time.

To analyze the effect of conformational asymmetry on a computational simulation of a low $\bar{N}$ system, we have performed a set of simulations from the homogeneous initial condition at conformational asymmetries $\epsilon = \{1.0, 3.0\}$ with multiple Flory-Huggins parameters, $\chi N = \{10, 20, 23, 24, 25, 26, 30\}$ at compositional asymmetry of $f_A = 0.2$ and $\bar{N} = 10^4$. The value of $\chi N_{\mathrm{ODT}}^{\mathrm{SCFT}}$ for each ϵ from SCFT calculations is tabulated in Table 4.1, which was determined by interpolating the value of χN where the free energy

ϵ	$\chi N_{\mathrm{ODT}}^{\mathrm{SCFT}}$	ordered phase
1.0	21.55	BCC
3.0	24.23	FCC

Table 4.1: Order-disorder transition segregation strength, $\chi N_{\mathrm{ODT}}^{\mathrm{SCFT}}$, and ordered phase obtained from SCFT calculations for different conformational asymmetries, $\epsilon = b_A/b_B$, at $f_A = 0.2$.

of the stable ordered phase is equal to the free energy of the disordered phase (Appendix Fig. B.1). The range of χN in our simulations are chosen to be centered around the predicted SCFT order-disorder transition (ODT). To make clear the differences between the ODT predicted by mean-field theory and the higher ODT emerging due to fluctuation effects, we will use the notation $\chi N_{\mathrm{ODT}}^{\mathrm{SCFT}}$ for the ODT segregation strength obtained from SCFT calculations and χN_{ODT} for the ODT segregation strength of a finite $\bar{N}$ system, wherein $\chi N_{\mathrm{ODT}} > \chi N_{\mathrm{ODT}}^{\mathrm{SCFT}}$.

4.2 Structure factor of the disordered phase

We first analyze the disordered micelle phase through the structure factor,

$$\frac{S(\mathbf{q})}{\rho_0 N} = \frac{n}{(V\chi N_{\mathrm{bare}})^2}\langle W_-(\mathbf{q})W_-(-\mathbf{q})\rangle - \frac{1}{2\chi N_{\mathrm{bare}}} \tag{4.1}$$

where the ensemble average $\langle W_-(\mathbf{q})W_-(-\mathbf{q})\rangle$ is obtained by sampling the composition field using the Monte Carlo algorithm described in Chapter 2 [84]. Since we anticipate that the disordered state is an isotropic liquid, the average structure factor, $S(q)$, is obtained by further averaging $S(\mathbf{q})$ for each wavevector of the same magnitude in wavenumber. The simulated structure factor is directly related to the intensity profile resulting from small angle X-ray scattering experiments [11].

Figure 4.1 shows the normalized structure factor, $S(q)/\rho_0 N$, obtained for the case of $\chi N = \{10, 20, 23\}, \epsilon = 1.0, 3.0$ started from the homogeneous initial condition as a

function of the dimensionless wavenumber, qRg. The solid lines are fits to a modified parametric equation used previously [117] to fit structure functions obtained from molecular dynamics data,

$$S^{-1}(qR_g) = S^{-1}_{\mathrm{RPA}}(qR_g, \chi N, \epsilon) + a + b(qR_g)^2 + c(qR_g)^4 \tag{4.2}$$

where a, b, and c are fitting parameters. The best fit parameters are tabulated in Appendix Table B.1.

In the limit of low wavenumber, $qR_g \lesssim 1.5$, we observe in Fig. 4.1 that the curves collapse for all values of ϵ, indicating that conformational asymmetry has no impact on the long-range correlations of the disordered melt, i.e., for distances larger than that between multiple micelles. At intermediate wavenumbers, where intermicelle and intramicelle correlations become important, the structure factors for different values of ϵ start to diverge before converging again at the very high wavenumbers, where intramicelle correlations dominate. As the value of χN increases from 10 to 23, we observe that the magnitude of the peaks similarly increases. This is consistent with the understanding that correlations within the melt increase with segregation strength until the order-disorder transition leads to the formation of Bragg peaks past χN_{ODT} [11]. Consistent across all values of χN, the peak height for $\epsilon = 3$ is lower than those from $\epsilon = 1$ and the peak location for $\epsilon = 3$ is at a lower value of qR_g compared to those from $\epsilon = 1$.

We have limited the data for Fig. 4.1 to values of $\chi N \leq 23$ where the fitting of Eq. 4.1 makes sense. At higher values of χN, the system produces strongly ordered structure with a high intensity primary peak and a secondary peak that could no longer be fitted by the modified RPA equation. For example, Fig. 4.2 shows the transition of structure factor going from $\chi N = 23$ to $\chi N = 26$ which produces a high intensity

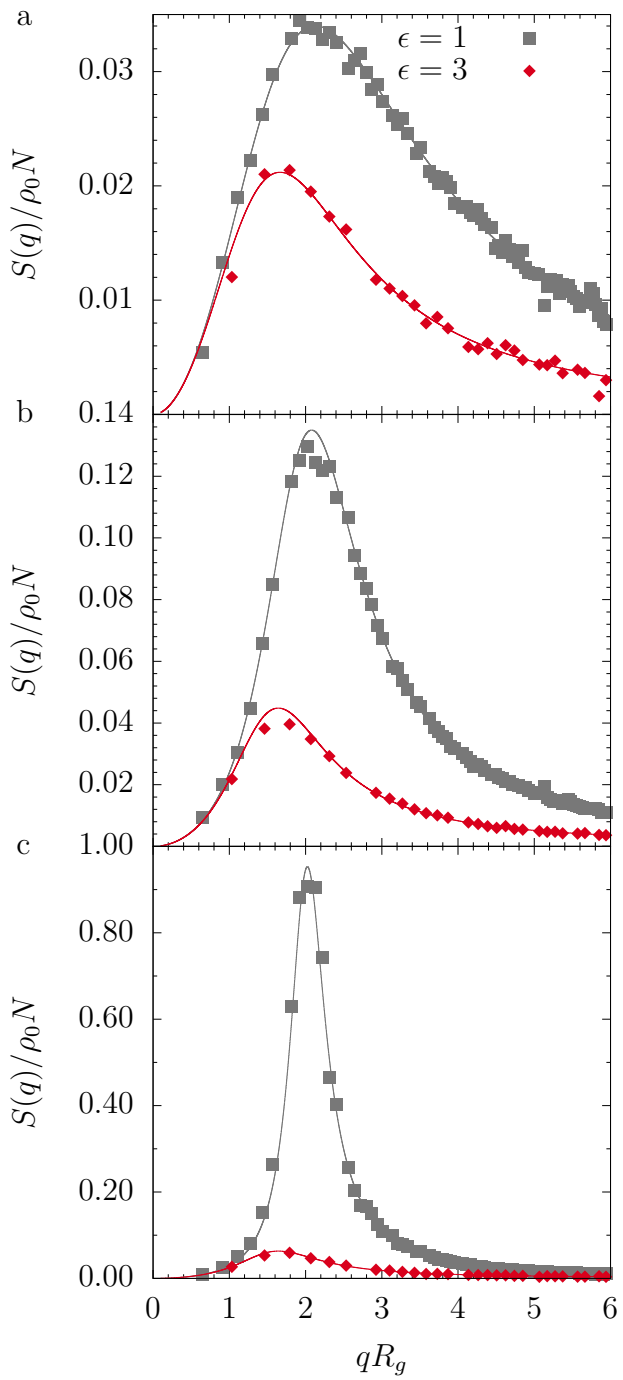

Figure 4.1: Structure factor for (a) $\chi N = 10$, (b) $\chi N = 20$ and (c) $\chi N = 23$ for $\epsilon = 1.0$ (gray ■), and $\epsilon = 3.0$ (red ♦) versus qR_g. The solid lines are fits of Eq. 4.2 to the discrete data points.

primary peak and a secondary shoulder. In this section, we are primarily interested in the behavior in the disordered regime and further analysis for the rest of our dataset would be done in subsequent sections.

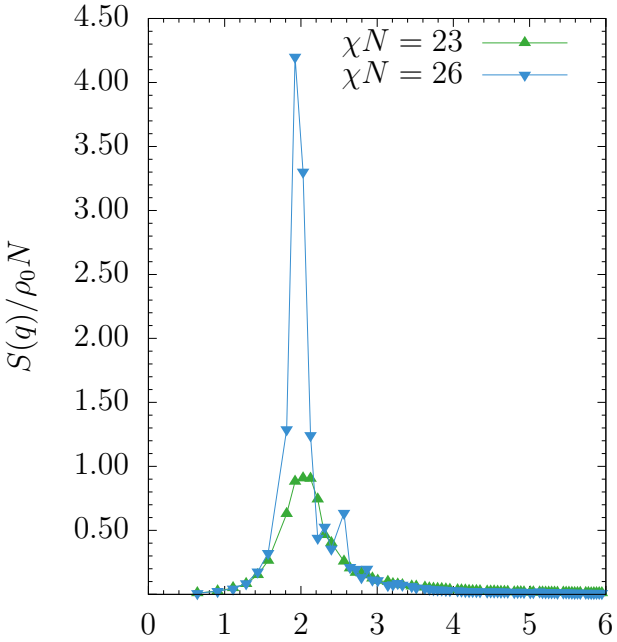

Figure 4.2: Structure factor for $\epsilon = 1.0$ at $\chi N = 23$ (green ▲) and $\chi N = 26$ (light blue ▼). The solid lines are guide to the eye.

As a check on our calculation of the structure factor, we compared the results at $\epsilon = 1$ with those from the RPA theory. Previous work by Wang et al. [116] demonstrated that the structure factor from a simulation with disordered micelles produces a larger structure factor peak intensity compared to RPA in conjunction with a left shift of the peak location to smaller qR_g values as compared to the RPA values. Our analysis in Fig. 4.3 is consistent with their observation. The deviation of peak intensity increases as we increase the segregation strength away from the athermal case. The rationale for this behavior is that the formation of disordered micelles accentuates the intensity of the disordered structure compared to the randomly mixed model underlying RPA. For

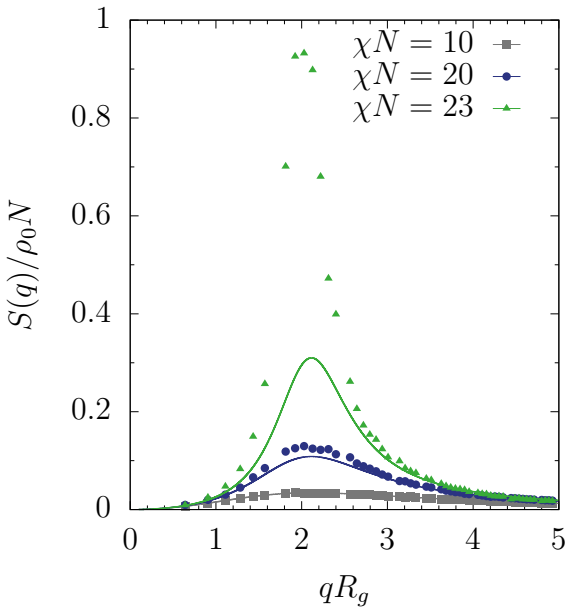

Figure 4.3: Structure factor versus dimensionless wavevector at $\epsilon = 1$. The solid points are results from our MC-FTS simulation while the solid lines are the structure factors obtained from the RPA equation. The fitting to MC-FTS data to Eq. 4.2 is removed for clarity.

the case of $\chi N = 10$, the segregation strength is sufficiently weak to reduce back to the randomly mixed model. We also observe a left shift of the peak location in our MC-FTS simulation compared to the result from RPA. This is most noticeable in the case of $\chi N = 23$, which again, indicates the formation of disordered micelles. We repeated this analysis for $\epsilon = 3$ in Fig. 4.4. For $\epsilon = 3$, the structure factor at $\chi N = 10$ again reduces back to the randomly mixed model. However, the magnitude of structure factor at $\chi N = 23$ is only marginally stronger than the structure factor from RPA. The result at $\epsilon = 3$ indicates that the window of stability for the formation of disordered micelle regime is smaller, or perhaps nonexistant, compared to those at $\epsilon = 1$.

To better visualize the change in peak height for different values of χN and ϵ, Fig. 4.5 plots the scattering peak, $S(q^\star)$ normalized by the peak from RPA, $S_{\mathrm{RPA}}(q^\star)$, as a

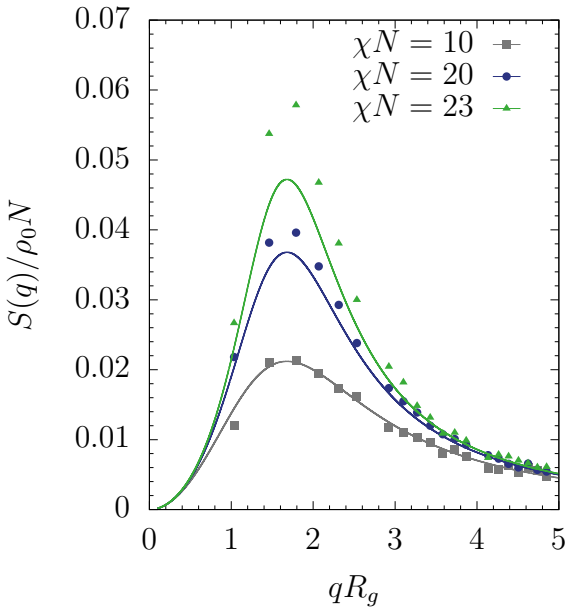

Figure 4.4: Structure factor versus dimensionless wavevector at $\epsilon = 3$. The solid points are results from our MC-FTS simulation while the solid lines are the structure factors obtained from the RPA equation. The fitting to MC-FTS data to Eq. 4.2 is removed for clarity.

function of segregation strength, χN. This presentation much more clearly illustrates the increasing deviation in peak height as we increase χN. For the case of $\epsilon = 1$, we observe a sudden jump in deviation in peak height at $\chi N = 23$. Meanwhile, we only observe a linear increase in deviation for the case of $\epsilon = 3$. We posit that the sudden jump in deviation at $\chi N = 23$ and $\epsilon = 1$ is an indicator for the formation of disordered micelles phase. We do not observe a similar spike at $\epsilon = 3$, possibly due to the formation of the disordered micelles occuring at a higher value of χN, proportional to the increase in χN_{ODT} at higher ϵ.

As a final validation of our result, we consider the location of the peak of the structure factor, $q^\star$ to those from RPA, q_0 in Fig. 4.6. The RPA prediction for the peak

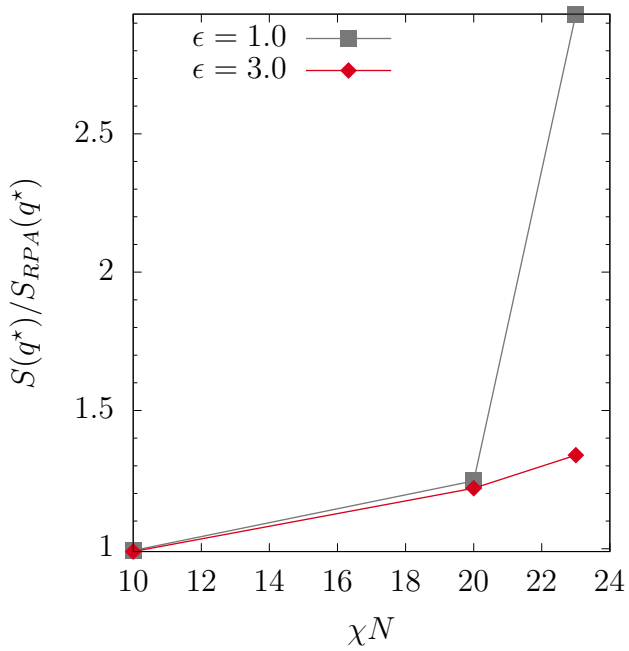

Figure 4.5: Ratio of scattering peak of MC-FTS to RPA, $S(q^\star)/S_{\mathrm{RPA}}(q^\star)$ versus Flory-Huggins parameter for $\epsilon = 1.0$ (gray ■), and $\epsilon = 3.0$ (red ♦). The solid lines are guide to the eye.

wavenumber is invariant to the value of χN but is different for each value of ϵ. Subsequent works [115–117] have shown that $q^\star$ decreases with increasing χN as composition fluctuations become increasingly important. Our calculations show a monotonic decrease in $q^\star/q_0$ with increasing χN for the case of $\epsilon = 1$ which agrees with the previous studies. For the case of $\epsilon = 3$, the peak location appears to have a decreasing behavior up until $\chi N = 23$. This inconsistency could be due to the error introduced by the continuous fit of Eq. 4.2 to the discrete data points from the simulations from which the location of the peak wavenumber is determined. While the fitting equation works well in describing the overall shape of the structure factor, the use of the fitting equation in practice appears to have quite a significant degree of uncertainty due to the disproportionate lower number of points in the low qR_g region where the peaks for the case of

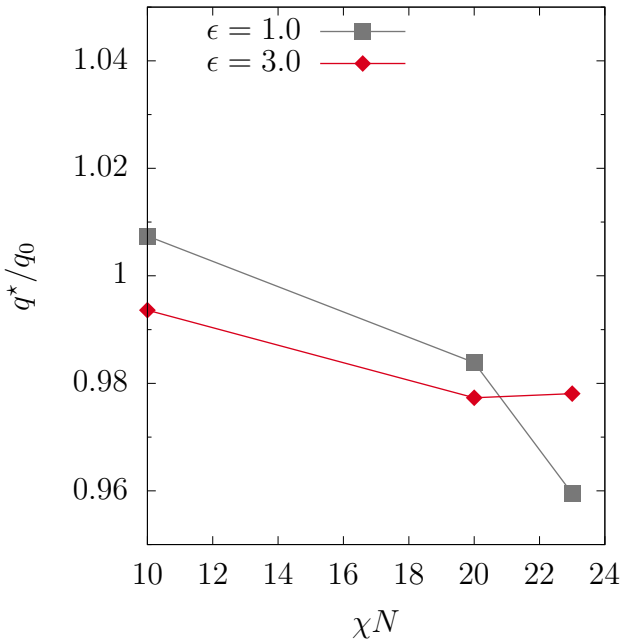

Figure 4.6: Ratio of peak location of MC-FTS to RPA, $q^\star/q_0$ versus Flory-Huggins parameter for $\epsilon = 1.0$ (gray ■), and $\epsilon = 3.0$ (red ♦). The solid lines are guide to the eye.

$\epsilon = 3$ are located. Indeed, our attempts to fit the structure factor for the entire range of qR_g with Eq. 4.2 sometimes misses the peak completely (Appendix Fig. B.2). As a result, we usually cut off the data used in the fit at about $qR_g \approx 4$ (Appendix Table B.2). The resolution of $q^\star$ can be improved, in principle, by repeating the calculation with a finer simulation mesh at the cost of more computational time to balance the number of points in the low qR_g region to better fit the location of the peaks.

4.3 χN_{ODT} of conformational asymmetric diblock copolymer

Our examination of the structure factor for values of χN below the ODT have unveiled an interesting phenomena whereby we do not detect the formation of the disordered micelle regime for $\epsilon = 3$, but there do appear to be micelles forming at $\epsilon = 1$. To obtain a deeper understanding on this phenomena, we performed a hysteresis loop analysis to estimate the χN_{ODT} for both values of ϵ. For such analysis, we analyzed data from our MC-FTS calculations at values of χN beyond those whose structure factor can be reasonably fitted by Eq. 4.2. Next, we performed another set of calculations started from the ordered state to produce the melting branch of the hysteresis diagram. The dataset analyzed in the previous section, which was obtained with the homogeneous initial condition, is thus the cooling branch of the hysteresis diagram. In principle, the combination of the melting and cooling branch would then form a hysteresis loop whereby the ODT of the system is bracketed by the loop.

ϵ	$L_{SCFT,\,\chi N\,=\,25}$
1.0	1.86
3.0	3.61

Table 4.2: Optimized unit cell size for a BCC structure from SCFT calculation for $\epsilon = 1, 3$ and $\chi N = 25$.

We initialized the calculations started from the ordered state with n copies of the BCC structure that best minimize the commensurability between the unit cell size of our calculation to those from SCFT. The optimized unit cell size for a BCC structure from SCFT at $\chi N = 25$ is shown in Table. 4.2. The calculations at $\epsilon = 1$ are initialized with a 2 x 2 x 2 BCC structure, while the calculations at $\epsilon = 3$ are initialized with only a single BCC structure. We chose to use the optimized SCFT unit cell size at $\chi N = 25$ as it is the midpoint for the range of χN used in this work, which is also above the

χN_{ODT} for both values of ϵ.

We use the order parameter,

$$\Psi = \frac{1}{V^2}\langle W_-(q^*)W_-(-q^*)\rangle \tag{4.3}$$

as introduced by Stasiak and Matsen [84] which is essentially the normalized peak of the structure factor, where Ψ approaches 0 in the limit of a disordered $\bar{N} \to \infty$ system but approaches a large finite value for ordered structures. Hysteresis diagrams using the order parameter for $\epsilon = 1, 3$ are plotted in Fig. 4.7.

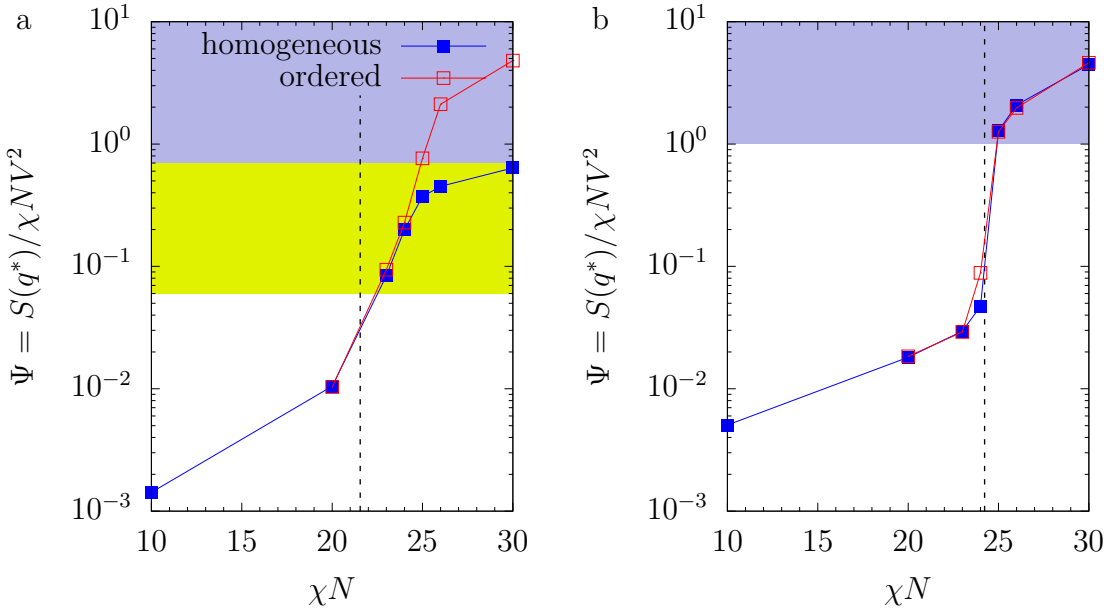

Figure 4.7: Order parameter, Ψ, versus χN for (a) $\epsilon = 1$ (b) $\epsilon = 3$. The solid symbol corresponds to the cooling branch where the initial condition is a homogeneous structure while the open symbol corresponds to the melting branch where the initial condition is an ordered structure. The broken vertical line indicates $\chi N_{\mathrm{ODT}}^{\mathrm{SCFT}}$. The region where we observe the formation of the disordered micelle regime is labeled in yellow whereas the region for the formation of ordered structure is labeled in blue.

We first begin with the case of $\epsilon = 1$ in Fig. 4.7a. In the cooling branch, we observe low values of the order parameter at low χN consistent with the formation of the

disordered melt. Upon increasing χN to about $\chi N = 23$, the order parameter increases by about 2 orders of magnitude to about $\Psi \sim 10^{-1}$. We have labeled this region yellow to represent the formation of disordered micelles as indicated by the strong deviation of structure factor from RPA. For $\chi N > 25$, we observe a very strong, but broad, primary peak in the structure factor which may indicate that the system is in the ordered regime but trapped in a metastable state. Indeed, the order parameter did not increase past $\Psi = 1$ for $\chi N > 25$. A visual inspection of the real space density profile for $\chi N > 23$ shows the formation of disordered micelles but a lack of long range ordering even for the very highest $\chi N = 30$ (Appendix Fig. B.3). However, the melting branch retains its ordered structure at $\chi N > 25$ which rapidly merges with the cooling branch below $\chi N = 23$. At $\chi N > 25$, the structure factor forms Bragg peaks with peak spacings corresponding to the BCC structure ($q/q^* = \sqrt{1}, \sqrt{2}, \sqrt{3}$) (Appendix Fig. B.4a).

Meanwhile, Fig. 4.7b shows the hysteresis loop for the case of $\epsilon = 3$. In the cooling branch of $\epsilon = 3$, the system once again begins at low values of the order parameter before rapidly increasing by almost two orders of magnitude at $\chi N = 25$. In the melting branch, the order parameter matches those of the cooling branch except near $\chi N = 24$, forming a small hysteresis loop. Despite both branches matching at high χN, the structure factors from the cooling branch do not form Bragg peaks that exactly correspond to the BCC structure (Appendix Fig. B.6a). A visual inspection of the density field shows a skewed BCC-like structure (Appendix Fig. B.6b). We do not observe any formation of the disordered micelle regime in the cooling branch.

Interestingly, the hysteresis loop for $\epsilon = 3$ did not have any issue with convergence as opposed to the case of $\epsilon = 1$. We believe the reason for this is two-fold. First, the cooling branch of $\epsilon = 1$ requires the ordering of 8 copies of the BCC structure as opposed to one copy for of $\epsilon = 3$. With the increase in the number of micelles in the simulation volume, the possibility for the formation of defects increases the same,

leading to a slow evolution time in the simulation. In conjuction, we suspect that our Monte Carlo moves might not be efficient to escape the metastable disordered micelle regime at very high values of χN. This is indicated by the wavevectors, $\mathbf{q}$, corresponding to the same wavenumber, q, resolve to different structure factors when the calculations were started from the homogeneous initial condition and, subsequently, were trapped in a defective state (Appendix Fig. B.7). Indeed, recent Langevin dynamics Field Theoretic Simulations to determine χN_{ODT} for ranges of f_A higher than those done here encounter the same issues despite being more efficient [87,120]. Nevertheless, Beardsley and Matsen argue that the lower bound for the ODT from the melting branch is a good estimate for χN_{ODT} since the ease of forming defects prevents the existence of ordered structure below χN_{ODT} [120].

Using only the melting branch to estimate χN_{ODT}, we obtained χN_{ODT} of about 25 for both values of ϵ. For the case of $\epsilon = 1$, the shift in ODT from our MC-FTS calculations is 3.45, which is similar to the result from molecular dynamics calculation of 3.04 at $f_A = 0.25$ extrapolated to $\bar{N} = 10^4$ [121]. To ensure that our result is insensitive to finite size effects at $\epsilon = 3$, we doubled the BCC structure in each direction at $\chi N = 26$ and repeated the calculation at $\chi N = 25, 26, 30$ with a unit cell size of $V = 7.22^3 N^{3/2} b_B^3$ for another 2×10^6 steps. We observed that the ordered structure does not melt at for both cases, indicating that our calculated ODT does not change with the box size.

4.4 Real-Space Analysis of the Micelle Size

MC-FTS simulations generate samples of composition field, $W_-(\mathbf{r})$, a self-consistent pressure field, $w_+(\mathbf{r})$, and density field of each monomer, $\phi_\alpha(\mathbf{r})$. We have previously used the composition field to determine the structure factor. We now turn to the corresponding density field to estimate the size of the micelles from the real-space data.

We analyzed the density field samples from the MC-FTS simulation using a simple breadth-first search algorithm to determine the locations of micelles. The algorithm first picks an initial position $\mathbf{r}_0$ in the unit cell that satisfies

$$\phi_A(\mathbf{r} = \mathbf{r}_0) > I \tag{4.4}$$

where I is an isovalue selected to represent a concentration fluctuation above the background. We chose an isovalue of, I = 0.60, which is sufficiently high such that the minority block is the majority component at that location. The algorithm then iteratively marks adjacent grid points as part of the same micelle if they fulfill the condition in Eq. 4.4. The algorithm ends when every grid point is visited and, if Eq. 4.4 is fulfilled, clustered as part of their respective micelles. The volume of the micelles is determined by multiplying the number of grid points with the volume occupied by the cube surrounding a grid point. The micelle size, R_m, is then obtained by taking the cube root of the volume of the micelles.

To provide some intuition for the real space analysis, the micelle distributions for three different values of χN at $\epsilon = 1$ with the homogeneous initial condition are shown in the histograms of Fig. 4.8. For the case of $\chi N = 20$, where the system had yet to form disordered micelles, the histogram is heavily right-skewed such that the majority of the fluctuations results in the formation of micelles of one grid point, i.e. a local fluctuation that exceeds the isovalue but does not form a cluster of such points. In the intermediate case of $\chi N = 23$, where we believe we are observing the formation of disordered micelles, the micelle distribution is still mostly right-skewed with a large amount of one grid point sized micelle, but also contains an additional peak centered at a size larger than one grid point. In the case of $\chi N = 26$, the distribution of micelle sizes adopt a Gaussian-like curve centered at a larger than one pixel sized micelle size.

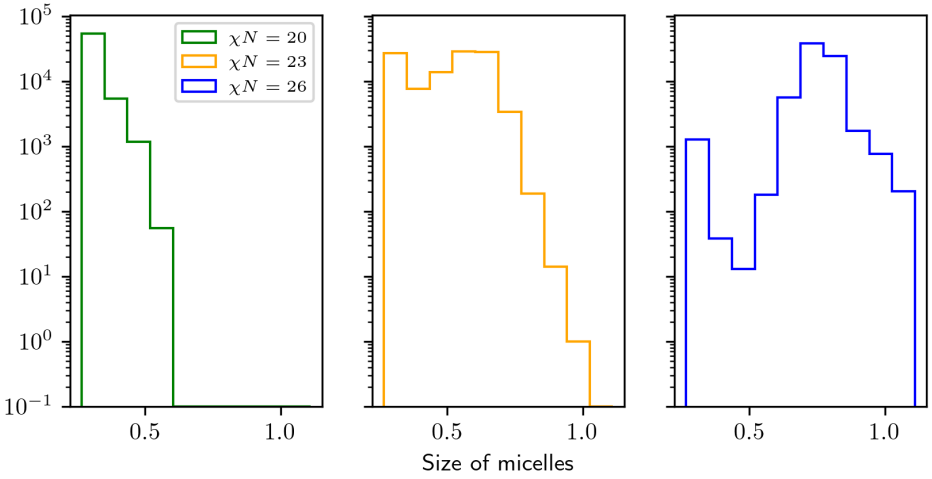

Figure 4.8: Histogram of the micelle size over all Monte Carlo samples for $\epsilon = 1$ and $\chi N = 20, 23, 26$ started from the homogeneous initial condition.

We next examine the effect of changing χN on both the mean size of the micelle and the number of clusters for both values of ϵ. Figure 4.9a shows the analysis for the micelle size at $\epsilon = 1$. At $\chi N = 10$, our choice of isovalue results in no detectable micelles for both values of ϵ. This indicates that we have made a good selection for the isovalue where it is large enough to filter out all the random fluctuations that may be present but are not strong enough to form disordered micelles. For the case of $\chi N = 10$ which reproduces the RPA result almost exactly, we expect that there should be no well-formed micelles. As seen in Fig. 4.9a, increasing χN results in larger micelles on average. As χN increases, the fluctuations strength grows stronger and forms increasingly larger micelles. We see similar results in the size of the micelle for both initial conditions up until $\chi N = 24$, where the results deviate from one another. This is consistent with the hysteresis diagram of Fig. 4.7a where the bifurcation is observed at nearly the same χN. In general, micelle size at high χN for the calculations started from the homogeneous initial condition are smaller than those started from the ordered initial condition. At

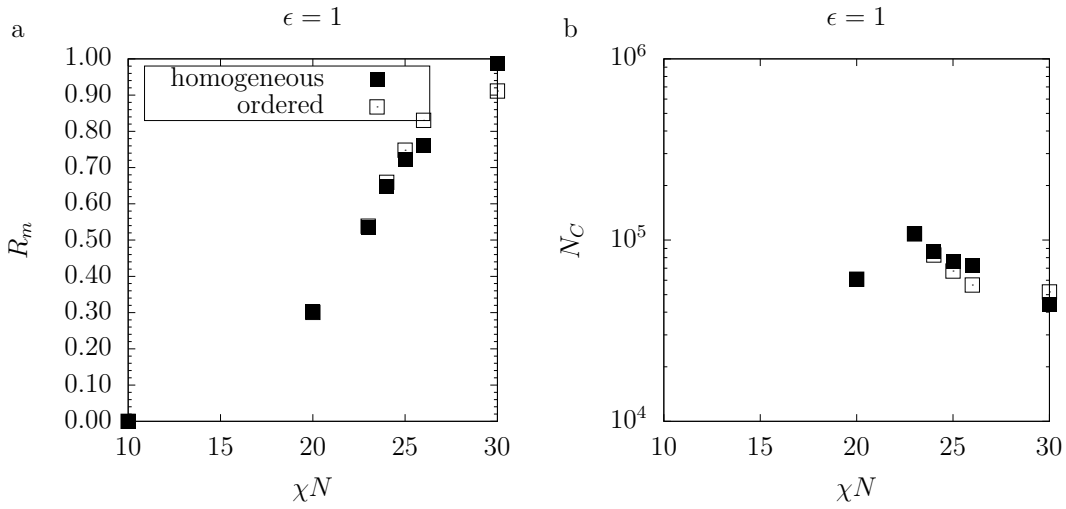

Figure 4.9: Plot of (a) the mean size of micelles, and (b) number of clusters over all χN values at $\epsilon = 1$ started from the homogeneous initial condition(solid squares) and from the ordered initial condition (empty squares).

$\chi N = 30$, we observe elongation of the micelles similar to those of hexagonal cylinders for those of homogeneous initial condition. This is reflected in the larger micelle size compared to the micelle size with ordered initial condition.

Meanwhile, Fig. 4.9b shows the number of micelles for $\epsilon = 1$ increasing to a maximum at $\chi N = 23$ for both initial conditions. Interestingly, this point coincides with the start of the window of existence for the disordered micelle regime established in Fig. 4.7a. Similar to Fig. 4.9a, the number of micelles from both initial conditions deviate at about $\chi N = 24$, with both following a monotonically decreasing trend with increasing χN starting from the peak at $\chi N = 23$. At $\chi N > 23$, the number of micelles from the homogeneous initial condition are, in general, larger than those from the ordered initial condition. At $\chi N = 30$, the elongation of the micelles in the homogeneous initial condition results in a much lower number of micelles compared to those of the ordered initial condition, which remains a BCC structure.

Next, we examine Fig. 4.10a which shows the analysis for the micelle size at $\epsilon = 3$.

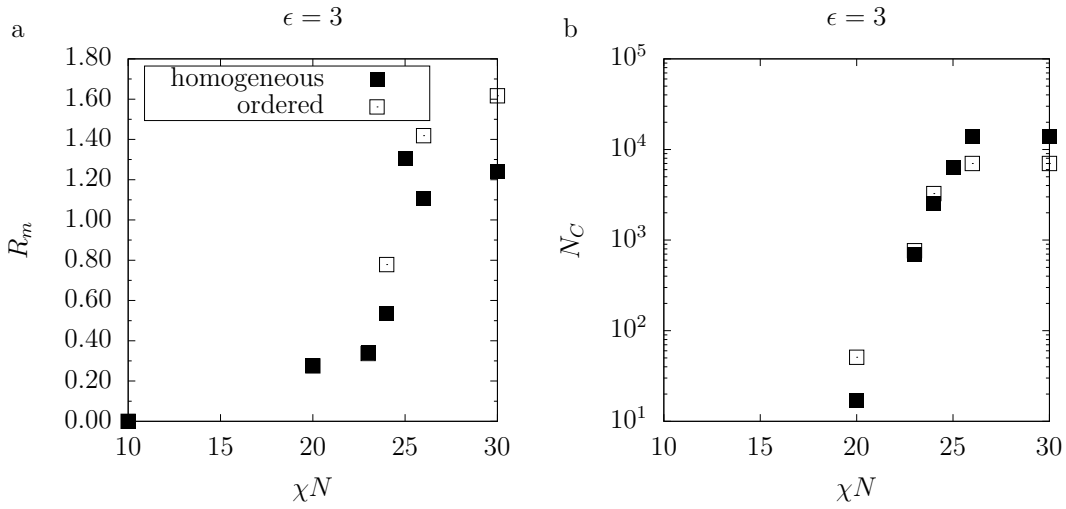

Figure 4.10: Plot of (a) the mean size of micelles, and (b) number of clusters over all χN values at $\epsilon = 3$ started from the homogeneous initial condition(solid squares) and from the ordered initial condition (empty squares).

In this case, we once again observe similar trends in the mean micelle size for both initial conditions, which again deviates at $\chi N = 24$ consistent with Fig. 4.7b. While we could close the hysteresis loop in Fig. 4.7b, Fig. 4.10a clearly shows a large divergence in the micelle size for the two initial condition at $\chi N > 26$. This agrees with our previous observation that the cooling branch resulted in ordered-like structures that do not fit the BCC lattice exactly. As shown in Fig. 4.10b, the number of clusters at $\epsilon = 3$ for both initial conditions track each other pretty well. The biggest difference for both initial conditions is found at $\chi N > 26$ where the homogeneous initial condition resulted in more micelles that those needed for the formation of a BCC lattice.

As we do not observe the formation of a peak in the number of clusters before the formation of ordered structures in Fig. 4.10b, we are confident that the peak observed in Fig. 4.9b indicates the transition into the disordered micelle regime. Indeed, our result of Fig. 4.10b is consistent with our analysis in Fig. 4.7b where we do not observe any disordered micelle regime. The sudden increase in the number of micelles at the

onset of the disordered micelle regime has interesting repercussions. While MC-FTS is strictly an equilibrium method, we can speculate on the dynamics of the formation of ordered structure from the disordered state based on the previous results. Particularly, there needs to be some mechanism whereby the number of micelle reduces from the maximum in the disordered micelle regime to those needed for the formation of an ordered structure. Previously discussed thermal processing experiments have postulated one such mechanism to be the fussion and fission of micelles [21]. Our results which show the formation of a large number of small micelles in the disordered micelle regime is consistent with the idea of fussion and fission.

4.5 Discussion

Our analysis indicates that increasing χN at fixed ϵ from the disordered melt leads to (i) an increase in the peak of the structure factor, $S(q^\star)$; (ii) a shift of the peak to lower wavenumber, $q^\star$. For $\epsilon = 1$, past $\chi N_{\mathrm{ODT}}^{\mathrm{SCFT}}$ we observe the formation of the disordered micelle regime as indicated by (i) a large deviation of the peak of the structure factor compared to the RPA prediction; (ii) a sharp peak in the number of clusters through real-space analysis of the density field. Interestingly, the combination of both of our analyses unveiled a seemingly smaller or nonexistent window of stability for the disordered micelle regime at the higher values of ϵ. Upon noting the lack of the formation of the disordered micelle regime in $\epsilon = 3$, we are led to conclude that the window of existence for disordered micelle regime is bracketed by $\chi N_{\mathrm{ODT}}^{\mathrm{SCFT}}$ and the larger χN_{ODT} of the system. Due to the close proximity of $\chi N_{\mathrm{ODT}}^{\mathrm{SCFT}}$ and χN_{ODT} for $\epsilon = 3$, we do not observe the formation of the disordered micelle regime. A particularly satisfying aspect of our analysis is the synergy between reciprocal-space and real-space analysis, which allowed deeper insights into the structure of the disordered micelle state than is possible through one method alone.

While the utility of this methodology is apparent, a possible systematic error in our analysis is the uncertainty in how the unit cell size affects the results. In both particle-based and field-based methods, the choice of unit size is especially important in determining the selection of the ordered state above χN_{ODT} [85, 121]. For the compositional symmetric diblock copolymer case, Vorselaars et al. [85] have attempted to relieve the stress on the unit cell by performing a volume-preserving, box-altering Monte Carlo move in their study of the lamellar phase. Recent work by Beardsley and Matsen attempts to solve this problem by brute force, simulating different unit cell sizes and picking the one that maximizes the intensity in structure factor [120]. Their results show that the optimal unit cell sizes are near their respective SCFT box sizes, which coincide with our method for selecting simulation box sizes. Nevertheless, there has yet to be a comprehensive analysis on the effect incommensurate unit cell sizes, which may be important in our work as our simulation volume is about 7-10% larger than the SCFT box size. Future studies that attempt this brute force method could alleviate the computational time requirement by using Langevin sampling in MC-FTS [87] that has shown to improve computation time by an order of magnitude.

In principle, one can choose to perform either molecular dynamics calculations or a complex Langevin calculation to perform the same analyses of the disordered micelle phase as those done here. Molecular dynamics calculations would have a higher resolution in their structure factor result compared to the pseudospectral solution in MC-FTS, which limits the resolution of the system to the grid points in the simulations. However, molecular dynamics calculations are computationally expensive to equilibrate at our value of $\bar{N}$. Complex Langevin calculations seem to be an attractive option, having seen success in analyzing fluctuation effects on the stability of different phases [15, 90]. Different from MC-FTS, complex Langevin calculations deal with the issue of UV divergence by adopting a weakly compressible model of the polymer [90]. The model will

require tuning of the parameter controlling the compressibility of the system and it is unknown how it changes the resulting disordered micelle phase, as most work has been focused on ordered phases. In either case, it is unclear at the moment what is the efficacy of other types of analysis of the disordered micelle phase compared to MC-FTS. A head-to-head comparison of the computational time of these different methods is needed to make an informed selection of methodology.

4.6 Conclusion

This work investigated the effects of conformational asymmetry in compositionally asymmetric diblock copolymers using MC-FTS calculations to access the disordered micelle state. We have analyzed the resulting disordered micelle phase using two methods, a structure factor analysis and a real-space clustering method. The results reveal key features for the formation of the disordered micelle regime, which can largely be associated with gap the between $\chi N_{\mathrm{ODT}}^{\mathrm{SCFT}}$ and χN_{ODT}. The real space analysis also enabled us to postulate that fussion of micelles is required in the direct transition of the disordered micelle regime into an ordered sphere forming structures. Our analysis shows a surpression in the formation of the disordered micelle phase for higher conformational asymmetry. This work represents a key step in further developing the understanding of the behavior of the disordered micelle phase. In the case where the long-lived structures in the disordered micellar states are highly correlated with the formation of different Frank-Kasper phases, [20, 21] a comprehensive understanding of the behavior of the disordered micelle phase should provide a deep understanding of how transitions across the order-disorder transition impact the selection of complex sphere-forming phases.

Chapter 5

Frank-Kasper phases in binary diblock copolymer blends

5.1 Introduction

Our work in Chapter 3 with diblock copolymer/homopolymer blends has revealed a new mechanism in stabilizing various Frank-Kasper phases. In this chapter, we revisit the binary diblock copolymer blends briefly mentioned in Chapter 3 and futher explore its utility in stabilizing Frank-Kapser phases. SCFT calculation have shown that binary blends of A_1B/A_2B, where both chains have the same corona block length, N_B, but different core block length, N_{A_1,A_2}, stabilize the σ, A15, C14 and C15 phases [21,70]. Liu et al. attributed the stabilization of the complex Frank-Kasper phases to the anisotropic distribution of the binary blend in the micelle whereby the shorter chain favors regions of high curvature while the longer chain favors regions of lower curvature [70]. The redistribution of the two types of chains presumably eases the formation of the different micelle sizes associated with the Frank-Kasper phases. Experimental studies of this particular system have shown the formation of the σ phase for very short chains [18]

and the formation of σ and $A15$ phases for longer chains [106].

Here, we focus on the work done by Lindsay et al. [106] whose phase diagram should be predicted computationally owing to its high molecular weight. Recent work found a crossover invariant polymerization index of $\bar{N} \sim 400$ below which SCFT no longer predicts the phase stability of the system [28]. As such, the experimental work done by Lindsay et al. at $\bar{N} \gtrsim 1000$ could, in principle, be predicted through SCFT calculations owing to the longer chain lengths. We do expect some differences with the experimental results owing to fluctuation effects that are completely suppressed in SCFT [32]. Nevertheless, this lies in contrast to thermal processing techniques which can also be used to observe Frank-Kasper phases [20, 22]. Thermal processing techniques presumably only trap a metastable Frank-Kasper phase such that they can no longer be predicted by an equilibrium method such as SCFT. Meanwhile, one can also make use of conformational asymmetry to stabilize Frank-Kasper phases. Both experimental and computational work have shown that increasing conformational asymmetry results in the stabilization of complex phases [15, 17, 18, 31, 34]. From a practical standpoint, one will have to synthesize many different types of diblock copolymer with varying chemistries to sweep through a broad range of conformational asymmetry [18]. For A_1B/A_2B binary blends, one can easily access a large parameter ranges by changing the values of N_{A_1} and N_{A_2} by performing the same polymerization reaction with different amount of reactants, eschewing the need to deal with different chemistries [122]. Together, binary blends provide significant advantages over the other two mechanisms in stabilizing these Frank-Kasper phases.

Our objective here is twofold. First, we demonstrate the predictive ability of SCFT on high $\bar{N}$ binary blends. We chose a binary blend system similar to those of Ref. 106 but with different chain lengths. We then compare the computational phase diagram to its corresponding experimental version. Second, we reexamine the partitioning of the two

different chains over the simulation volume using the tools developed in Chapter 3 for our particle-by-particle analysis. Beyond the anisotropic distribution of the two types of chains in the micelles by Liu et al. [70], we are interested to see if there are other mechanisms or behaviors present in binary blend systems which could be responsible in stabilizing Frank-Kasper phases.

5.2 Methods

To verify the predictive ability of SCFT on high $\bar{N}$ binary diblock copolymer blends, we performed SCFT calculations for the A_1B/A_2B systems similar to those of Lindsay et al. [106] but with a shorter N_{A_2}. Mimicking the experimental conditions, we performed canonical ensemble SCFT calculations for $N_2/N_1 \sim 1.41$, $N_{B_1} = N_{B_2}$, $f_{A_1} = 0.12$, $f_{A_2} = 0.38$, and conformation asymmetry $\epsilon = b_A/b_B = 1.309$. We swept through a range of segregation strength $\chi N = 30 - 40$ and volume fraction of the short chain, $\phi_1 = 0 - 1$. The calculations were performed to reach a convergence criteria of 10^{-5} as defined in Ref. 74 with a contour length step size of $\Delta s = 0.01$. We considered the stability of A15, BCC, FCC, C14, C15, σ, Hexagonal cylinders (HEX), Gyroid (GYR), LAM, and the spherical Hexagonal Closed Packed structure (HCP). Grid size of $64 \times 64 \times 64$ was used for BCC, FCC, HCP, and GYR; 64×64 for the 2D HEX phase; and, 64 for the 1D LAM phase. Complex phases with many more particles were calculated with a fine resolution of $96 \times 96 \times 96$ for A15 and C15, $64 \times 64 \times 104$ for C14, and $128 \times 128 \times 64$ for σ.

5.3 Results

The phase diagram from our canonical ensemble SCFT calculations and the experimental phase diagram are shown in Fig. 5.1. As seen in Fig. 5.1a), the SCFT phase diagram

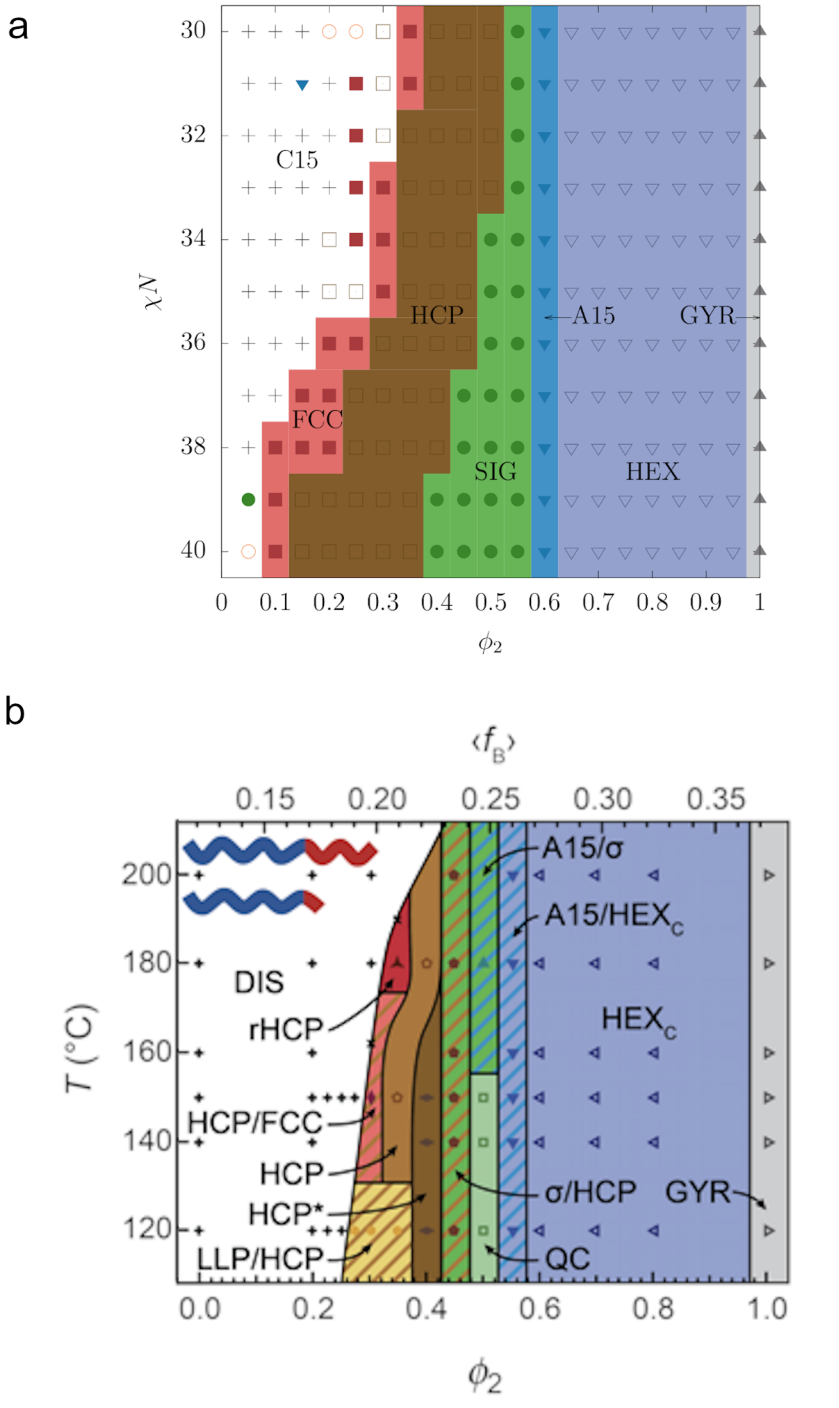

Figure 5.1: a) Binary blend phase diagram generated from canonical ensemble SCFT calculations. Symbols correspond to GYR (gray ▲), Hex (grayish blue ▽), A15 (blue ▼), σ (green ●) HCP (brown □), FCC(red ■), C14 (orange ○) and C15 (black +). b) Experimental phase diagram courtesy of Aaron Lindsay.

successfully reproduces the salient behaviors seen in experiments. Starting from $\phi_2 = 1$ ($\phi_1 = 0$), which is equivalent to a pure melt of the long chains ($f_A = 0.39$), we observe the stable Gyroid phase. Upon decreasing ϕ_2, we see the GYR $\rightarrow$ HEX $\rightarrow$ A15 $\rightarrow \sigma$ $\rightarrow$ HCP $\rightarrow$ FCC transition. This sequence of transition is similarly observed in the experimental phase diagram at about $T = 135°$C - 170°C. The main differences are the many two-phase windows of stability seen in the experimental phase diagram, which is a natural consequence of a binary blend system. For example, near $\phi_2 = 0.60$ where we observe the A15 phase in the SCFT phase diagram, the experimental phase diagram shows Hex/A15 and A15/σ two-phase windows. These two-phase windows are composed of the A15 phase and its neighboring phases, HEX at lower ϕ_1 and σ at a higher ϕ_1. As such, we believe that we can reconcile this simple difference by repeating the calculations under the grand-canonical ensemble, which predicts a two-phase window by comparing the chemical potential of neighboring phases [110]. Finally, we also observe stabilization of various sphere forming phases, predominantly C15, past the FCC phase in our SCFT phase diagram. We believe that this region will be effectively destabilized when we perform grand-canonical ensemble calculations accounting for the disordered phase. Indeed, the window of stability for the C15 phase tapers off as we increase χN, similar to the behavior of the disordered phase in the experimental phase diagram as temperature decreases.

Having successfully reproduced the key features of the phase diagram, we examine how the two types of chain selectively partition in the stable phases. To differentiate between the two chemically equivalent chains, we have relabeled the blocks internally within our code and, from this point onward, use the nomenclature shown in Fig. 5.2. We use the notation A,B,C,D to specifically indicates the blocks that we are referring to and eschew the use of A and B to indicate their chemical identity. To describe the chemical identity of the blocks, we will describe the previous A-type monomer as A/C-type and

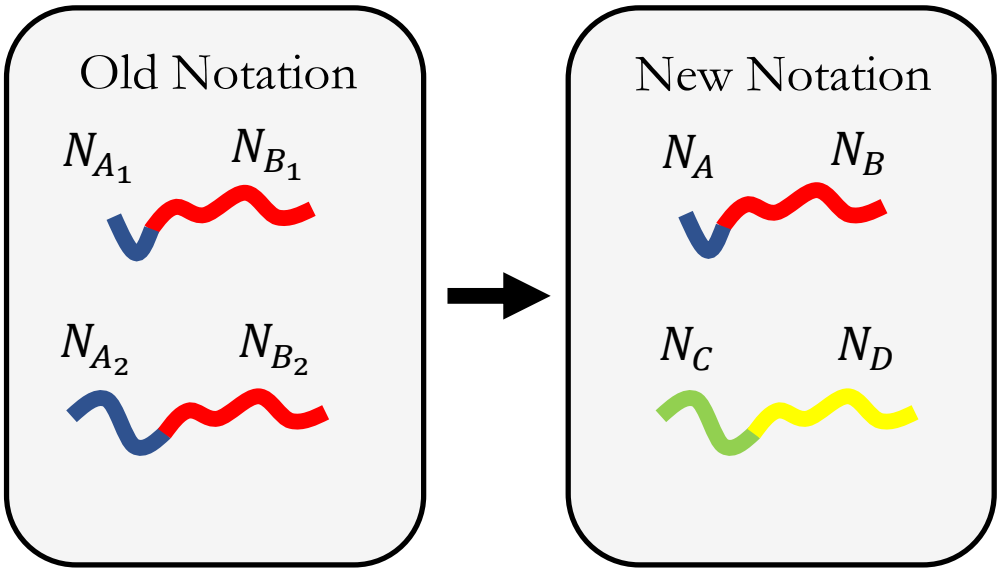

Figure 5.2: Visualization of the change of nomenclature used in examining the partitioning of the two type of diblock copolymer chains. The A/C-blocks are chemically equivalent to the A-block in the old notation and the B/D-blocks are chemically equivalent to the B-block in the old notation.

the previous B-type monomer as B/D-type. To begin, we first examine the partitioning of the chains in the FCC phase at $\chi N = 30, \phi_2 = 0.35$ in Fig. 5.3. We observe the formation of a core-shell micelles in Fig. 5.3a) as indicated by the C-block, which forms the core of the micelles and stretches through a shell of the chemically equivalent but shorter A-block. Since the length of the B-block and D-block are equivalent, the D-block, which is connected to the core of the micelle, penetrates less into the matrix compared to the B-block, which is connected to the shell of the micelle. For symmetric micelles such as those in the FCC phase, we do not observe significant variations in behavior between different directions. The density fields for the HEX and HCP phases behave similarly to the FCC phase (Figs. 5.4-5.5).

We repeated the same analysis for the σ phase at $\chi N = 30, \phi_2 = 0.55$, which unveiled a surprisingly intricate behavior in the density field for the Frank-Kasper σ phase, as

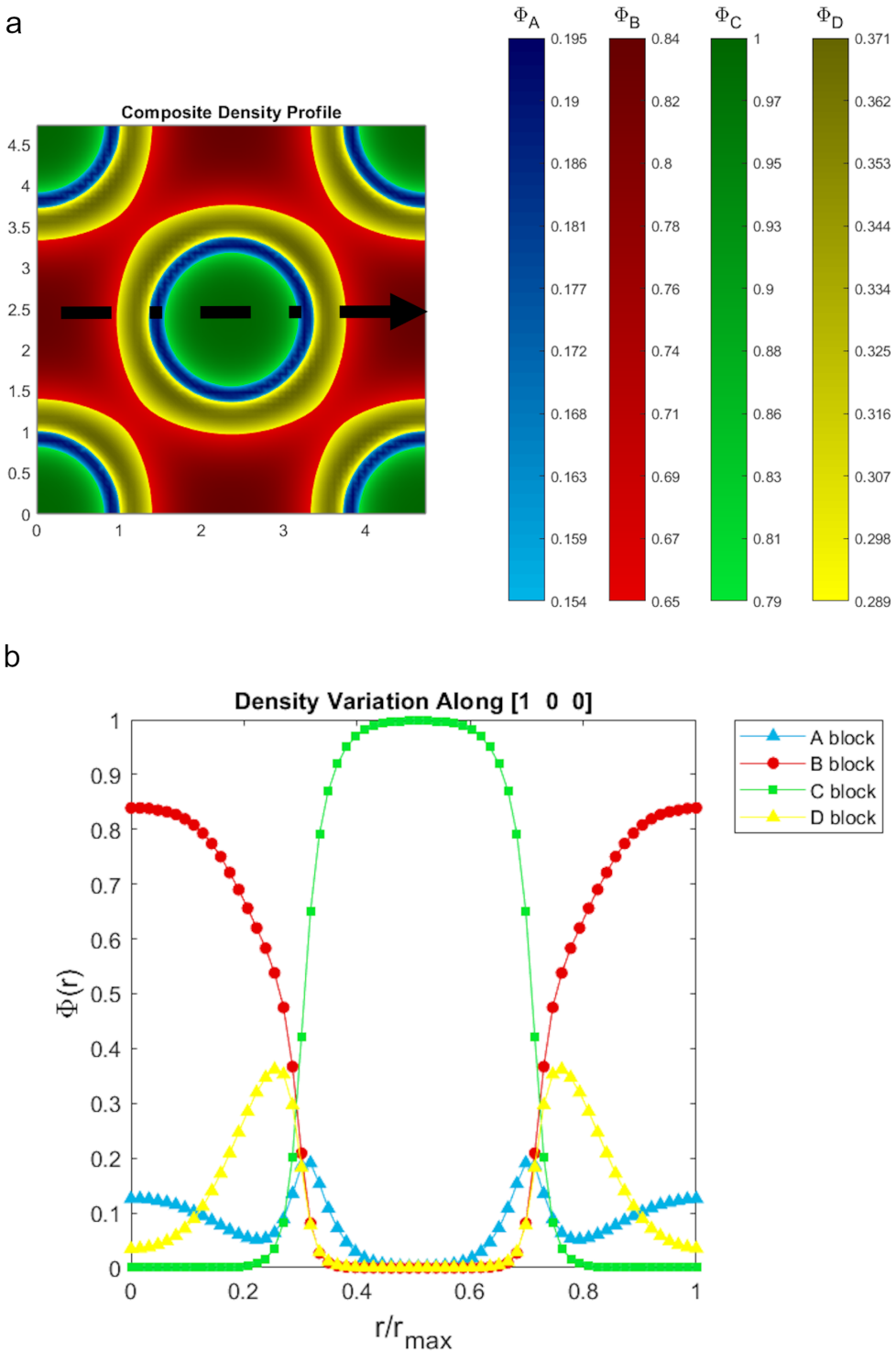

Figure 5.3: a) Side view of the density field for the FCC phase. The broken line indicates the [1 0 0] direction b) Volume fraction of each block in the [1 0 0] direction.

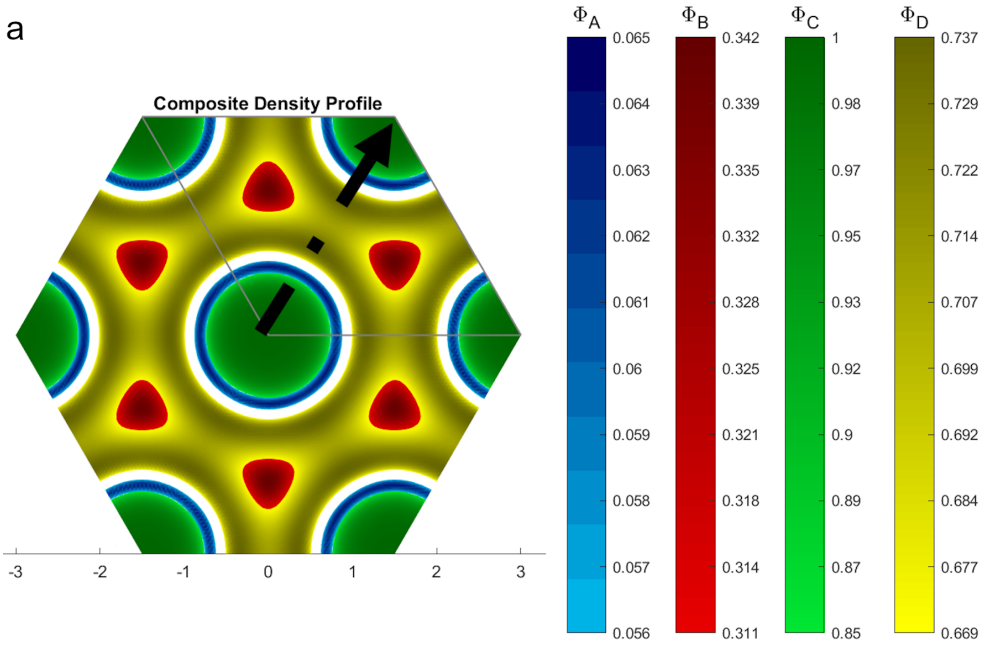

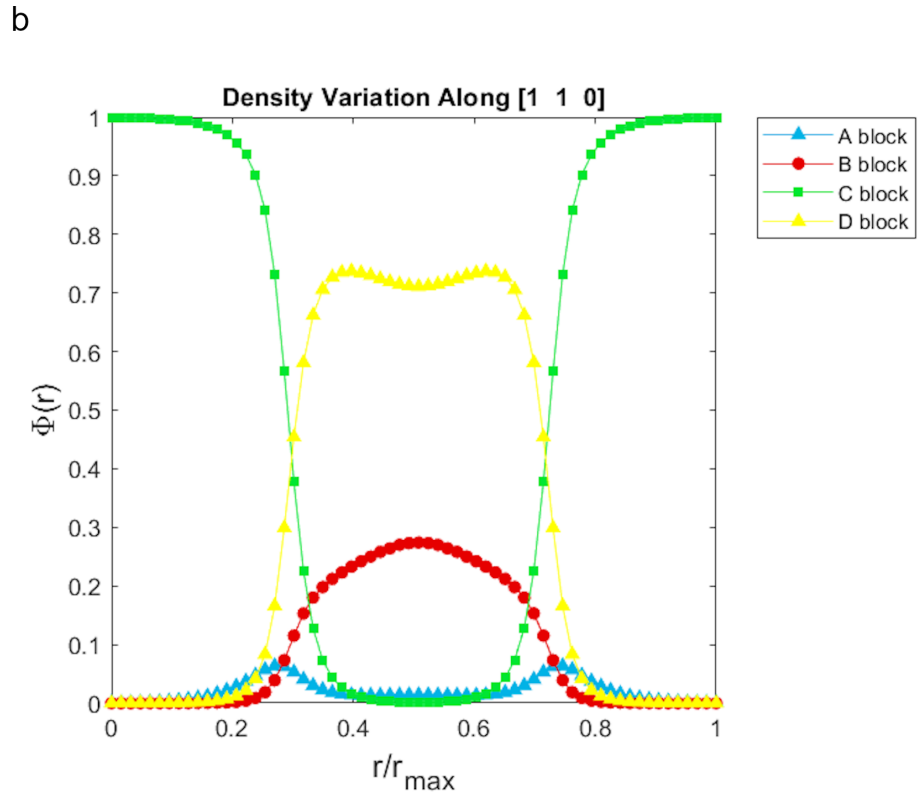

Figure 5.4: a) Top view of the density field for the HEX phase. The broken line indicates the [1 1 0] direction b) Volume fraction of each block in the [1 1 0] direction.

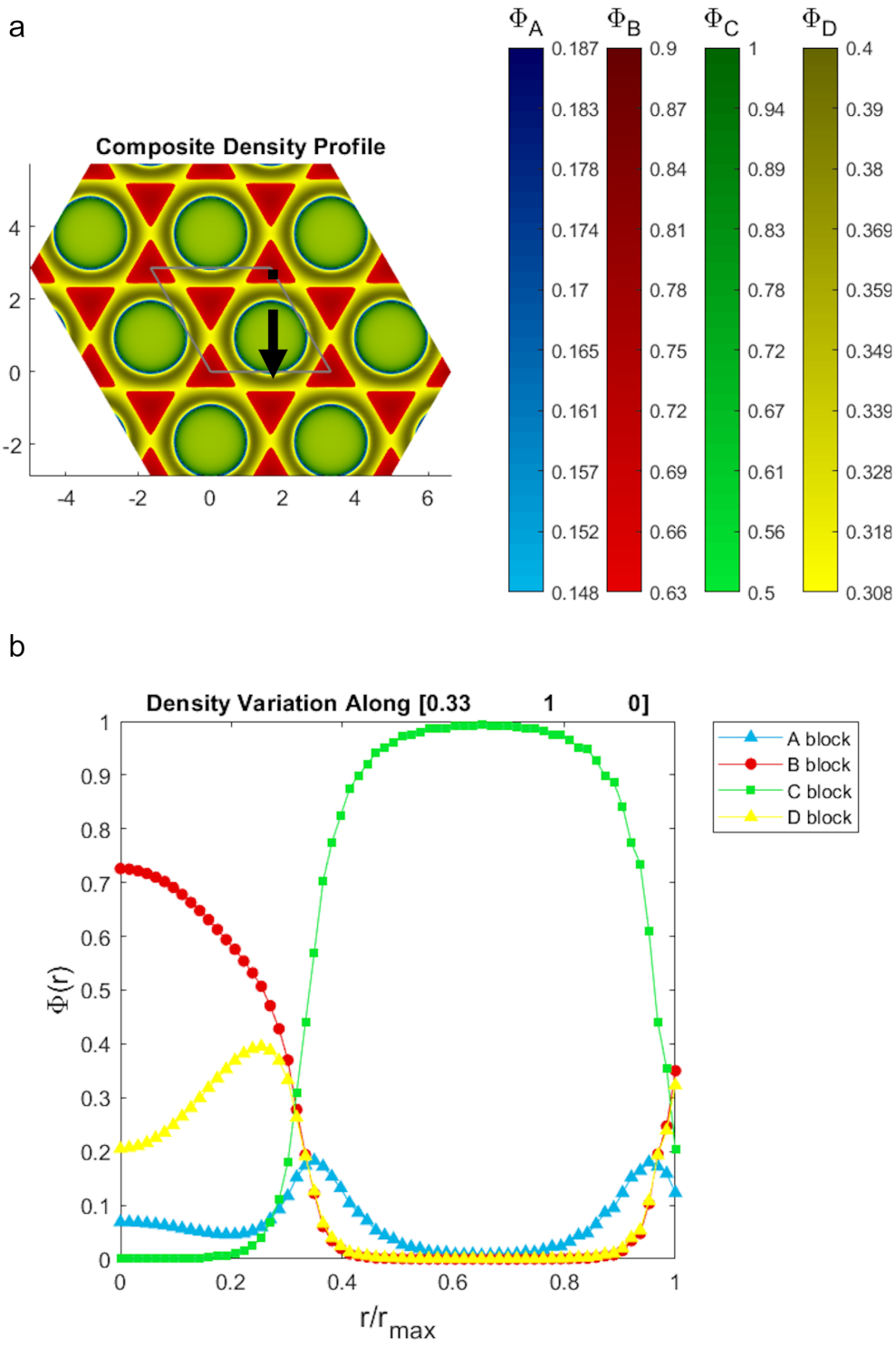

Figure 5.5: a) Top view of the density field for the HCP phase. The broken line indicates the [0.33 1 0] direction b) Volume fraction of each block in the [0.33 1 0] direction.

shown in Fig. 5.6. Particularly, we observe the formation of star-like motifs surrounded by 6 A/C-type micelles. Unlike the FCC phase, where the majority of the matrix is formed by the B-block, we see a re-emergence of the D-block at the core of these star-like motifs. This is easily visualized in Fig. 5.6b) where we see the concentration of the D-block overtaking those of B-block at a normalized distance of 0.35 along the [0.25144 1 0] direction. We also observe the disruption of the core-shell structure in the A/C type micelles. Particularly, there is a selective partitioning of the A-block shell to point towards the core of the star motifs. By examining the density variation along the [0.25144 1 0] direction, we see that the A-block shell density decreases by about 0.05 going from $r/r_{\max} = 0.5$, which points towards the star motif, to $r/r_{\max} = 0.7$, which points towards another micelle. Similar behavior is observed for the stable A15 phase at $\chi N = 30$ and $\phi_2 = 0.6$. As shown in Fig. 5.7, we once again observe the formation of the star motifs surrounded by six A/C type micelles. The center two micelles (Wyckoff position 6d) have shells that selectively point towards the star motifs. The corner micelles (Wyckoff position 2a) have isotropically distributed shells.

5.4 Discussion

Our analysis here has demonstrated a selective partitioning of the shell A-block to point towards the core of the star motifs for asymmetrical micelles. This behavior is not seen in spherically symmetric micelles like those in the FCC, HEX, or HCP phases. The contrast in behavior is most obvious in the A15 phase where we observe both types of partitioning between A15's two types of micelles. Although we are only examining horizontal slices of our simulation volume, our analysis here agrees with those of Liu et al. [70] whereby short chains selectively partition in region of high curvature while longer chains partition in region of low curvature. Indeed, the directions pointing towards the star motifs are regions of high curvature while the directions pointing towards another micelle are of

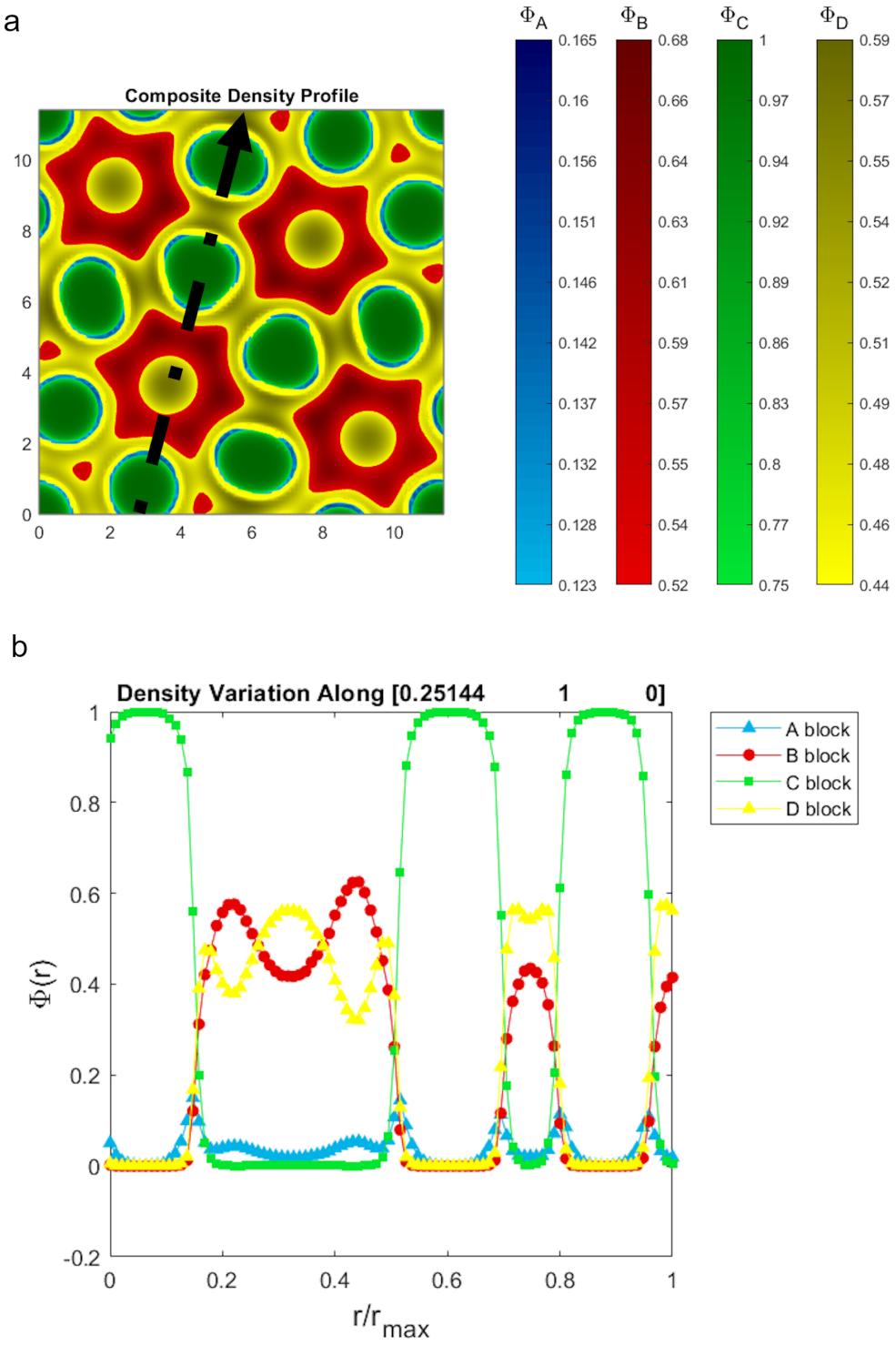

Figure 5.6: a) Top view of the density field for the σ phase. The broken line indicates the [0.25144 1 0] direction b) Volume fraction of each block in the [0.25144 1 0] direction.

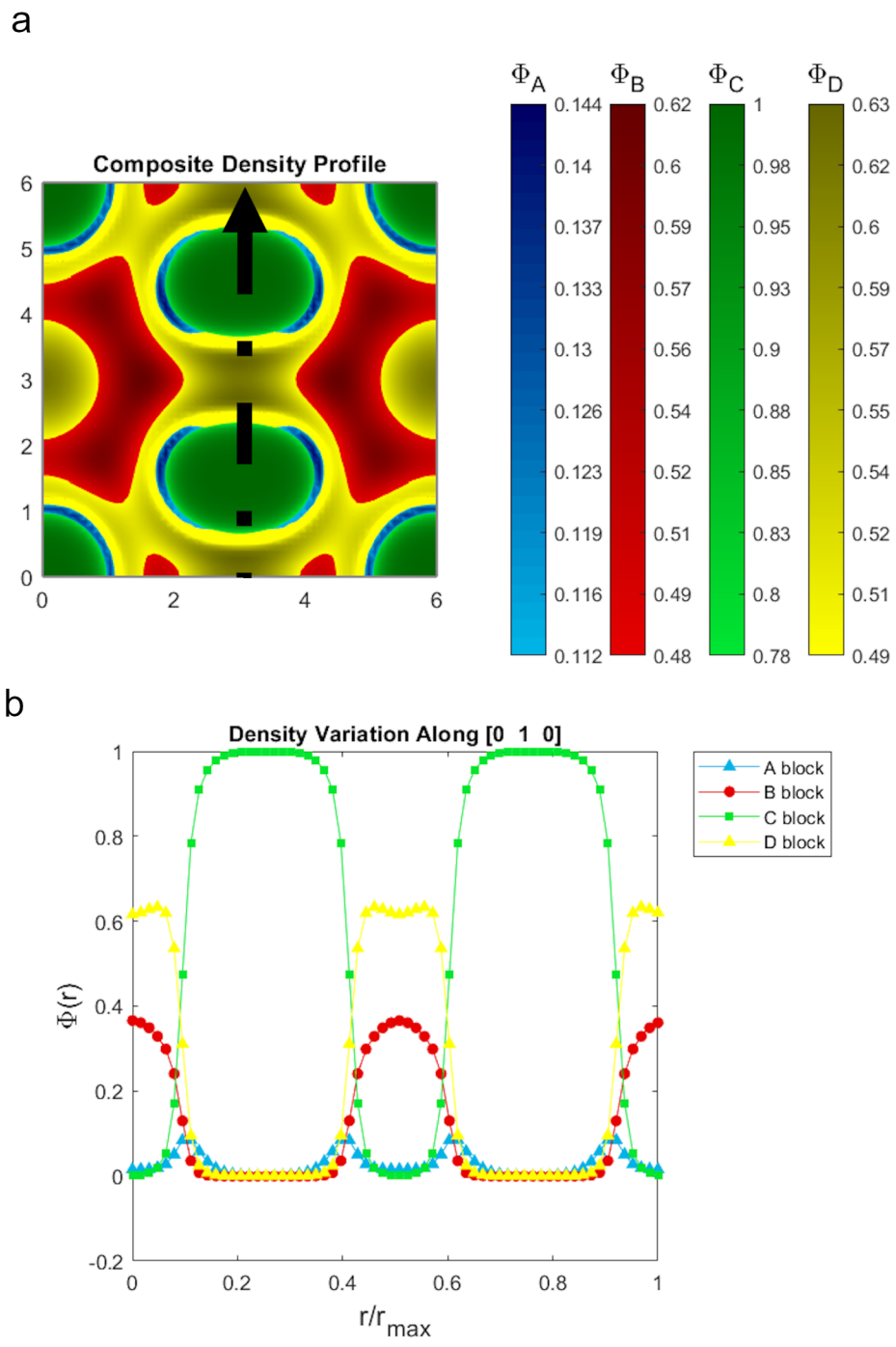

Figure 5.7: a) Top view of the density field for the A15 phase. The broken line indicates the [0 1 0] direction b) Volume fraction of each block in the [0 1 0] direction. The center two micelles (Wyckoff position 6d) have shells that selectively points towards the star motifs. The corner micelles (Wyckoff position 2a) have isotropically distributed shell.

lower curvature. Thus, A-blocks, which are shorter than C-blocks, partition in the direction pointing towards the star motifs.

Besides the selective partitioning of the A-block, we also observe the spontaneous formation of star-like motifs with a pseudo-micelle consisting of the D-block. At the moment, it is unclear if the formation of these star motifs is solely a consequence of the selective partitioning of the A-block or if the formation of the motifs fulfills some function which stabilizes the Frank-Kasper phases. One postulate for the formation of the star motifs is that they act as an anchor point for the surrounding asymmetrical micelles reminiscent of molecular orbital theory. The short AB chains essentially form the bonding orbital that connects the surrounding micelles to the pseudo-micelle D-block. Meanwhile, two neighboring micelles destructively interfere with each other and form an antibonding orbital. This reduces the amount of the AB chains in directions that point to another micelle. Naturally, one could test this idea by reducing B/D-block lengths but keeping the overall volume fraction of the A/C-monomer constant. With shorter chains on average, the formation of the D-block pseudo-micelle, which is far away from the C-block micelle, could be suppressed. While this would allows us to test if the formation of the pseudo-micelle is necessary in stabilizing the Frank-Kasper phases, we expect such a study will require us to sweep through many different combinations of binary blends, which is beyond the scope of this work.

5.5 Conclusion

Our result here highlights the utility of binary blends to stabilize various Frank-Kasper phases as shown by the stabilization of σ and A15 phases. The succesful reproduction of the experimental phase diagram using only canonical ensemble calculations is consistent with previous work which demonstrated SCFT's ability to reproduce experimental results at high $\bar{N}$ [28]. By examining the density field of the stable Frank-Kasper phases,

we observe a potentially new mechanism that cooperatively stabilizes the Frank-Kasper phases alongside with the redistribution of chains of the different lengths in the shell of the micelle [70]. Taken together, the work done here underscores future opportunities to use binary blends of block polymer in a synergistic workflow whereby computational simulation can be use to guide the synthesis of long diblock copolymers for use in practical applications.

Chapter 6

Conclusion and Future Directions

As stated in the introduction of this work, our goal is to understand the mechanism behind the stability of complex sphere forming phases through computational works guided by experimental studies. To this end, we have studied three different block polymer systems which have implications in the formation of Frank-Kasper phases. In this section, we recapitulate the main conclusions of those works and also offer directions for future works relevant to our stated goals.

In Chapter 3, we examined the sphere forming structure in diblock polymer/homopolymer blends which show a sequence of BCC to σ to C14 to C15 transition. Our particle-by-particle analysis shows that the delayed onset of macrophase separation results in the stabilization of phases with increasingly larger volume asymmetry. Recently, the Frank-Kasper Z phase was identified in nanosized shape amphiphiles systems, which is the first of its kind in soft matter [104]. It will be interesting to examine if diblock polymer/homopolymer blends could stabilize the Z phase, which was not considered in our calculation. In fact, there exists a collection of Frank-Kasper phases with varying volume asymmetry that could potentially be stabilized in diblock polymer/homopolymer blends [72]. With the established pattern of increasing volume asymmetry, we can place

the region of stability of all the different Frank Kasper phases, effectively reducing the search space of a potentially very large computational study.

Inline with our stated goals, we examined the window of stability of the disordered micelle regime in Chapter 4. Our results demonstrate that the window of stability for the disordered micelle regime is bracketed by a lower bound of $\chi N_{\mathrm{ODT,SCFT}}$ and an upper bound of χN_{ODT}. From that, we observed a reduced window of stability for conformationally asymmetric system compared to the conformationally symmetric case at a relatively high $\bar{N}$ of 10^4. The natural extension to this work is to examine the same system at a lower value of $\bar{N}$, say $\bar{N} \sim 10^3$, where experimental studies are commonly conducted. As the computational time of MC-FTS increases with decreasing $\bar{N}$, we anticipate that it might be worthwhile to use molecular dynamics calculations instead, which equilibrate faster at low $\bar{N}$. Consistent with the result at compositionally symmetric diblock copolymer, we expect that χN_{ODT} will shift to a even higher value upon decreasing $\bar{N}$ from 10^4 to 10^3. This will widen the window of stability for the disordered micelle phase for both conformationally symmetric and asymmetric diblock copolymer system, perhaps large enough such that we observe the disordered micelle regime at $\epsilon = 3$. The corollary to that is we expect to observe the disordered micelle regime in experimental studies over a broad range of conformational asymmetry.

Our results in Chapter 5 demonstrated the utility of block polymer blends which produce various stable Frank-Kasper phases that could be predicted by SCFT. We discovered patterning of the density field reminiscent of molecular orbital theory which could play a key role in the stabilization of Frank-Kasper phases. One interesting avenue for future work is to examine if the star-motifs play a role in stabilizing Frank-Kasper phases or if they are merely a consequence of the selective redistribution of the two type of chains in the micelle. Another avenue is to test the limit of diblock copolymer blends by computationally searching for other stable Frank-Kasper phases yet to

be seen in diblock copolymer systems, such as the Z phase, and, in turn, confirming it experimentally. This will require a full grand canonical ensemble calculation which multiplicatively increase the computational time. Such study might find synergy when done in combination with modern data-driven techniques such as particle swarm optimization and parameter reducing deep learning techniques.

References

[1] Bates, F. S. *et al.* Multiblock Polymers: Panacea or Pandora's Box. *Science* **336**, 434–440 (2012).

[2] Bates, C. M. & Bates, F. S. 50th Anniversary Perspective: Block Polymers - Pure Potential. *Macromolecules* **50**, 3–22 (2017).

[3] Stoykovich, M. P. *et al.* Directed Self-assembly of Block Co-polymers for Nano-manufacturing. *Directed Self-Assembly of Block Copolymers for Nanolithography: Fabrication of Isolated Features and Essential Integrated Circuit Geometries* **1**, 168–175 (2007).

[4] Hu, H., Gopinadhan, M. & Osuji, C. O. Directed self-Assembly of block copolymers: A tutorial review of strategies for enabling nanotechnology with soft matter. *Soft Matter* **10**, 3867–3889 (2014).

[5] Liu, C.-C. *et al.* Directed self-assembly of block copolymers for 7 nanometre FinFET technology and beyond. *Nature Electronics* **1**, 562–569 (2018).

[6] Jackson, E. A. & Hillmyer, M. A. Nanoporous membranes derived from block copolymers: From drug delivery to water filtration. *ACS Nano* **4**, 3548–3553 (2010).

[7] Phillip, W. A., O'neill, B., Rodwogin, M., Hillmyer, M. A. & Cussler, E. L. Self-assembled block copolymer thin films as water filtration membranes. *ACS Applied Materials and Interfaces* **2**, 847–853 (2010).

[8] Nunes, S. P. Block Copolymer Membranes for Aqueous Solution Applications. *Macromolecules* **49**, 2905–2916 (2016).

[9] Sveinbjörnsson, B. R. *et al.* Rapid self-assembly of brush block copolymers to photonic crystals. *Proceedings of the National Academy of Sciences of the United States of America* **109**, 14332–14336 (2012).

[10] Macfarlane, R. J. *et al.* Improving brush polymer infrared one-dimensional photonic crystals via linear polymer additives. *Journal of the American Chemical Society* **136**, 17374–17377 (2014).

[11] Schwab, M. & Stuhn, B. Thermotropic Transition from a State of Liquid Order to a Macrolattice in Asymmetric Diblock Copolymers. *Phys. Rev. Lett.* **76**, 924–927 (1996).

[12] Frank, F. C. & Kasper, J. S. Complex Alloy Structures Regarded as Sphere Packings. I. Definitions and Basic Principles. *Acta Crystallogr.* **11**, 184–190 (1958).

[13] Frank, F. C. & Kasper, J. S. Complex Alloy Structures Regarded as Sphere Packings. II. Analysis and Classification of Representative Structures. *Acta Crystallogr.* **12**, 483–499 (1959).

[14] Lee, S., Bluemle, M. J. & Bates, F. S. Discovery of a Frank-Kasper σ phase in sphere-forming block copolymer melts. *Science* **330**, 349–353 (2010).

[15] Bates, M. W. *et al.* Stability of the A15 phase in diblock copolymer melts. *Proc. Natl. Acad. Sci. USA* **116**, 13194–13199 (2019).

[16] Bates, M. W. *et al.* Synthesis and Self-Assembly of AB_n miktoarm star polymers. *ACS Macro Lett.* **9**, 396–403 (2020).

[17] Jeon, S. *et al.* Frank–Kasper Phases Identified in PDMS-b-PTFEA Copolymers with High Conformational Asymmetry. *Macromolecular Rapid Communications* **40**, 1900259 (2019).

[18] Schulze, M. W. *et al.* Conformational asymmetry and quasicrystal approximants in linear diblock copolymers. *Phys. Rev. Lett.* **118**, 207801 (2017).

[19] Lachmayr, K. K., Wentz, C. M. & Sita, L. R. An exceptionally stable and scalable sugar-polyolephin Frank-Kasper A15 phase. *Angew. Chem. Intl. Ed.* **59**, 1521–1526 (2020).

[20] Kim, K. *et al.* Thermal processing of diblock copolymer melts mimics metallurgy. *Science* **356**, 520–523 (2017).

[21] Kim, K. *et al.* Origins of low-symmetry phases in asymmetric diblock copolymer melts. *Proc. Natl. Acad. Sci. USA* **115**, 847–854 (2018).

[22] Gillard, T. M., Lee, S. & Bates, F. S. Dodecagonal quasicrystalline order in a diblock copolymer melt. *Proc. Natl. Acad. Sci. USA* **113**, 5167–5172 (2016).

[23] Lee, S., Gillard, T. M. & Bates, F. S. Fluctuations, Order, and Disorder in Short Diblock Copolymers. *AIChE Journal* **59**, 3052 (2013). `0201037v1`.

[24] Fredrickson, G. H. *The Equilibrium Theory of Inhomogeneous Polymers* (Oxford Science Publication, 2006).

[25] Matsen, M. W. The standard Gaussian model for block copolymer melts. *Journal of Physics Condensed Matter* **14**, 21–47 (2002).

[26] Matsen, M. W. Field theoretic approach for block polymer melts: SCFT and FTS. *Journal of Chemical Physics* **152**, 110901 (2020).

[27] Khandpur, A. K. *et al.* Polyisoprene-polystyrene diblock copolymer phase diagram near the order-disorder transition. *Macromolecules* **28**, 8796–8806 (1995).

[28] Lewis III, R. M. *et al.* Role of chain length in the formation of Frank-Kasper phases in diblock copolymers. *Phys. Rev. Lett.* **121**, 208002 (2018).

[29] Vavasour, J. D. & Whitmore, M. D. Self-Consistent Field Theory of Block Copolymers with Conformational Asymmetry. *Macromolecules* **26**, 7070–7075 (1993).

[30] Matsen, M. W. & Schick, M. Stable and unstable phases of a diblock copolymer melt. *Physical Review Letters* **72**, 2660–2663 (1994).

[31] Xie, N., Li, W., Qiu, F. & Shi, A.-C. σ phase formed in conformationally asymmetric AB-type block copolymers. *ACS Macro Lett.* **3**, 906–910 (2014).

[32] Fredrickson, G. H. & Helfand, E. Fluctuation effects in the theory of microphase separation in block copolymers. *J. Chem. Phys.* **87**, 697–705 (1987).

[33] Tyler, C. A. & Morse, D. C. Orthorhombic Fddd network in triblock and diblock copolymer melts. *Physical Review Letters* **94**, 208302 (2005).

[34] Liu, M., Li, W., Qiu, F. & Shi, A.-C. Stability of the Frank-Kasper σ-phase in BABC linear tetrablock terpolymers. *Soft Matter* **12**, 6412–6421 (2016).

[35] Deng, H., Li, W., Qiu, F. & Shi, A. C. Self-Assembled Morphologies of Linear and Miktoarm Star Triblock Copolymer Monolayers. *Journal of Physical Chemistry B* **121**, 4642–4649 (2017).

[36] Zhao, M. & Li, W. Laves phases formed in the binary blend of AB_4 miktoarm star copolymer and A-homopolymer. *Macromolecules* **52**, 1832–1842 (2019).

[37] Levi, A. E. *et al.* Miktoarm Stars via Grafting-Through Copolymerization: Self-Assembly and the Star-to-Bottlebrush Transition. *Macromolecules* **52**, 1794–1802 (2019).

[38] Gadelrab, K. R. & Alexander-Katz, A. Effect of molecular architecture on the self-assembly of bottlebrush copolymers. *Journal of Physical Chemistry B* **124**, 11519–11529 (2020).

[39] Sides, S. W. & Fredrickson, G. H. Continuous polydispersity in a self-consistent field theory for diblock copolymers. *Journal of Chemical Physics* **121**, 4974–4986 (2004).

[40] Cooke, D. M. & Shi, A. C. Effects of polydispersity on phase behavior of diblock copolymers. *Macromolecules* **39**, 6661–6671 (2006).

[41] Matsen, M. W. Polydispersity-induced macrophase separation in diblock copolymer melts. *Physical Review Letters* **99**, 148304 (2007).

[42] Muller M & Schmid F. Incorporating fluctuations and dynamics in self-consistent field theories for polymer blends. *Advances in Polymer Science* **185**, 1–58 (2005).

[43] Hannon, A. F., Gotrik, K. W., Ross, C. A. & Alexander-Katz, A. Inverse design of topographical templates for directed self-assembly of block copolymers. *ACS Macro Lett.* **2**, 251–255 (2013).

[44] Hannon, A. F., Ding, Y., Bai, W., Ross, C. A. & Alexander-Katz, A. Optimizing topographical templates for directed self-assembly of block copolymers via inverse design simulations. *Nano Lett.* **14**, 318–325 (2014).

[45] Paradiso, S. P., Delaney, K. T. & Fredrickson, G. H. Swarm Intelligence Platform for Multiblock Polymer Inverse Formulation Design. *ACS Macro Lett.* **5**, 972–976 (2016).

[46] Tsai, C. L., Delaney, K. T. & Fredrickson, G. H. Genetic Algorithm for Discovery of Globally Stable Phases in Block Copolymers. *Macromolecules* **49**, 6558–6567 (2016).

[47] Khadilkar, M. R., Paradiso, S., Delaney, K. T. & Fredrickson, G. H. Inverse Design of Bulk Morphologies in Multiblock Polymers Using Particle Swarm Optimization. *Macromolecules* **50**, 6702–6709 (2017).

[48] Ouaknin, G. Y., Laachi, N., Delaney, K. T., Fredrickson, G. H. & Gibou, F. Level-set strategy for inverse DSA-lithography. *J. Comput. Phys.* **375**, 1159–1178 (2018).

[49] Zhang, R., Zhang, L., Lin, J. & Lin, S. Customizing topographical templates for aperiodic nanostructures of block copolymers via inverse design. *Phys. Chem. Chem. Phys.* **21**, 7781–7788 (2019).

[50] Arora, A. *et al.* Broadly accessible self-consistent field theory for block polymer materials discovery. *Macromolecules* **49**, 4675–4690 (2016).

[51] http://pscf.cems.umn.edu.

[52] Tyler, C., Qin, J., Bates, F. S. & Morse, D. C. SCFT Study of Nonfrustrated ABC Triblock Copolymer Melts. *Macromolecules* **40**, 4654 (2007).

[53] Ranjan, A., Qin, J. & Morse, D. C. Linear response and stability of ordered phases of block copolymers. *Macromolecules* **41**, 942 (2008).

[54] Qin, J., Bates, F. C. & Morse, D. C. Phase behavior of nonfrustrated ABC triblock copolymers: Weak and intermediate segregation. *Macromolecules* **43**, 5128 (2010).

[55] Glaser, J., Medapuram, P., Beardsley, T. M., Matsen, M. W. & Morse, D. C. Universality of block copolymer melts. *Physical Review Letters* **113**, 68302 (2014).

[56] Medapuram, P., Glaser, J., Beardsley, T. M., Matsen, M. W. & Morse, D. C. Universal phenomenology of symmetric diblock copolymers near the order-disorder transition. *Macromolecules* **48**, 819 (201).

[57] Chanpuriya, S. *et al.* Cornucopia of nanoscale ordered phases in sphere-forming tetrablock terpolymers. *ACS Nano* **10**, 4961–4972 (2016).

[58] Radlauer, M. R. *et al.* Morpohological Consequences of Frustration in ABC Triblock Polymers. *Macromolecules* **50**, 446–458 (2017).

[59] Burke, C. J. & Grason, G. M. Intradomain phase transitions in flexible block copolymers with self-aligning segments. *J. Chem. Phys.* **148**, 174905 (2018).

[60] Burns, A. B. & Register, R. A. Large, reversible, and coherent domain spacing dilation driven by crystallization under soft lamellar confinement. *Macromolecules* **50**, 8106–8116 (2916).

[61] Prasad, I., Seo, Y., Hall, L. M. & Grason, G. M. Intradomain Textures in Block Copolymers: Multizone Alignment and Biaxiality. *Phys. Rev. Lett.* **118**, 247801 (2017).

[62] Prasad, I., Jinnai, H., Ho, R. M., Thomas, E. L. & Grason, G. M. Anatomy of triply-periodic network assemblies: characterizing skeletal and inter-domain surface geometry of block copolymer gyroids. *Soft Matter* **14**, 3612–3623 (2018).

[63] Dane, C., Register, R. A. & Priestley, R. D. Role of chain connectivity across an interface on the dynamics of a nanostructured block copolymer. *Phys. Rev. Lett.* **121**, 247801 (2018).

[64] Christie, D., Register, R. A. & Priestley, R. D. Direct Measurement of the Local Glass Transition in Self-Assembled Copolymers with Nanometer Resolution. *ACS Cent. Sci.* **4**, 504–511 (2018).

[65] Yadav, M., Bates, F. S. & Morse, D. C. Network model of the disordered phase in symmetric diblock copolymer melts. *Physical Review Letters* **121**, 127802 (2018).

[66] Burns, A. B., Christie, D., Mulhearn, W. D. & Register, R. A. Estimating the segregation strength of microphase-separated diblock copolymers from the interfacial width. *J. Polym. Sci. B Polym. Phys.* **57**, 932–940 (2019).

[67] Yadav, M., Bates, F. S. & Morse, D. C. Effect of segment length asymmetry in ternary diblock copolymer - homopolymer mixtures. *Macromolecules* **52**, 4091 (2019).

[68] Feng, X. *et al.* Seeing mesoatom distortions in soft-matter crystals of a double-gyroid block copolymer. *Nature* **575**, 175–179 (2019).

[69] Lee, S., Leighton, C. & Bates, F. S. Sphericity and symmetry breaking in the formation of Frank-Kasper phases from one component materials. *Proc. Natl. Acad. Sci. USA* **111**, 17723–17731 (2014).

[70] Liu, M., Qiang, Y., Li, W., Qiu, F. & Shi, A.-C. Stabilizing the Frank-Kasper phases via binary blends of AB diblock copolymers. *ACS Macro Lett.* **5**, 1167–1171 (2016).

[71] Takagi, H., Hashimoto, R., Igarashi, N., Kishimoto, S. & Yamamoto, K. Frank-Kasper σ phase in polybutadiene-poly(ε-caprolactone) diblock copolymer/polybutadiene blends. *J. Phys. Condens. Matter* **29**, 204002 (2017).

[72] Reddy, A. *et al.* Stable Frank-Kasper phases of self-assembled, soft matter spheres. *Proc. Natl. Acad. Sci. USA* **115**, 10233–10238 (2018).

[73] Takagi, H. & Yamamoto, K. Phase boundary of Frank-Kasper σ phase in phase diagrams of binary mixtures of block copolymers and homopolymers. *Macromolecules* **52**, 2007–2014 (2019).

[74] Arora, A., Morse, D. C., Bates, F. S. & Dorfman, K. D. Accelerating self-consistent field theory of block polymers in a variable unit cell. *J. Chem. Phys.* **146**, 244902 (2017).

[75] Delaney, K. T. & Fredrickson, G. H. Polymer field-theory simulations on graphics processing units. *Comput. Phys. Commun.* **184**, 2102–2110 (2013).

[76] Matsen, M. W. Fast and accurate SCFT calculations for periodic block-copolymer morphologies using the spectral method with Anderson mixing. *Eur. Phys. J. E* **30**, 361–369 (2009).

[77] Stasiak, P. & Matsen, M. W. Efficiency of pseudo-spectral algorithms with Anderson mixing for the SCFT of periodic block-copolymer phases. *Eur. Phys. J. E* **34**, 110 (2011).

[78] Tyler, C. A. & Morse, D. C. Stress in self consistent field theory. *Macromolecules* **36**, 8184–8188 (2003).

[79] https://github.com/dmorse/pscfpp.

[80] Audus, D. J., Delaney, K. T., Ceniceros, H. D. & Fredrickson, G. H. Comparison of Pseudospectral Algorithms for Field-Theoretic Simulations of Polymers. *Macromolecules* **46**, 8383–8391 (2013).

[81] Thompson, R. B., Rasmussen, K. O. & Lookman, T. Improved convergence in block copolymer self-consistent field theory by Anderson mixing. *J. Chem. Phys.* **120**, 31–34 (2004).

[82] Dutour Sikirić, M., Delgado-Friedrichs, O. & Deza, M. Space fullerenes: A computer search for new Frank-Kasper structures. *Acta Crystallogr. A* **66**, 602–615 (2010).

[83] Duchs, D., Ganesan, V., Fredrickson, G. H. & Schmid, F. Fluctuation Effects in Ternary AB + A + B Polymeric Emulsions. *Macromolecules* **36**, 9237–9248 (2003).

[84] Stasiak, P. & Matsen, M. W. Monte Carlo Field-Theoretic Simulations for Melts of Symmetric Diblock Copolymer. *Macromolecules* **46**, 8037–8045 (2013).

[85] Vorselaars, B., Stasiak, P. & Matsen, M. W. Field-Theoretic Simulation of Block Copolymers at Experimentally Relevant Molecular Weights. *Macromolecules* **48**, 9071–9080 (2015).

[86] Spencer, R. K. W., Vorselaars, B. & Matsen, M. W. Continuous Thermodynamic Integration in Field-Theoretic Simulations of Structured Polymers. *Macromol. Theory Simul.* **26**, 1700036 (2017).

[87] Beardsley, T. M., Spencer, R. K. W. & Matsen, M. W. Computationally Efficient Field-Theoretic Simulations for Block Copolymer Melts. *Macromolecules* **52**, 8840–8848 (2019).

[88] de la Cruz, M., Edwards, S. F. & Sanchez, I. C. Concentration fluctuations in polymer blend thermodynamics. *J. Chem. Phys.* **89**, 1704–1708 (1988).

[89] Morse, D. C. & Qin, J. Relationships among coarse-grained field theories of fluctuations in polymer liquids. *J. Chem. Phys.* **134**, 84902 (2011).

[90] Delaney, K. T. & Fredrickson, G. H. Recent Developments in Fully Fluctuating Field-Theoretic Simulations of Polymer Melts and Solutions. *J. Phys. Chem. B* **120**, 7615–7634 (2016).

[91] Eitouni, H. B., Balsara, N. P., Hahn, H., Pople, J. A. & Hempenius, M. A. Thermodynamic Interactions in Organometallic Block Copolymers: Poly(styrene-block-ferrocenyldimethylsilane). *Macromolecules* **35**, 7765–7772 (2002).

[92] Leibler, L. Theory of microphase separation in block copolymers. *Macromolecules* **13**, 1602–1617 (1980).

[93] Matsen, M. W. & Bates, F. S. Unifying weak- and strong-segregation block copolymer theories. *Macromolecules* **29**, 1091–1098 (1996).

[94] Cochran, E. W., Garcia-Cervera, C. J. & Fredrickson, G. H. Stability of the gyroid phase in diblock copolymers at strong segregation. *Macromolecules* **39**, 2449–2451 (2006).

[95] Ungar, G., Liu, Y., Zeng, X., Percec, V. & Cho, W. D. Giant supramolecular liquid crystal lattice. *Science* **299**, 1208–1211 (2003).

[96] Zeng, X. *et al.* Supramolecular dendtritic liquid quasicrystals. *Nature* **428**, 157–160 (2004).

[97] Vargas, R., Mariani, P., Gulik, A. & Luzzati, V. Cubic phases of lipid-containing systems: The structure of phase Q^{223} (space group Pm3n). An X-ray scattering study. *J. Mol. Biol.* **225**, 137–1345 (1992).

[98] Seddon, J. M., Zeb, N., Templer, R. H., McElhaney, R. N. & Mannock, D. A. An Fd3m lyotropic cubic phase in a binary glycolipid/water system. *Langmuir* **12**, 5250–5253 (1996).

[99] Ungar, G. & Zeng, X. Frank-Kasper, quasicrystalline and related phases in liquid crystals. *Soft Matter* **1**, 95–106 (2005).

[100] Perroni, D. V. & Mahanthappa, M. K. Inverse $Pm\bar{3}n$ cubic micellar lyotropic phases from zwitterionic triazolium gemeni surfactants. *Soft Matter* **9**, 7919–7922 (2013).

[101] Baez-Cotto, C. M. & Mahanthappa, M. K. Micellar mimicry of intermetallic C14 and C15 Laves phases by aqueous self-assembly. *ACS Nano* **12**, 3226–3234 (2018).

[102] Huang, M. *et al.* Selective assemblies of giant tetrahedra via precisely controlled positional interactions. *Science* **348**, 424–428 (2015).

[103] Yue, K. *et al.* Geometry induced sequence of nanoscale Frank-Kasper and quasicrystal mesophases in giant surfactants. *Proc. Natl. Acad. Sci. USA* **113**, 14195–14200 (2016).

[104] Su, Z. *et al.* Identification of a Frank-Kasper Z phase from shape amphiphile self-assembly. *Nat. Chem.* **11**, 899–905 (2019).

[105] Grason, G. M., DiDonna, B. A. & Kamien, R. D. Geometric theory of diblock copolymer phases. *Phys. Rev. Lett.* **91**, 58304 (2003).

[106] Lindsay, A. P. *et al.* A15, σ and a quasicrystal: Access to complex particle packings via bidisperse diblock copolymer blends. *ACS Macro Lett.* **9**, 197–203 (2020).

[107] Li, W., Duan, C. & Shi, A.-C. Nonclassical spherical packing phases self-assembled from AB-type block copolymers. *ACS Macro Lett.* **6**, 1257–1262 (2017).

[108] Mueller, A. J. *et al.* Emergence of a C15 Laves phase in diblock polymer/homopolymer blends. *ACS Macro Lett.* **9**, 576–582 (2020).

[109] Semenov, A. N. Phase equllibria in block copolymer-homopolymer mixtures. *Macromolecules* **26**, 2273–2281 (1993).

[110] Matsen, M. W. Phase behavior of block copolymer/homopolymer blends. *Macromolecules* **28**, 5765–5773 (1995).

[111] Arora, A., Pillai, N., Bates, F. S. & Dorfman, K. D. Predicting the phase behavior of ABAC tetrablock terpolymers: Sensitivity to Flory-Huggins interaction parameters. *Polymer* **154**, 305–314 (2018).

[112] Koizumi, S., Hasegawa, H. & Hashimoto, T. Spatial distribution of homopolymers in block copolymer microdomains as observed by a combined SANS and SAXS method. *Macromolecules* **27**, 7893–7906 (1994).

[113] Peng, H.-G. *et al.* Distributions of a linear homopolymer additive in an ordered block copolymer matrix as quantified by small-angle neutron scattering. *Macromolecules* **48**, 7574–7584 (2015).

[114] Tamai, Y., Sekine, R., Aoki, H. & Ito, S. Conformation of single homopolymer chain in microphase-separated block copolymer monolayer studied by scanning near-field optical microscopy. *Macromolecules* **42**, 4224–4229 (2009).

[115] Dormitontova, E. E. & Lodge, T. P. The Order-Disorder Transition and the Disordered Micelle Regime in Sphere-Forming Block Copolymer Melts. *Macromolecules* **34**, 9143–9155 (2001).

[116] Wang, J., Wang, Z.-G. & Yang, Y. Nature of Disordered Micelles in Sphere-Forming Block Copolymer Melts. *Macromolecules* **38**, 1979–1988 (2005).

[117] Ghasimakbari, T. & Morse, D. C. Correlations in Disordered Melts of Asymmetric Diblock Copolymers. *Macromolecules* **51**, 2335–2348 (2018).

[118] Fredrickson, G. H., Ganesan, V. & Drolet, F. Field-Theoretic Computer Simulation Methods for Polymers and Complex Fluids. *Macromolecules* **35**, 16–39 (2002).

[119] Cheong, G. K., Chawla, A., Morse, D. C. & Dorfman, K. D. Open-source code for self-consistent field theory calculations of block polymer phase behavior on graphics processing units. *Eur. Phys. J. E* **43**, 15 (2020).

[120] Beardsley, T. M. & Matsen, M. W. Fluctuation correction for the order–disorder transition of diblock copolymer melts. *The Journal of Chemical Physics* **154**, 124902 (2021). URL `https://doi.org/10.1063/5.0046167`.

[121] Ghasimakbari, T. & Morse, D. C. Order-Disorder Transitions and Free Energies in Asymmetric Diblock Copolymers. *Macromolecules* **53**, 7399–7409 (2020).

[122] Ndoni, S., Papadakis, C. M., Bates, F. S. & Almdal, K. Laboratory-scale setup for anionic polymerization under inert atmosphere. *Review of Scientific Instruments* **66**, 1090–1095 (1995).

Appendix A

Supplementary Information to Chapter 3

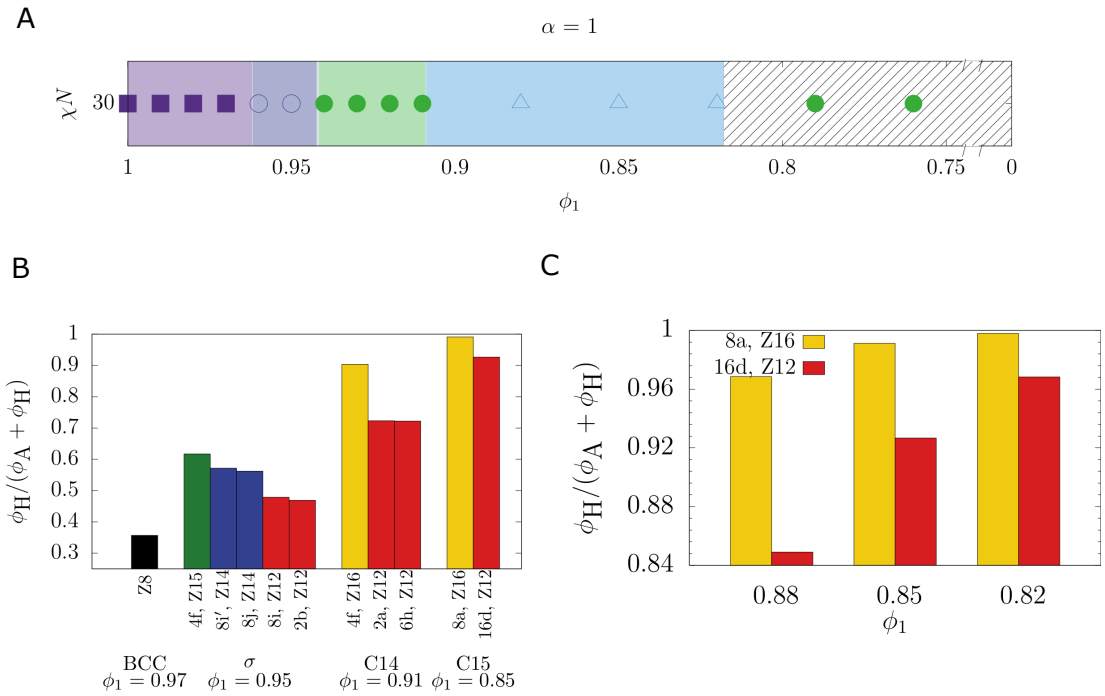

Figure A.1: Analysis for diblock copolymer-monomer blend at $\epsilon = 1.7$, $\chi N = 30$ for the dry brush case $\alpha = 1$, equivalent to those done in the main text for $\epsilon = 1.7$, $\chi N = 25$. (A) Phase diagram of the diblock copolymer-monomer blend at $\epsilon = 1.7$ and $\chi N = 30$. The symbols indicate state points for SCFT calculations in the canonical ensemble. Phase boundaries between these state points were obtained by grand canonical ensemble calculations. Symbols correspond to bcc (■, dark purple), σ (○, light purple), C14 (●, green), and C15 (△, blue). Phase boundaries between states were obtained from grand canonical ensemble calculations. Two-phase regions between ordered states are indicated by light shading; in many cases, these regions are too narrow to be depicted. The hashed areas indicate two-phase regions that correspond to equilibrium between an ordered phase and a disordered phase. (B) Volume fraction of the homopolymer, ϕ_H, relative to the total volume fraction of A monomers at the center of a micellar particle, $\phi_A + \phi_H$, for the dry brush case $\alpha = 1$. The notation refers to the Wykoff positions of the particles and the number of faces in the polyhedra. (C) Volume fraction of the homopolymer, ϕ_H, relative to the total volume fraction of A monomers at the center of a micellar particle, $\phi_A + \phi_H$, for C15 at $\alpha = 1$. The color coding corresponds to panel (B).

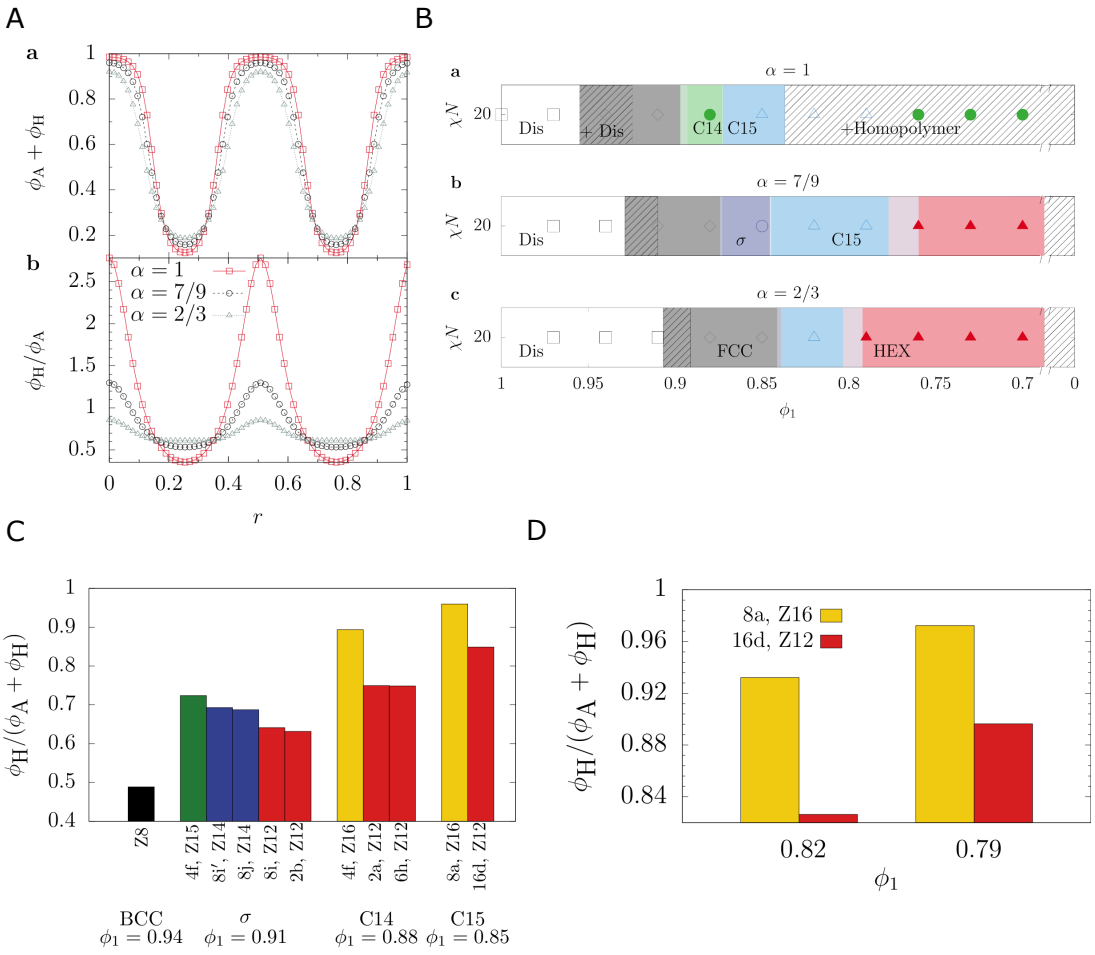
A
a
b
$\phi_A + \phi_H$
ϕ_H/ϕ_A
$\alpha = 1$
$\alpha = 7/9$
$\alpha = 2/3$
r
B
a
b
c
$\alpha = 1$
$\alpha = 7/9$
$\alpha = 2/3$
χN
Dis
+ Dis
C14 C15
+Homopolymer
σ
C15
FCC
HEX
ϕ_1
C
D
$\phi_H/(\phi_A + \phi_H)$
Z8
4f, Z15
8i', Z14
8j, Z14
8i, Z12
2b, Z12
4f, Z16
2a, Z12
6h, Z12
8a, Z16
16d, Z12
BCC
$\phi_1 = 0.94$
σ
$\phi_1 = 0.91$
C14
$\phi_1 = 0.88$
C15
$\phi_1 = 0.85$
8a, Z16
16d, Z12
0.82
0.79
ϕ_1

Figure A.2: Analysis for diblock copolymer-monomer blend at $\epsilon = 1.7$, $\chi N = 20$, equivalent to those done in the main text for $\epsilon = 1.7$, $\chi N = 25$. The analysis of bcc and σ phase here use metastable states; fcc is the stable state but destabilizes as χN increases. (A) Illustration of the transition from dry brush to wet brush regimes as the homopolymer molecular weight decreases. (a) Volume fraction of the A monomers in the bcc phase at $\phi_1 = 0.90$ along the [111] direction for $\alpha = 1$ (red squares) and $\alpha = 7/9$ (black circles), where the position is made dimensionless with $\sqrt{3}a$ for the unit-cell parameter a. (b) Ratio of the A-homopolymer to A-block volume fractions for the conditions in (a). (B) Phase diagram of the diblock copolymer-monomer blend at $\epsilon = 1.7$ and $\chi N = 20$. The symbols indicate state points for SCFT calculations in the canonical ensemble. Phase boundaries between these state points were obtained by grand canonical ensemble calculations. Symbols correspond to fcc ($\diamond$, gray), σ ($\bigcirc$, light purple), C14 ($\bullet$, green), C15 ($\triangle$, blue), and hexagonally-packed (hex) cylinders ($\blacktriangle$, red). Two-phase regions between ordered states are indicated by light shading. The hashed areas indicate two-phase regions that correspond to equilibrium between an ordered phase and a disordered phase. (C) Volume fraction of the homopolymer, ϕ_H, relative to the total volume fraction of A monomers at the center of a micellar particle, $\phi_A + \phi_H$, for the dry brush case $\alpha = 1$. The notation refers to the Wykoff positions of the particles and the number of faces in the polyhedra. The inset shows the planar graph forms of each of the polyhedra. (D) Volume fraction of the homopolymer, ϕ_H, relative to the total volume fraction of A monomers at the center of a micellar particle, $\phi_A + \phi_H$, for C15 at $\alpha = 0.78$. The color coding corresponds to panel (C).

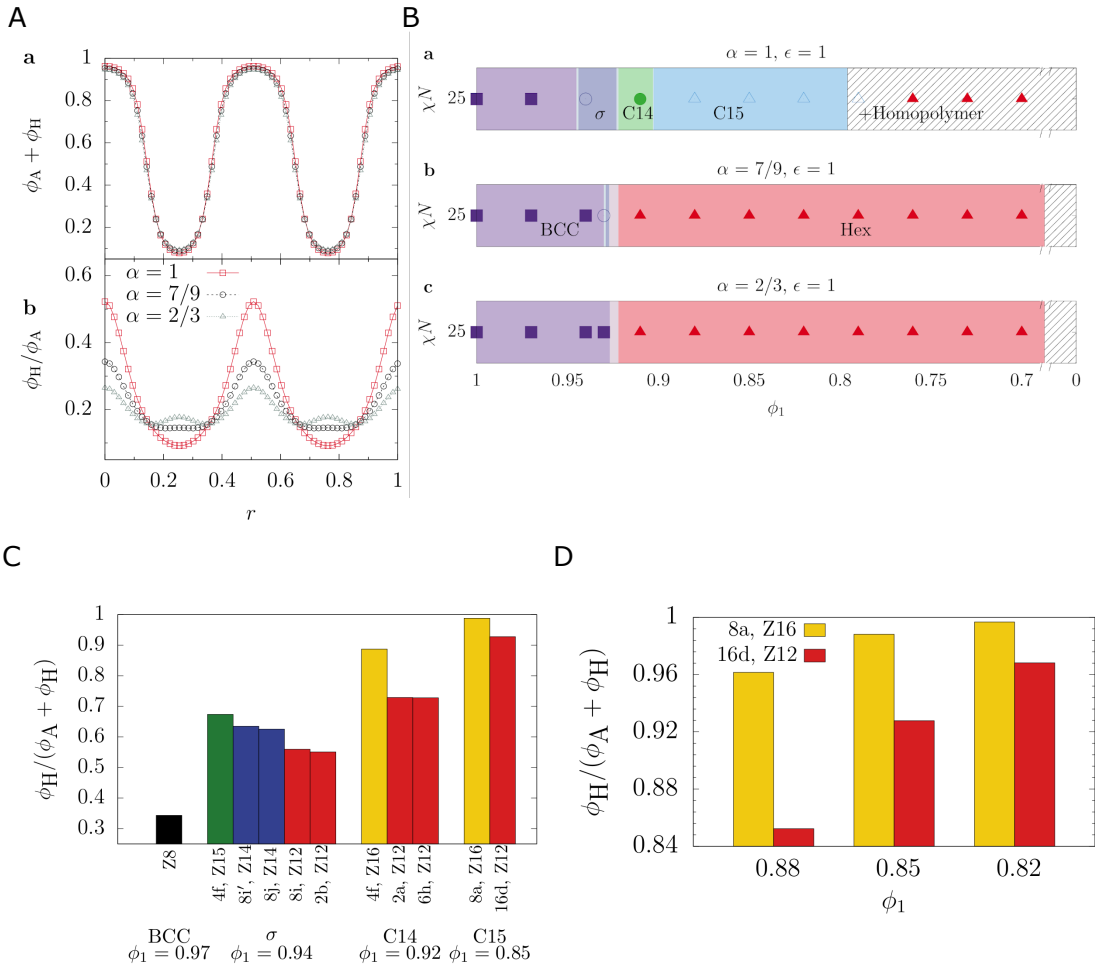
A
a
b
$\phi_A + \phi_H$
ϕ_H/ϕ_A
$\alpha = 1$
$\alpha = 7/9$
$\alpha = 2/3$
r
B
a
b
c
$\alpha = 1, \epsilon = 1$
$\alpha = 7/9, \epsilon = 1$
$\alpha = 2/3, \epsilon = 1$
χN
σ
C14
C15
+Homopolymer
BCC
Hex
ϕ_1
C
D
$\phi_H/(\phi_A + \phi_H)$
Z8
4f, Z15
8i', Z14
8j, Z14
8i, Z12
2b, Z12
4f, Z16
2a, Z12
6h, Z12
8a, Z16
16d, Z12
BCC
$\phi_1 = 0.97$
σ
$\phi_1 = 0.94$
C14
$\phi_1 = 0.92$
C15
$\phi_1 = 0.85$
8a, Z16
16d, Z12
ϕ_1

Figure A.3: Analysis for diblock copolymer-monomer blend at $\epsilon = 1$ and $\chi N = 25$ equivalent to those done in the main text for $\epsilon = 1.7$, $\chi N = 25$. (A) Illustration of the transition from dry brush to wet brush regimes as the homopolymer molecular weight decreases. (a) Volume fraction of the A monomers in the bcc phase at $\phi_1 = 0.97$ along the [111] direction for $\alpha = 1$ (red squares), $\alpha = 7/9$ (black circles), and $\alpha = 2/3$ (green triangles), where the position is made dimensionless with $\sqrt{3}a$ for the unit-cell parameter a. (b) Ratio of the A-homopolymer to A-block volume fractions for the conditions in (a). (B) Phase diagram of the diblock copolymer-monomer blend at $\epsilon = 1$ and $\chi N = 25$. The symbols indicate state points for SCFT calculations in the canonical ensemble. Phase boundaries between these state points were obtained by grand canonical ensemble calculations. Symbols correspond to bcc (■, dark purple), σ (○, light purple), C14 (●, green), C15 (△, blue), and hexagonally-packed (hex) cylinders (▲, red). Two-phase regions between ordered states are indicated by light shading. The hashed areas indicate two-phase regions that correspond to equilibrium between an ordered phase and a disordered phase. (C) Volume fraction of the homopolymer, ϕ_H, relative to the total volume fraction of A monomers at the center of a micellar particle, $\phi_A + \phi_H$, for the dry brush case $\alpha = 1$. The notation refers to the Wykoff positions of the particles and the number of faces in the polyhedra. The inset shows the planar graph forms of each of the polyhedra. (D) Volume fraction of the homopolymer, ϕ_H, relative to the total volume fraction of A monomers at the center of a micellar particle, $\phi_A + \phi_H$, for C15 at $\alpha = 1$. The color coding corresponds to panel (C).

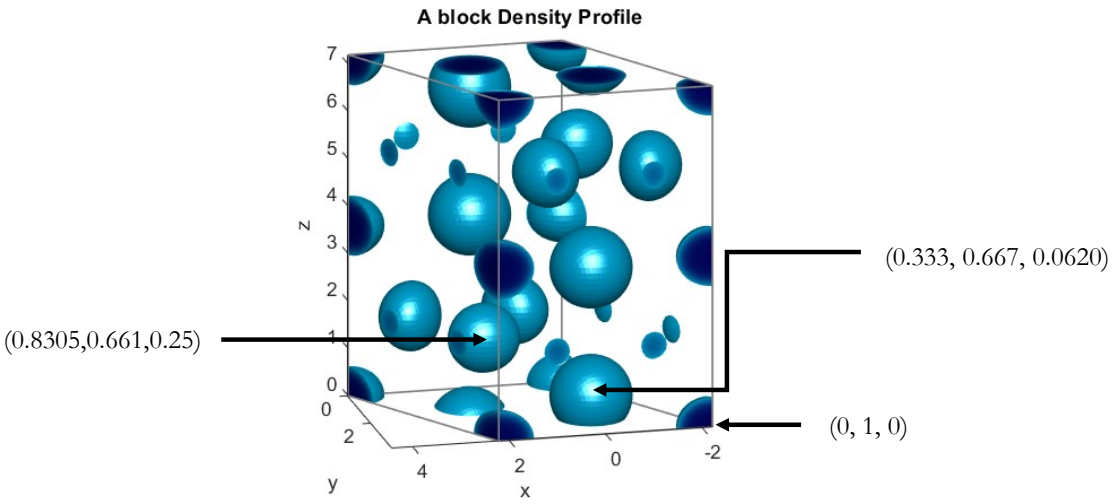

Figure A.4: Location of micelles are determined through our visualization software. Shown is the A-monomer isosurface ($\phi = 0.52$) for C14 phase with $\epsilon = 1.7$, $\alpha = 1$, $\chi N = 25$, and $\phi_1 = 0.92$ with distinct micelles labeled with their center's fractional coordinate in three dimensional space (x,y,z) based on the Wykoff positions for C14. The location of all other micelles can be determined from their space group symmetry.

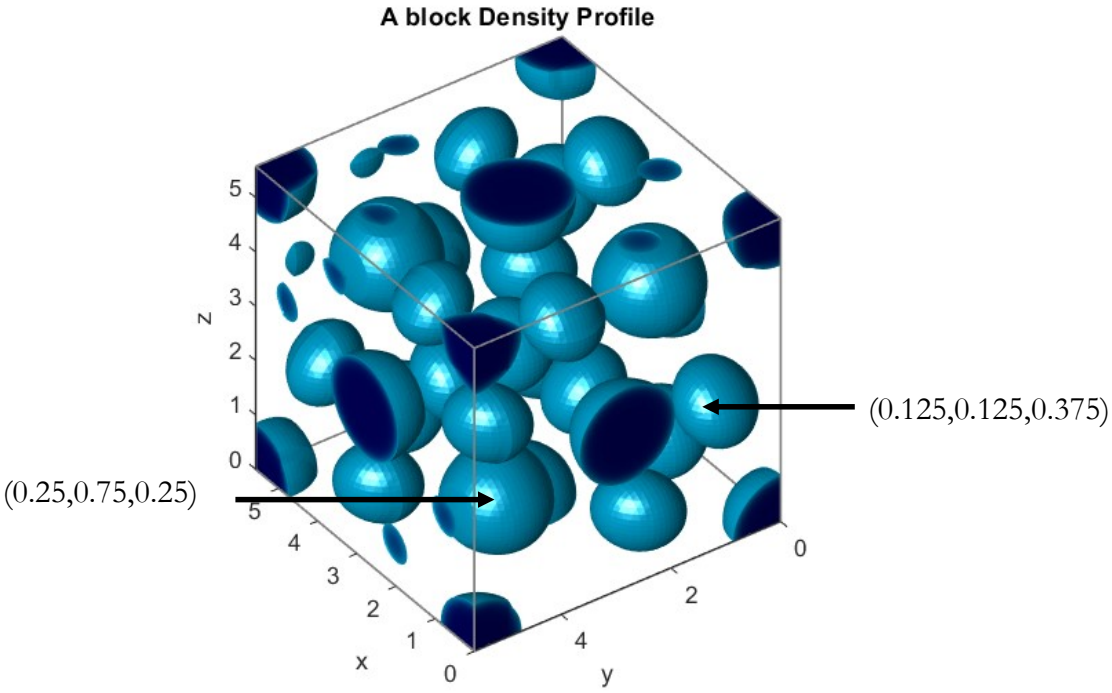

Figure A.5: Location of micelles are determined through our visualization software. Shown is the A-monomer isosurface ($\phi = 0.52$) for C15 with $\epsilon = 1.7$, $\alpha = 1$, $\chi N = 25$, and $\phi_1 = 0.85$ with distinct micelles labeled with their center's fractional coordinate in three dimensional space (x,y,z) based on the Wykoff positions for C15. The location of all other micelles can be determined from their space group symmetry.

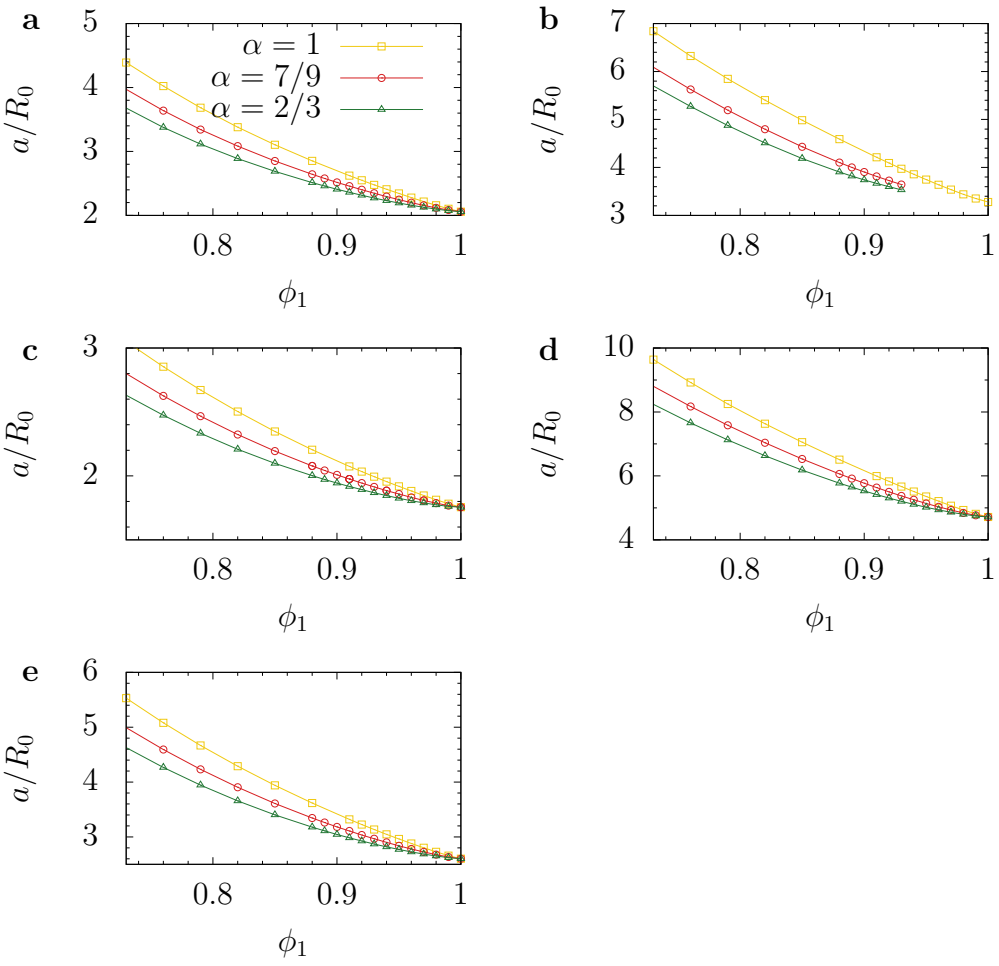

Figure A.6: Plot of unit cell dimensions normalized by the root-mean-square end-to-end length, a/R_0 versus the volume fraction of the diblock copolymer, ϕ_1 at different blending ratios, α for $\epsilon = 1.7$, $\chi N = 25$. Each panel represents the converged unit cell dimension in the canonical ensemble calculations of (a) BCC, (b) A15, (c) Hex, (d) C15, (e) FCC.

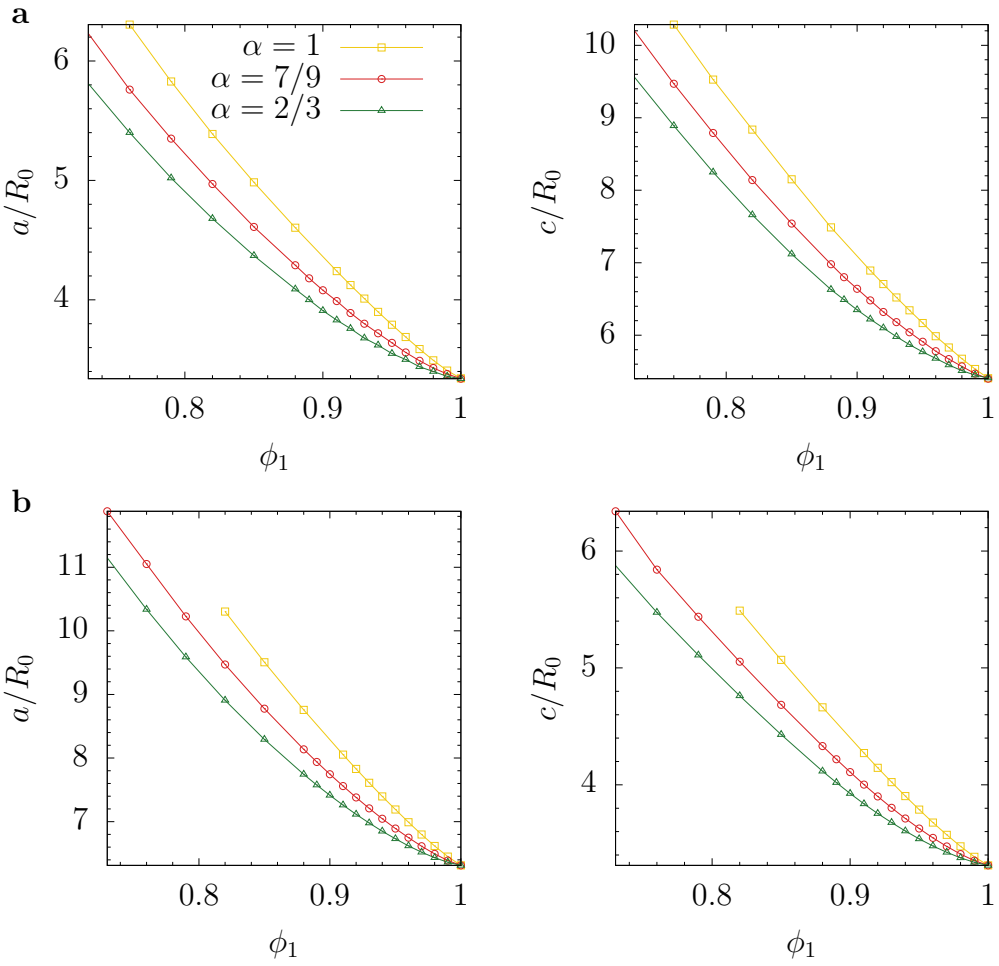

Figure A.7: Plot of non-cubic unit cell dimensions normalized by the root-mean-square end-to-end length, a/R_0 or c/R_0, versus the volume fraction of the diblock copolymer, ϕ_1 at different blending ratios, α for $\epsilon = 1.7$, $\chi N = 25$. Each panel represents the converged unit cell dimension in the canonical ensemble calculations of (a) C14, (b) σ.

Table A.1: Table of the relative free energy of each phase with respect to the BCC phase, $(F - F_{\mathrm{BCC}})/nk_{\mathrm{B}}T$, at different volume fraction of the diblock copolymer, ϕ_1 for $\epsilon = 1.7$, $\alpha = 1$, and $\chi N = 25$. Dashes denote states which do not converge to that particular phase.

	$(F - F_{\mathrm{BCC}})/nk_{\mathrm{B}}T$								
ϕ_1	A15	BCC	C14	C15	FCC	σ	Disordered	Hex	Stable Phase
1	0.000752	0.000000	0.001401	0.001548	-0.000063	0.000531	0.014083	0.030752	FCC
0.99	0.000952	0.000000	0.001620	0.001809	0.000019	0.000666	0.044428	0.030274	BCC
0.98	0.001014	0.000000	0.001590	0.001791	0.000074	0.000676	0.080040	0.027718	BCC
0.97	0.000955	0.000000	0.001371	0.001563	0.000127	0.000577	0.119760	0.024592	BCC
0.96	0.000788	0.000000	0.000996	0.001170	0.000163	0.000376	0.162818	0.021357	BCC
0.95	0.000507	0.000000	0.000485	0.000632	0.000188	0.000072	0.208632	0.018209	BCC
0.94	0.000113	0.000000	-0.000146	-0.000029	0.000198	-0.000336	0.256735	0.015242	σ
0.93	-0.000375	0.000000	-0.000863	-0.000778	0.000197	-0.000828	0.306758	0.012513	C14
0.92	-0.000948	0.000000	-0.001646	-0.001595	0.000188	-0.001398	0.358371	0.010036	C14
0.91	-0.001587	0.000000	-0.002471	-0.002446	0.000171	-0.002030	0.411291	0.007809	C14
0.88	-0.003716	0.000000	-0.005007	-0.005038	0.000043	-0.004116	0.575499	0.002488	C15
0.85	-0.005773	0.000000	-0.007279	-0.007345	-0.000121	-0.006137	0.743743	-0.001235	C15
0.82	-0.007348	0.000000	-0.008939	-0.009003	-0.000220	-0.007695	0.911811	-0.003829	C15
0.79	-0.008123	0.000000	-0.009772	-0.009796	-0.000064	-	1.076480	-0.005500	C15
0.76	-0.007903	0.000000	-0.009622	-0.009546	0.000493	-	1.235189	-0.006275	C14
0.73	-0.006780	0.000000	-0.008573	-0.008508	0.001349	-	1.385663	-0.006267	C14
0.7	-0.005164	0.000000	-0.007147	-0.006982	0.002165	-	1.525768	-0.005782	C14

Table A.2: Table of the relative free energy of each phase with respect to the BCC phase, $(F - F_{\mathrm{BCC}})/nk_{\mathrm{B}}T$, at different volume fraction of the diblock copolymer, ϕ_1 for $\epsilon = 1.7$, $\alpha = 0.78$, and $\chi N = 25$. Dashes denote states which do not converge to that particular phase.

	$(F - F_{\mathrm{BCC}})/nk_{\mathrm{B}}T$								
ϕ_1	A15	BCC	C14	C15	FCC	σ	Disordered	Hex	Stable Phase
1	-	0.000000	0.001403	0.001550	-0.000061	0.000534	0.014086	0.030755	FCC
0.99	-	0.000000	0.001630	0.001814	0.000019	0.000664	0.035262	0.029913	BCC
0.98	-	0.000000	0.001713	0.001917	0.000093	0.000720	0.059734	0.027376	BCC
0.97	-	0.000000	0.001669	0.001879	0.000160	0.000699	0.087031	0.024171	BCC
0.96	-	0.000000	0.001527	0.001732	0.000224	0.000618	0.116822	0.020698	BCC
0.95	-	0.000000	0.001278	0.001468	0.000280	0.000458	0.148806	0.017147	BCC
0.94	-	0.000000	0.000929	0.001097	0.000336	0.000217	0.182742	0.013644	BCC
0.93	0.018209	0.000000	0.000497	0.000637	0.000386	-0.000095	0.218425	0.010279	σ
0.92	0.017281	0.000000	-0.000024	0.000084	0.000426	-0.000492	0.255648	0.007089	σ
0.91	0.016481	0.000000	-0.000623	-0.000549	0.000457	-0.000970	0.294235	0.004109	σ
0.9	0.015755	0.000000	-0.001285	-0.001244	0.000483	-0.001514	0.334028	0.001365	σ
0.89	0.015057	0.000000	-0.002001	-0.001990	0.000504	-0.002119	0.374869	-0.001140	σ
0.88	0.014353	0.000000	-0.002756	-0.002772	0.000513	-0.002773	0.416612	-0.003406	Hex
0.85	0.012009	0.000000	-0.005093	-0.005172	0.000519	-0.004867	0.545919	-0.008835	Hex
0.82	0.009263	0.000000	-0.007232	-0.007336	0.000509	-0.006840	0.678773	-0.012489	Hex
0.79	0.006525	0.000000	-0.008823	-0.008907	0.000590	-0.008308	0.812262	-0.014735	Hex
0.76	0.004492	0.000000	-0.009517	-0.009574	0.000946	-0.008893	0.943960	-0.015759	Hex
0.73	0.003683	0.000000	-0.009053	-0.009068	0.001705	-0.008379	1.071733	-0.015648	Hex
0.7	0.004073	0.000000	-0.007627	-0.007671	0.002709	-0.006970	1.193451	-0.014660	Hex

Table A.3: Table of the relative free energy of each phase with respect to the BCC phase, $(F - F_{\mathrm{BCC}})/nk_{\mathrm{B}}T$, at different volume fraction of the diblock copolymer, ϕ_1 for $\epsilon = 1.7$, $\alpha = 0.67$, and $\chi N = 25$. Dashes denote states which do not converge to that particular phase.

	$(F - F_{\mathrm{BCC}})/nk_{\mathrm{B}}T$								
ϕ_1	A15	BCC	C14	C15	FCC	σ	Disordered	Hex	Stable Phase
1	-	0.000000	0.001403	0.001551	-0.000062	0.000535	0.014087	0.030755	FCC
0.99	-	0.000000	0.001605	0.001785	0.000009	0.000647	0.030605	0.029826	BCC
0.98	-	0.000000	0.001712	0.001913	0.000079	0.000712	0.049376	0.027517	BCC
0.97	-	0.000000	0.001737	0.001949	0.000157	0.000730	0.070173	0.024566	BCC
0.96	-	0.000000	0.001685	0.001898	0.000214	0.000697	0.092818	0.021276	BCC
0.95	-	0.000000	0.001559	0.001766	0.000282	0.000612	0.117164	0.017821	BCC
0.94	-	0.000000	0.001359	0.001553	0.000353	0.000469	0.143075	0.014315	BCC
0.93	0.017600	0.000000	0.001087	0.001260	0.000405	0.000264	0.170428	0.010838	BCC
0.92	0.016462	0.000000	0.000741	0.000889	0.000463	-0.000007	0.199109	0.007451	σ
0.91	0.015516	0.000000	0.000326	0.000445	0.000520	-0.000346	0.229010	0.004198	σ
0.9	0.014692	0.000000	-0.000155	-0.000068	0.000569	-0.000753	0.260026	0.001110	σ
0.89	0.013945	0.000000	-0.000702	-0.000648	0.000613	-0.001229	0.292054	-0.001791	Hex
0.88	0.013241	0.000000	-0.001303	-0.001283	0.000652	-0.001765	0.325000	-0.004487	Hex
0.85	0.011109	0.000000	-0.003357	-0.003423	0.000740	-0.003651	0.428400	-0.011270	Hex
0.82	0.008620	0.000000	-0.005537	-0.005655	0.000788	-0.005688	0.536743	-0.016138	Hex
0.79	0.005842	0.000000	-0.007486	-0.007607	0.000847	-0.007500	0.647714	-0.019300	Hex
0.76	0.003345	0.000000	-0.008810	-0.008913	0.001032	-0.008700	0.759199	-0.020991	Hex
0.73	0.001848	0.000000	-0.009104	-0.009171	0.001550	-0.008897	0.869323	-0.021313	Hex
0.7	0.001744	0.000000	-0.008160	-0.008204	0.002467	-0.007925	0.976262	-0.020392	Hex

Table A.4: Table of the relative free energy of each phase with respect to the BCC phase, $(F - F_{\mathrm{BCC}})/nk_{\mathrm{B}}T$, at different volume fraction of the diblock copolymer, ϕ_1 for $\epsilon = 1.7$, $\alpha = 1$ and $\chi N = 20$. Note that SCFT calculations are resolved to a higher accuracy for certain cases such as $\phi_1 = 0.88$ due to the similar free energies between different phases. Dashes denote states which do not converge to that particular phase.

	$(F - F_{\mathrm{BCC}})/nk_{\mathrm{B}}T$								
ϕ_1	A15	BCC	C14	C15	FCC	σ	Disordered	Hex	Stable Phase
0.94	0.000125	0.000000	0.000321	0.000331	-0.000346	0.000005	0.006954	-	FCC
0.93	0.000178	0.000000	0.000319	0.000346	-0.000403	0.000015	0.024251	0.020368	FCC
0.92	0.000149	0.000000	0.000161	0.000193	-0.000462	-0.000052	0.044917	0.019502	FCC
0.91	0.000044	0.000000	-0.000102	-0.000070	-0.000521	-0.000184	0.068274	0.018105	FCC
0.9	-0.000131	0.000000	-0.000451	-0.000430	-0.000596	-0.000384	0.093858	0.016519	FCC
0.89	-0.000366	0.000000	-0.000855	-0.000841	-0.000676	-0.000634	0.121329	0.014910	C14
0.88	-0.000652	0.000000	-0.001294	-0.001290	-0.000759	-0.000929	0.150398	0.013353	C14
0.85	-0.001686	0.000000	-0.002685	-0.002700	-0.001083	-0.001976	0.244890	0.009285	C15
0.82	-0.002720	0.000000	-0.003896	-0.003919	-0.001421	-0.003003	0.346520	0.006237	C15
0.79	-0.003461	0.000000	-0.004694	-0.004713	-0.001650	-0.003733	0.451482	0.004087	C15
0.76	-0.003730	0.000000	-0.004958	-0.004970	-0.001671	-0.003992	0.556836	0.002692	C15
0.73	-0.003515	0.000000	-0.004697	-0.004682	-0.001436	-0.003760	0.660171	0.001913	C14
0.7	-0.002940	0.000000	-0.004080	-0.004058	-0.001027	-0.003190	0.759438	0.001597	C14

Table A.5: Table of the relative free energy of each phase with respect to the BCC phase, $(F - F_{\mathrm{BCC}})/nk_{\mathrm{B}}T$, at different volume fraction of the diblock copolymer, ϕ_1 for $\epsilon = 1.7$, $\alpha = 0.78$ and $\chi N = 20$. Dashes denote states which do not converge to that particular phase.

	$(F - F_{\mathrm{BCC}})/nk_{\mathrm{B}}T$								
ϕ_1	A15	BCC	C14	C15	FCC	σ	Disordered	Hex	Stable Phase
0.92	-	0.000000	-	-	-0.000253	0.000037	0.000941	-	FCC
0.91	-	0.000000	-	0.000479	-0.000260	0.000066	0.011774	0.016474	FCC
0.88	-	0.000000	-	0.000112	-0.000285	-0.000185	0.056356	0.012080	FCC
0.85	0.010037	0.000000	-	-0.000902	-0.000365	-0.000941	0.113946	0.006353	σ
0.82	0.008415	0.000000	0.004048	-0.002251	-0.000500	-0.002070	0.180606	0.001401	C15
0.79	0.006859	0.000000	0.001597	-0.003623	-0.000682	-0.003298	0.253424	-0.002364	C15
0.76	0.005302	0.000000	-0.000665	-0.004682	-0.000793	-0.004284	0.330000	-0.004930	Hex
0.73	0.004069	0.000000	-0.002212	-0.005175	-0.000680	-0.004747	0.408267	-0.006400	Hex
0.7	0.003522	0.000000	-0.002951	-0.004933	-0.000233	-0.004511	0.486402	-0.006880	Hex

Table A.6: Table of the relative free energy of each phase with respect to the BCC phase, $(F - F_{\mathrm{BCC}})/nk_{\mathrm{B}}T$, at different volume fraction of the diblock copolymer, ϕ_1 for $\epsilon = 1.7$, $\alpha = 0.67$ and $\chi N = 20$. Dashes denote states which do not converge to that particular phase.

	$(F - F_{\mathrm{BCC}})/nk_{\mathrm{B}}T$								
ϕ_1	A15	BCC	C14	C15	FCC	σ	Disordered	Hex	Stable Phase
0.9	-	0.000000	-	-	-0.000205	-	0.000108	-	FCC
0.89	-	0.000000	-	-	-0.000192	-	0.008229	0.013978	FCC
0.88	-	0.000000	-	0.000504	-0.000176	-	0.017911	0.013040	FCC
0.85	-	0.000000	0.008302	0.000094	-0.000153	-	0.054323	0.007796	FCC
0.82	0.007645	0.000000	0.005204	-0.000814	-0.000163	-	0.099457	0.002081	C15
0.79	0.006123	0.000000	0.002309	-0.002047	-0.000236	-	0.151146	-0.002901	Hex
0.76	0.004587	0.000000	-0.000112	-0.003360	-0.000342	-	0.207625	-0.006767	Hex
0.73	0.003030	0.000000	-0.002058	-0.004445	-0.000403	-	0.267316	-0.009429	Hex
0.7	0.001875	0.000000	-0.003312	-0.004950	-0.000236	-	0.328824	-0.010855	Hex

Table A.7: Table of the relative free energy of each phase with respect to the BCC phase, $(F - F_{\mathrm{BCC}})/nk_{\mathrm{B}}T$, at different volume fraction of the diblock copolymer, ϕ_1, for $\epsilon = 1$, $\alpha = 1$, and $\chi N = 25$. Dashes denote states which do not converge to that particular phase.

	$(F - F_{\mathrm{BCC}})/nk_{\mathrm{B}}T$								
ϕ_1	A15	BCC	C14	C15	FCC	σ	Disordered	Hex	Stable Phase
1	-	0.000000	0.001458	0.001626	0.000055	0.000607	0.027954	0.021470	BCC
0.97	0.000952	0.000000	0.001450	0.001643	0.000231	0.000638	0.135506	0.013890	BCC
0.94	0.000168	0.000000	0.000128	0.000241	0.000322	-0.000190	0.273641	0.005955	σ
0.93	-0.000285	0.000000	-0.000511	-0.000435	0.000338	-0.000642	0.324085	0.003799	σ
0.92	-0.000816	0.000000	-0.001216	-0.001170	0.000345	-0.001167	0.376140	0.001902	C14
0.91	-0.001413	0.000000	-0.001967	-0.001947	0.000338	-0.001752	0.429518	0.000249	C14
0.9	-0.002052	0.000000	-0.002741	-0.002747	0.000316	-0.002380	0.483961	-0.001183	C15
0.89	-0.002721	0.000000	-0.003520	-0.003549	0.000291	-0.003033	0.539238	-0.002420	C15
0.88	-0.003391	0.000000	-0.004285	-0.004330	0.000260	-0.003691	0.595141	-0.003486	C15
0.85	-0.005329	0.000000	-0.006418	-0.006489	0.000145	-0.005597	0.764725	-0.005954	C15
0.82	-0.006878	0.000000	-0.008081	-0.008142	0.000074	-0.007125	0.933917	-0.007664	C15
0.79	-0.007728	0.000000	-0.009030	-0.009058	0.000203	-0.007963	1.099438	-0.008767	C15
0.76	-0.007623	0.000000	-0.008986	-0.008975	0.000698	-0.007883	1.258749	-0.009169	Hex
0.73	-0.006596	0.000000	-0.007993	-0.008048	0.001516	-0.006938	1.409618	-0.008882	Hex
0.7	-0.005091	0.000000	-0.006645	-0.006501	0.002302	-	1.549902	-0.008197	Hex

Table A.8: Table of the relative free energy of each phase with respect to the BCC phase, $(F - F_{\mathrm{BCC}})/nk_{\mathrm{B}}T$, at different volume fraction of the diblock copolymer, ϕ_1, for $\epsilon = 1$, $\alpha = 0.78$, and $\chi N = 25$. Dashes denote states which do not converge to that particular phase.

	$(F - F_{\mathrm{BCC}})/nk_{\mathrm{B}}T$								
ϕ_1	A15	BCC	C14	C15	FCC	σ	Disordered	Hex	Stable Phase
1	-	0.000000	0.001455	0.001622	0.000055	0.000605	0.027952	0.021468	BCC
0.99	-	0.000000	0.001639	0.001834	0.000123	0.000706	0.049485	0.019380	BCC
0.98	-	0.000000	0.001718	0.001928	0.000189	0.000751	0.074046	0.016593	BCC
0.97	-	0.000000	0.001697	0.001908	0.000247	0.000734	0.101295	0.013490	BCC
0.96	0.014800	0.000000	0.001589	0.001792	0.000305	0.000662	0.130966	0.010293	BCC
0.95	0.013923	0.000000	0.001384	0.001571	0.000360	0.000517	0.162808	0.007123	BCC
0.94	0.013276	0.000000	0.001083	0.001246	0.000407	0.000293	0.196603	0.004064	BCC
0.93	0.012782	0.000000	0.000704	0.000836	0.000452	0.000000	0.232168	0.001186	σ
0.92	0.012374	0.000000	0.000237	0.000336	0.000495	-0.000376	0.269309	-0.001484	Hex
0.91	0.012009	0.000000	-0.000302	-0.000241	0.000530	-0.000827	0.307857	-0.003924	Hex
0.9	0.011656	0.000000	-0.000908	-0.000878	0.000559	-0.001343	0.347655	-0.006118	Hex
0.89	0.011278	0.000000	-0.001564	-0.001566	0.000580	-0.001916	0.388543	-0.008072	Hex
0.88	0.010852	0.000000	-0.002254	-0.002288	0.000593	-0.002530	0.430376	-0.009790	Hex
0.85	0.009140	0.000000	-0.004428	-0.004521	0.000616	-0.004486	0.560134	-0.013689	Hex
0.82	0.006828	0.000000	-0.006457	-0.006565	0.000620	-0.006331	0.693592	-0.016089	Hex
0.79	0.004404	0.000000	-0.008027	-0.008125	0.000689	-0.007746	0.827686	-0.017427	Hex
0.76	0.002604	0.000000	-0.008755	-0.008819	0.004780	-0.008365	0.959905	-0.017848	Hex
0.73	0.001979	0.000000	-0.008370	-0.008398	0.003958	-0.007932	1.088092	-0.017342	Hex
0.7	0.002515	0.000000	-0.007093	-0.007031	0.004144	-0.006601	1.210101	-0.016095	Hex

Table A.9: Table of the relative free energy of each phase with respect to the BCC phase, $(F - F_{\mathrm{BCC}})/nk_{\mathrm{B}}T$, at different volume fraction of the diblock copolymer, ϕ_1, for $\epsilon = 1$, $\alpha = 0.67$, and $\chi N = 25$. Dashes denote states which do not converge to that particular phase.

	$(F - F_{\mathrm{BCC}})/nk_{\mathrm{B}}T$								
ϕ_1	A15	BCC	C14	C15	FCC	σ	Disordered	Hex	Stable Phase
1	-	0.000000	0.001457	0.001624	0.000057	0.000606	0.027954	0.021469	BCC
0.99	-	0.000000	0.001618	0.001809	0.000118	0.000693	0.044603	0.019468	BCC
0.98	-	0.000000	0.001714	0.001920	0.000178	0.000745	0.063288	0.016892	BCC
0.97	-	0.000000	0.001747	0.001960	0.000237	0.000758	0.083864	0.013992	BCC
0.96	-	0.000000	0.001715	0.001928	0.000296	0.000729	0.106210	0.010920	BCC
0.95	0.013457	0.000000	0.001618	0.001822	0.000353	0.000650	0.130210	0.007783	BCC
0.94	0.012609	0.000000	0.001454	0.001642	0.000408	0.000518	0.155757	0.004660	BCC
0.93	0.011938	0.000000	0.001221	0.001388	0.000462	0.000324	0.182750	0.001611	BCC
0.92	0.011389	0.000000	0.000920	0.001059	0.000513	0.000066	0.211089	-0.001317	Hex
0.91	0.010925	0.000000	0.000547	0.000656	0.000561	-0.000261	0.240675	-0.004090	Hex
0.9	0.010513	0.000000	0.000113	0.000185	0.000607	-0.000655	0.271415	-0.006680	Hex
0.89	0.010123	0.000000	-0.000387	-0.000350	0.000649	-0.001117	0.303211	-0.009072	Hex
0.88	0.009726	0.000000	-0.000943	-0.000941	0.000685	-0.001636	0.335970	-0.011252	Hex
0.85	0.008300	0.000000	-0.002852	-0.002941	0.000770	-0.003432	0.439083	-0.016508	Hex
0.82	0.006279	0.000000	-0.004907	-0.005038	0.000817	-0.005330	0.547481	-0.019981	Hex
0.79	0.003840	0.000000	-0.006767	-0.006898	0.000868	-0.007019	0.658713	-0.022009	Hex
0.76	0.001618	0.000000	-0.008059	-0.008167	0.001030	-0.008160	0.770538	-0.022870	Hex
0.73	0.000358	0.000000	-0.008357	-0.008416	0.001491	-0.008356	0.881008	-0.022628	Hex
0.7	0.000455	0.000000	-0.007494	-0.007505	0.002347	-0.007408	0.988259	-0.021329	Hex

Table A.10: Table of the relative free energy of each phase with respect to the BCC phase, $(F - F_{\mathrm{BCC}})/nk_{\mathrm{B}}T$, at different volume fraction of the diblock copolymer, ϕ_1 for $\epsilon = 1.7$, $\alpha = 1$ and $\chi N = 30$.

	$(F - F_{\mathrm{BCC}})/nk_{\mathrm{B}}T$								
ϕ_1	A15	BCC	C14	C15	FCC	σ	Disordered	Hex	Stable Phase
1	0.002025	0.000000	0.003216	0.003660	0.000773	0.001512	0.242428	0.027209	BCC
0.99	0.001829	0.000000	0.002755	0.003156	0.000868	0.001278	0.309213	0.022570	BCC
0.98	0.001506	0.000000	0.002123	0.002474	0.000961	0.000926	0.378899	0.018244	BCC
0.97	0.001046	0.000000	0.001334	0.001625	0.001047	0.000447	0.450964	0.014285	BCC
0.96	0.000462	0.000000	0.000417	0.000650	0.001129	-0.000146	0.524986	0.010727	σ
0.95	-0.000244	0.000000	-0.000607	-0.000437	0.001205	-0.000851	0.600592	0.007565	σ
0.94	-0.001052	0.000000	-0.001710	-0.001591	0.001274	-0.001648	0.677457	0.004785	C14
0.93	-0.001942	0.000000	-0.002868	-0.002793	0.001340	-0.002523	0.755289	0.002356	C14
0.92	-0.002898	0.000000	-0.004052	-0.004018	0.001395	-0.003456	0.833819	0.000241	C14
0.91	-0.003889	0.000000	-0.005237	-0.005232	0.001445	-0.004424	0.912807	-0.001597	C14
0.88	-0.006840	0.000000	-0.008564	-0.008656	0.001579	-0.007308	1.150421	-0.005805	C15
0.85	-0.009384	0.000000	-0.011289	-0.011379	0.001714	-0.009833	1.385217	-0.008719	C15
0.82	-0.011111	0.000000	-0.013172	-0.013193	0.001957	-0.011548	1.613333	-0.010773	C15
0.79	-0.011665	0.000000	-0.014011	-0.013900	0.002481	-0.012118	1.831824	-0.011974	C14
0.76	-0.010857	0.000000	-0.013513	-0.013110	0.003393	-0.011311	2.038295	-0.012186	C14

Appendix B

Supplementary Information to Chapter 4

	$\epsilon = 1$			$\epsilon = 3$		
χN	a	b	c	a	b	c
10	0.71065	-0.14639	0.00692	-0.23557	0.304603	-0.01727
20	-2.84761	0.27661	-0.00958	-7.20269	0.957654	-0.03908
23	-3.74362	0.43130	-0.01358	-7.38918	0.984815	-0.05325

Table B.1: Fitting parameters for Eq. 4.2 for data for $\chi N = 10, 20, 23$ and $\epsilon = 1, 3$ that minimizes the mean square error.

χN	$\epsilon = 1$	$\epsilon = 3$
10	[0.9069 - 5.9469]	[1.4623 - 5.3729]
20	[0.9069 - 5.0085]	[1.4623 - 5.6636]
23	[0.9069 - 3.4534]	[1.0340 - 4.8500]

Table B.2: Range for qR_g used in fitting Eq. 8 of the main text which best fits the peak.

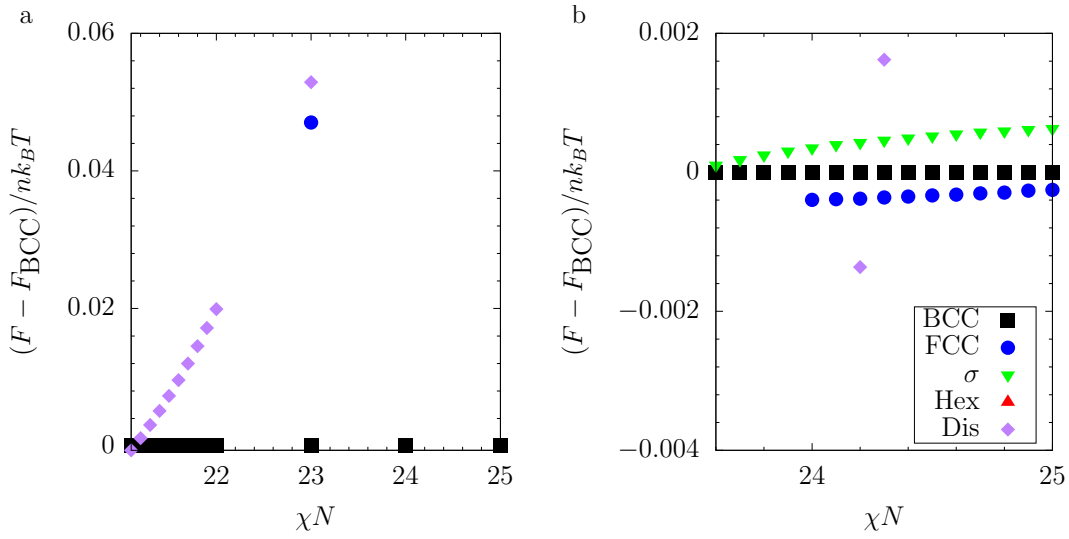

Figure B.1: Plot of $(F - F_{BCC})/nk_BT$ versus χN for (a) $\epsilon = 1$, (b)$\epsilon = 3$ where the phases are BCC (black ■), FCC (blue ●), σ (green ▼), Hex (red ▲), Dis (yellow ♦). In most cases, Hex phase exceeds the scale of the plot for most of the range of χN. The stability of σ phase was only tested for the case of $\epsilon = 3.0$. The full phase diagram for other values of ϵ that includes σ phases can be found elsewhere [31].

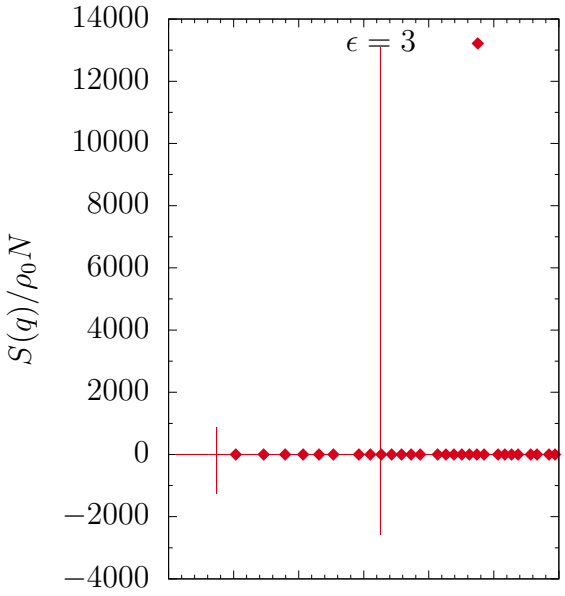

Figure B.2: Example of fitting to Eq. 4.2 of the main text for the full dataset for $\epsilon = 3$ and $\chi N = 20$.

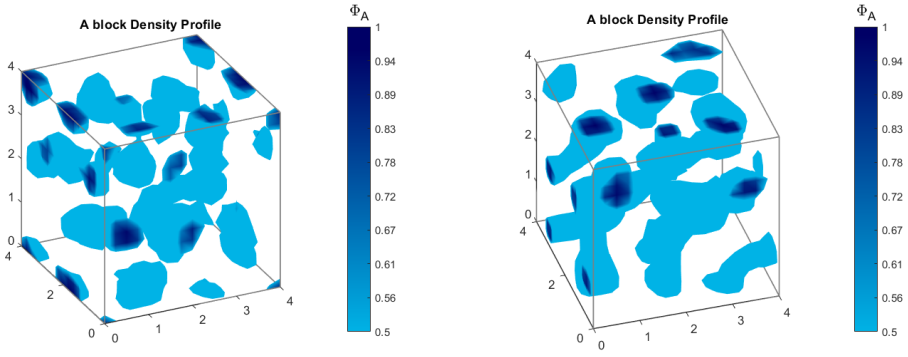

Figure B.3: Snapshot of density field for $\epsilon = 1$ at $\chi N = 26$(left) and $\chi N = 30$ (right) started from the homogeneous initial condition.

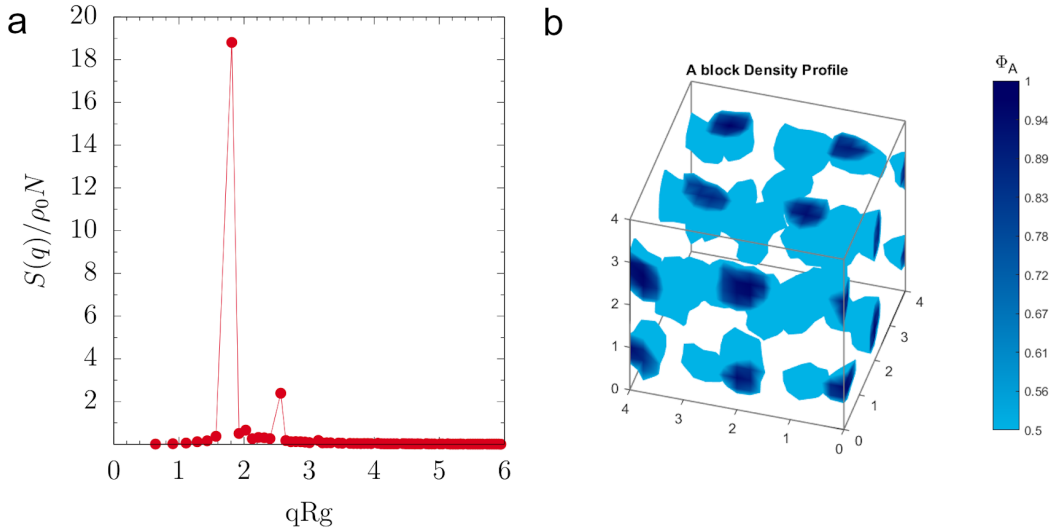

Figure B.4: a) Structure factor and b) Density field for the simulation started from the ordered initial condition at $\chi N = 26$ and $\epsilon = 1$.

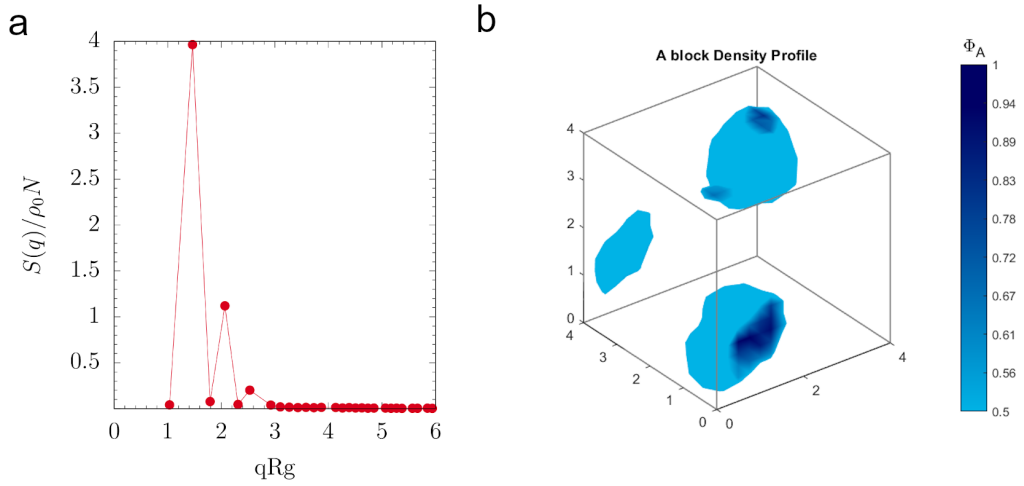

Figure B.5: a) Structure factor and b) Density field for the simulation started from the ordered initial condition at $\chi N = 26$ and $\epsilon = 3$.

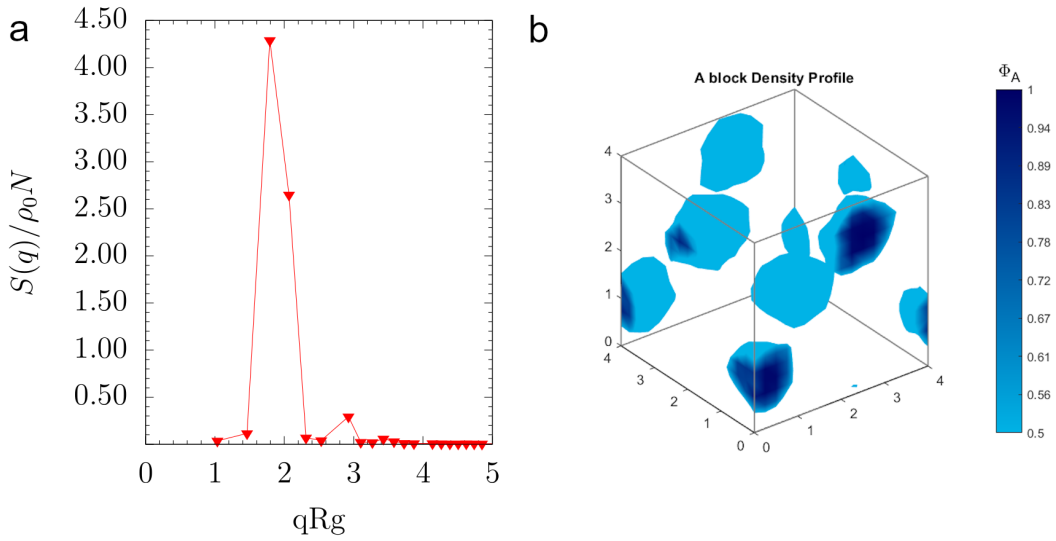

Figure B.6: a) Structure factor and b) Density field for the simulation started from the homogeneous initial condition at $\chi N = 26$ and $\epsilon = 3$.

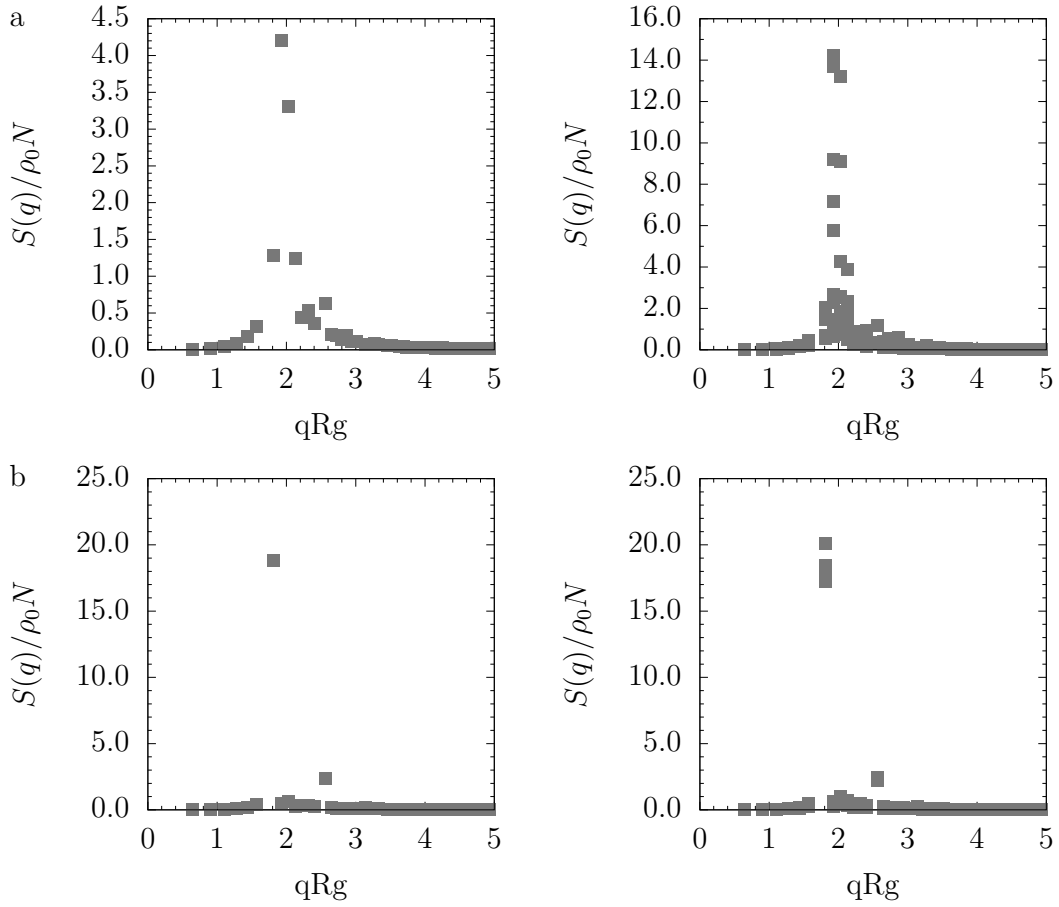

Figure B.7: Structure factor for a) $\epsilon = 1$, $\chi N = 26$, started with a homogeneous initial condition and b) $\epsilon = 1$, $\chi N = 26$, started with an ordered initial condition. The left column shows the structure factor from averaging the wavevectors corresponding to the same wavenumber. The right column shows the structure factor without averaging the wavevectors.